UNIVERSITÀ DEGLI STUDI DI TORINO

SCUOLA DI SCIENZE DELLA NATURA

Corso di Laurea Magistrale in Fisica

Tesi di Laurea Magistrale

OPTICAL LATTICE CLOCK WITH AN AMPLIFIED LASER DIODE

Relatore:
Prof.ssa Elena Botta UNITO

Correlatore:
Dr.Marco Pizzocaro INRiM

Candidato:
Stefano Condio

Controrelatore:
Prof. Paolo Olivero

Anno Accademico 2020/2021

Abstract

Optical lattice clocks occupy a very important position in metrological research. Diffused worldwide, they are a strong candidate for a future redefinition of the second of the International System of Units (SI) and thanks to their extremely small fractional uncertainty about 10^{-18} they are involved in fundamental physics experiments, for example in the field of general relativity. In a optical clock, the lattice is used to trap ultracold atoms and it is realized with a retro-reflected laser tuned on magic wavelength to reduce perturbations on the clock transition. An optical lattice is generated usually starting by a titanium:sapphire laser: its main qualities are high output power and narrow linewidth, but it is delicate and difficult to use so its application in new kinds of atomic clocks, such as transportable or spacial, is not strongly recommended. Replacing it with an amplified laser diode would be preferable because these instruments are better for cost, reliability, size and weight, so suitable for applications out of laboratory, but at the same time present the problem of spectral purity as they have a not negligible amplified spontaneous emission (ASE): this phenomenon produces a broad spectrum detuned from magic wavelength inducing a perturbation on the clock transition. In my thesis I investigated experimentally the possibility to generate an optical lattice starting from an amplified laser diode emitting at $759.35\,\text{nm}$, ytterbium magic wavelength, and I applied the laser system that I developed on the atomic clock IT-Yb1 at Istituto Nazionale di Ricerca Metrologica (INRiM) located in Torino. The target of this work is to achieve fractional uncertainty due to ASE below 10^{-18}, making the performances of the two different lasers sources equivalent. First, I calculated the theoretical model of the light shift induced by the lattice on the clock transition between ytterbium atomic states $^1S_0 \rightarrow\,^3 P_0$, comparing it with experimental results and I applied it to estimate ASE contribution to lattice shift. In the experimental part of this work I realized an optical system to study amplified laser diode emission and manipulate laser beam to obtain a good lattice from this laser source, filtering ASE with a volume Bragg grating and controlling power with an acousto optic modulator. Moreover I studied ASE spectral distribution in different conditions and its interaction with optical elements. Next studies foresee to measure experimentally with IT-Yb1 the shift induced by the laser system that I realized to calculate its uncertainty contribution and compare this result with the one obtained with a titanium:sapphire laser. This work will be useful to the development of compact or transportable atomic clocks based exclusively on semiconductor lasers with applications in the generation of optical timescales, travelling optical standards and the measurements of Earth gravitational redshift.

Aknowledges

Vorrei ringraziare in primo luogo la mia famiglia che mi ha sempre supportato durante questi ani di università. Per la riuscita di questa tesi vorrei esprimere la mia riconoscenza verso la professoressa Elena Botta, che mi ha seguito in qualità di relatrice e le cui correzioni, non solo di carattere scientifico ma anche linguistiche, si sono rivelate estremamente utili. La mia più grande riconoscenza va al dottor Marco Pizzocaro, che mi ha affiancato durante questo periodo passato all'INRiM sempre pronto ad aiutarmi e a consigliarmi oltre che a fornire il suo prezioso supporto nel lavoro sperimentale. Ringrazio Irene Goti per l'aiuto fornito in laboratorio. Vorrei ringraziare l'Istituto Nazionale di Ricerca Metrologica e in particolare Davide Calonico, a capo della divisione "Quantum Metrology and Nanotech", per avermi accolto presso questo centro di ricerca e per avermi dato la possibilità di svolgere l'attività sperimentale in presenza nonostante il perdurare della situazione pandemica. Vorrei ringraziare tutti gli altri componenti della divisione "Tempo e Frequenza" dell'INRiM che ho avuto modo di conoscere durante il periodo passato in istituto, per la loro collaborazione e la loro simpatia.

Infine un pensiero speciale va a Giada.

Funding

The EMPIR initiative is co-funded by the European Union's Horizon 2020 research and innovation programme and the EMPIR Participating States

Contents

Chapter 1

Introduction

1.1 International System of Units

Figure 1.1: SI fundamental units and physical constants

The International System of Units (SI) [1] is the most worldwide used system of unity measure and it finds application in different fields that spans from everyday to economy, industrial and scientific research. It was formally defined in 1960 during the 11th CGPM (General Conference on Weights and Measures). As shown in fig.(1.1) it is composed by a set of seven base units (second, meter, kilogram, ampere, kelvin, mole and candela) to measure seven quantities (respectively time, length, mass, electric current, thermodynamic temperature, amount of substance, luminous intensity) from which building all other derived units is possible. From 2019 these units are defined starting from seven physical constants whose numerical value is set as fixed and exact (without uncertainty). National metrological Institutes have the task of preserving and disseminating these SI units in their respective countries. In particular I will

focus on the second(s), the unity of the time, that is currently defined as follows: *"by taking the fixed numerical value of the caesium frequency $\Delta\nu_{Cs}$, the unperturbed ground-state hyperfine transition frequency of the caesium 133 atom, to be 9192631770 when expressed in the unit Hz, which is equal to s^{-1}"*.

So this definition fixes the numerical value of the absolute frequency of the microwave transition between the two hyperfine ground states of ^{133}Cs atom and inverting this relation:

$$1\,\mathrm{s} = \frac{9192631770}{\Delta\nu_{Cs}} \tag{1.1}$$

The second is so defined starting by the duration of a certain number of periods of this microwave transition of caesium. Important issue is the term "unperturbed" atom, that underlines that an atom not influenced by any external field must be considered, taking in account eventual corrections such as for electric or magnetic fields.

1.2 Atomic Clock

The instruments used to obtain a standard of the second referred directly to SI definition are atomic clocks. In particular the caesium fountain, like the one reported in fig.(1.2), constitutes the primary realization of the SI second.

Figure 1.2: IT-CsF2 [2], caesium fountain that constitutes the primary frequency standard for Italy. It is conserved at INRiM in Torino

The hyperfine transition that constitutes the frequency standard is probed with a low noise microwave that represents the local oscillator, comparing its known frequency with the reference to determine its value. If the probe radiation frequency is very close to the atomic resonance of the sample there is an excitation of the clock transition. Then the detection phase is able to measure how many atoms interacted, estimating how much the oscillator frequency is close to the reference. After that, a small correction is applied on the local oscillator to repeat the measure and to determine the exact frequency of resonance and locking the frequency on the atomic resonance.

In the hypothesis that atoms are ever equal in every point of universe and in every time, can be considered as an eternal, reliable and universal standard that justifies their use in the determination of unity of measure. State of the art Caesium fountains

can achieve a fractional uncertainty in the low 10^{-16} in determination of the SI second, with a measurement time of about 10 days.

1.3 Optical Clock

Research in the field of atomic clock [3] made possible to realize optical clocks whose operation process is similar to what is described in the previous section, but that use different atomic species like ytterbium (Yb), strontium (Sr), aluminum (Al) or mercury (Hg). The frequency reference is constituted by an atomic transition that belongs to the visible electromagnetic spectrum (from which the adjective *optical*) while ultra-stable lasers (instead of masers) are the local oscillator. Optical standard widely surpassed the performances of microwave standard of both fractional uncertainty (typically of the order of magnitude of 10^{-18}) [4] and stability and research brings these instruments to a continuous improvement of their performances.

They are diffused worldwide, allowing a network of international comparison [5] [6] [7] [8] [9]. For these reasons they are the highest rated candidates to a future redefinition of the second in SI [10], but this role is made possible only by the introduction of the optical frequency comb, because it enables to compare absolute measure of optical frequency with the microwave standards provided by caesium fountain, so with the current SI definition. Beyond a pure metrological application, they find employment in fundamental physics experiments where their extremely small uncertainty is required. Some examples are studies on time variation of fundamental constants [11], radio telescopes with VLBI (very long baseline interferometry) [12], quantum technologies [13], tests on general relativity [14] [15] and on chronometric geodesy [16] or to estimate the gravitational redshift [17] Another important advantage of optical clock is the lower clock instability: it is defined in term of Allan deviation [18] and for optical clock it is of the order of $10^{-5} \sqrt{\tau/\mathrm{s}}$, where τ is the measurement time, achieving in few hours results better than the ones of caesium fountains in tens of days of measurement.

It is possible to distinguish two categories of optical clocks based on the electric charge of the atoms: single ion and neutral atoms clocks. The first exploits the clock transition of a single atom that is confined in an electromagnetic trap, keeping it still where the field is null. This is the best possible realization of an unperturbed oscillator and presents advantages as a long interaction time and the absence of collisional and Doppler shift on energy levels. The seconds instead can not trap atoms using the Coulomb force, but use an optical lattice to trap them in a periodic potential. Differently from the previous case, because of the big number of trapped atoms they are affected by density shift due to collisions among different particles but enjoy the benefit of a large signal to noise ratio.

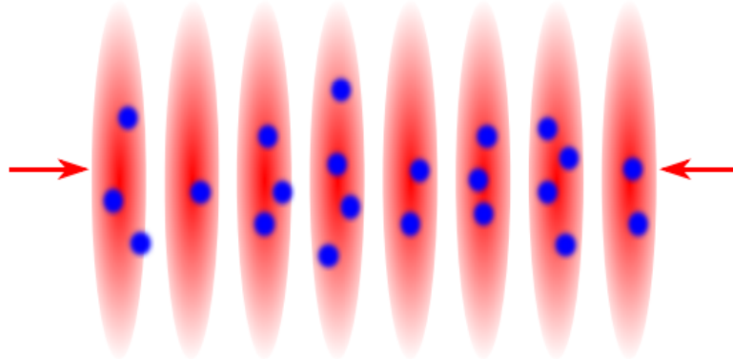### 1.3.1   Optical lattice and magic frequencies

Figure 1.3

The optical lattice is probably the main feature at the base of neutral optical clock operation. It consents to trap atoms cooled by magneto optic trap confining them to carry out the spectroscopy of the clock transition. It is an electromagnetic standing wave generated by a retro-reflected laser beam, so a periodic potential that sees a succession of consecutive nodes (zero laser power) and anti-nodes (maximum intensity of radiation). Depending on the laser wavelength, neutral atoms are attracted towards nodes or anti-nodes, where a potential hole arises trapping them, as schematized in fig.(1.3). One of the main advantages carried by the optical lattice with respect to a single ion clock is the big trapped neutral atoms: this is usually of the order of 1×10^4, obtaining a signal to noise ratio bigger than by a single atom. Trapping time longer than clock operation guarantees long interaction time between atoms and probe laser. For example I report the case of the ytterbium atomic clock It-Yb1, which will be discussed in detail in section (1.5), that has a lifetime in lattice of $2.7(1)$ s while the clock cycle period is about 277 ms. The role of atom confinement is to keep atoms as much as possible still, to reduce the Doppler effect on spectroscopy induced by the motion of the atomic ensemble. In Lamb-Dicke regime ($\sqrt{\Omega_r/\omega} \ll 1$, where Ω_r is the Rabi frequency o the transition and Ω_r is the lattice frequency [19]) the confinement is so tight that also recoil effect due to atom photon impact shifting energy levels are strongly reduced.

   Despite these advantages, immersing atoms in a non-resonant light field perturbes energy levels and influences the clock spectroscopy with the light shift. The solution to reduce this shift that limits clock performances, at least for its linear part, is to realize the lattice with a laser emitting at one of the possible magical wavelengths, characteristic of the considered atomic species.

1.4 INRiM

Figure 1.4

I performed my master thesis at INRiM laboratories (fig(1.4)). It is a public research institute that plays the role of national metrological institute for Italy and so, beyond other research themes, it takes care of definition, preservation and dissemination of SI units in our Country. I was welcomed in the group of "Quantum metrology and nanotechnologies", in particular in the "time and frequency" division, the research group that concentrates its efforts on realizing the primary and secondary standards of the second. Here are preserved atomic clocks like It-CsF2, the caesium fountain that provide the primary time standard for Italy (shown in fig.1.2) [20] and two optical lattice clock based on different atomic species, one on strontium (in progress) and the other on ytterbium. I will describe the second in more detail in the next section.
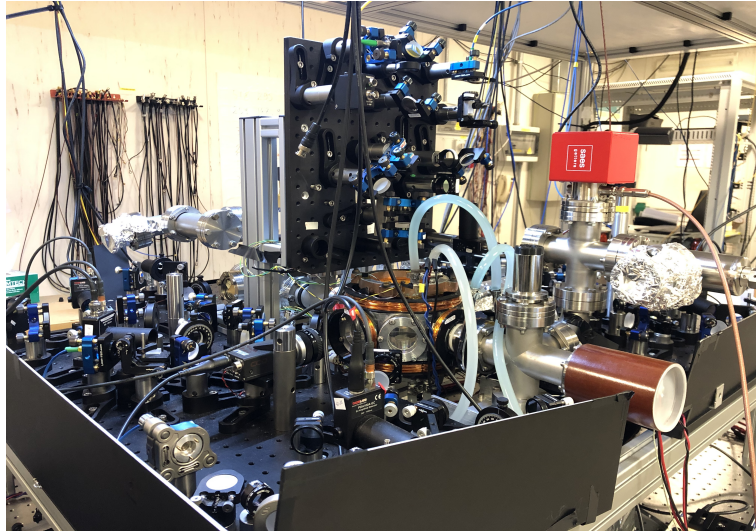
1.5 IT-Yb1

Figure 1.5: IT-Yb1

I worked on the ytterbium lattice clock IT-Yb1, shown in fig.(1.5) and located at INRiM laboratories. It is one of the first optical clocks worldwide that contributed to realization of International Atomic Time (TAI), providing the absolute measure of its optical frequency standard in 2019 [21]. It achieved in 2020 a fractional uncertainty of 2.7×10^{-17} with a stability expressed in term of Allan deviation equal to $3 \times 10^{-15} \sqrt{\tau}/\text{s}$ [22]

I describe here the main operating processes at the base of this optical clock, referring to the energy levels of neutral ^{171}Yb and to its more relevant involved transitions represented in fig.(1.6).
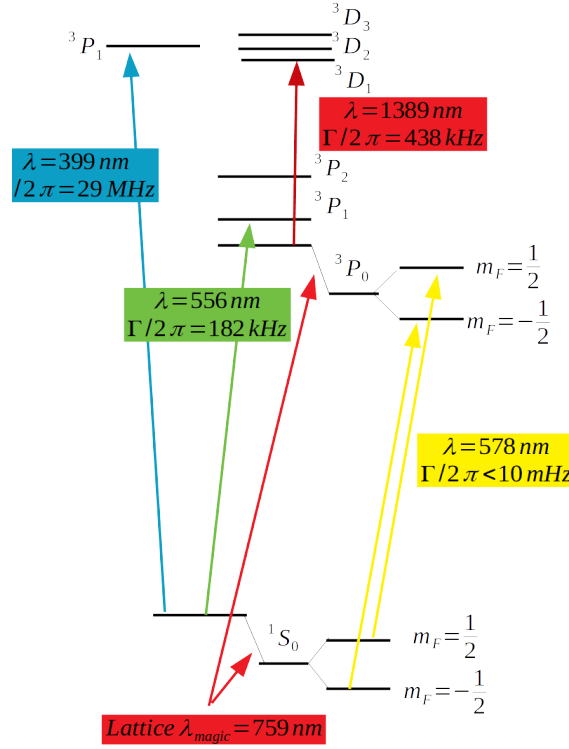
Figure 1.6: Energy levels and main atomic transitions of ^{171}Yb

- **Slower** 399 nm The atomic beam effused by an oven is slowed down by a counter-propagating blue light beam called *slower* exploiting the recoil effect.

- **First stage magneto optic trap** $^1S_0 \to^1 P_1$

  The magneto optic trap is realized with six counter propagating laser beams on the three space directions and turning on a magnetic field generated by coils. It is based on the phenomenon of laser cooling [24] to trap atoms up to a temperature of the order of ten millikelvin. It uses the strong $^1S_0(F = 1/2) \to^1 P_1(F = 3/2)$ transition excited with a laser of wavelength λ=399 nm, so with a blue/violet color.

- **Second stage magneto optic trap** $^1S_0 \to^3 P_1$

  Similar to the first stage, but uses the narrower transition $^1S_0(F = 1/2) \to^3 P_1(F = 3/2)$ with a wavelength of 556 nm, so the needed laser appears of green colour. It is split in three substages, the first transfer atoms from the precedent trap with high laser intensity, the second increases the gradient of magnetic field and reduces the laser intensity but moves the frequency close to resonance, decreasing atomic temperature down to $10\mu K$ while the third provides an enhanced transfer efficiency to confine atoms in the lattice.

- **Optical lattice** Cooled atoms are trapped in an optical lattice generated by a retro-reflected laser beam at 759 nm (so it appears red) being confined close to the maximum of radiation intensity. Atoms are loaded in lattice at low power while during the measure is possible to change laser intensity.

- **Single spin state polarization** $^1S_0(F = 1/2) \to^3 P_1(F = 3/2)$ Using the same transition of the second stage trap with a laser pulse at 556 nm and a magnetic field is possible to polarize the spin of the trapped atoms preparing a single spin state

- **Clock transition spectroscopy** $^1S_0 \to^3 P_0$ Spectroscopy of the clock transition is realized with a yellow laser emitting a 578 nm. A magnetic field splits the excited level for Zeeman effect following the two components $m_F = \pm 1/2$.

- **Detection** In this last process it is possible to estimate how many atoms have been excited on the clock transition. It is composed of three resonant pulses at 399 nm and then there is the collection of the atomic fluorescence with a photomultiplier. First pulse can measure how many atoms are in the ground state $^1S_0$, the second reveals the background signal from scattered light and hot atoms out of lattice while the third reveals the atoms excited during the Rabi spectroscopy. Before the third is necessary to repump atoms from the excited level $^3P_0$ to the ground state passing through the short-lived $^1D_0$ state using a laser emitting at 1389 nm.

In the following table I report the current uncertainty budget of this optical clock [21]:

Effect	Rel.shift x10^{17}	Rel.Unc.x10^{17}
Density Shift	-5,9	0,2
Lattice Shift	7,6	2,0
Zeeman shift	0,69	0,01
Blackbody radiation	236,7	1,3
Static Stark shift	1,6	0,9
Background gas shift	0,5	0,2
Others	-	1
Gravitational redshift	2599,5	0,3
Total	**2361,8**	**2,8**

Table 1.5.1: Uncertainty budget of the INRIM Yb lattice clock in fractional units as re-evaluated in 2019.

Currently main sources of uncertainty that limit clock performances are the Lattice shift and the Black body radiation shift.

1.5.1 Ti-sapphire VS TA laser diode

As discussed in section (1.3.1), to generate an optical lattice to trap neutral atoms in as much as possible imperturbated conditions it is necessary to have a narrow linewidth

centered on magic wavelength to minimize the lattice light shift. Moreover high power and frequency tunability are required to obtain a strong confinement (Lamb-Dicke regime) and because of the technique to obtain experimentally the magic frequency, based on alternating measure at high and low lattice power [25].

The light source typically used for this purpose in all optical clocks worldwide is a solid state Titanium:Sapphire laser, that has all these features. It presents an high spectral purity at high power and an emission tunable in a large wavelength range, but at the same time it is very delicate and susceptible to external stimuli (for example it is enough that a screw falls on the optical bench that the vibrations cause a change of oscillating mode on the laser and so a change of frequency). Moreover it requires high injection power and must be cooled to keep its temperatureconstant.

Amplified laser diodes are another laser source that can be a valid candidate to generate an optical lattice, because they are gifted of all the needed characteristics. Moreover they are preferables because of better qualities regarding their cheapness, transportability, size,weight and ease to use. They are reliable and compact, so perfect candidates for transportable or 24 h clock systems. Despite all these features, Ti:Sa lasers are the most used laser systems also for some transportable clocks [26], mainly because of the light shift induced by the amplified spontaneous emission.

1.5.2   Light shift problem

As already discussed, trapping ultracold atoms in an optical lattice finds many applications in different fields of atomic physics. It is necessary to take in account the ac Stark shift interaction between atoms and the radiation that perturbs them, whose effects are strongly reducible realizing the lattice with a narrow laser tuned at magic wavelength (in detail in section (2.1.6)). Real laser emission in general presents a broadband background spectrum distinct and detuned from the carrier: it is due to the phenomenon of amplified spontaneous emission (typically called ASE) and it can introduce a large and not well predictable light shift that could perturb the trapped atoms. Different laser systems present a different ASE spectrum, that depends from operational conditions and from the optical systems employed. Considering the Titanium:Sapphire laser it is almost irrelevant respect to the high power laser emission, discussing instead of laser diode this unwanted emission is not negligible. Moreover this kind of laser can not achieve alone power of the order of 1 W required to this purposes, so it is necessary to amplify them employing for example tapered amplifier (TA), semiconductor devices that introduce another important ASE source. This background can introduce a shift on the measured clock transition at Hz level or superior [27], making semiconductor lasers unusable for high accuracy application such as atomic clocks. For these reasons the Titanium:Sapphire performances are currently better despite all other disadvantages previously discussed, justifying their massive use also in transportable clocks.

1.6   Thesis work

During my master thesis I investigated the possibility of generating an optical lattice using a semiconductor laser to trap ultracold ytterbium atoms in the optical clock IT-

Yb1. The aim of this work is to limit the lattice shift induced by the ASE detuned from magic wavelength at the order of the low 10^{-18}, in order to not increase the actual uncertainty budget in determination of the frequency of the clock transition. This is a little investigated field in atomic clock research because, for the reasons previously discussed, Titanium:sapphire lasers are the main used laser sources. With this work I want to demonstrate that amplified laser diodes can be a valid replacement Ti:Sa systems, beyond that they can be able to be employed in developing new kinds of optical clocks to out-of-laboratory applications such as transportable [28], commercial or space.

Between the various possible solution to mitigate ASE effects, such as amplifier optimization [29], spatial filtering with optical fibers [30], absorption cells [31] or Fabry-Perot etalons [32], I chose to filter the TA spectrum with a Bragg grating to cancel out the detuned incoherent radiation trying to increase the TA spectral purity. In the second chapter of my thesis I report a simple theoretical model that I developed to estimate the maximum light shift induced by ASE. In chapter 3 I describe the experimental set-up that I realized to manipulate the laser beam of a tapered amplified laser diode, characterizing and filtering it with different systems. In particular I concentrate my efforts in studying the behavior of the radiation background of amplified spontaneous emission, that constitutes the main limit to the use of these lasers. In the fourth chapter I applied the theoretical model to the experimental data to estimate the ASE induced light shift while in the last chapter I show the experimental trapping of ytterbium atoms in the lattice realized with the laser system described in this work accompanied by the spectroscopy on the clock transition and a measure of the clock interleaved stability.

Chapter 2

Theoretical Background

2.1 Light Shift

Light shift [33], also called dynamic Stark shift, is a phenomenon observed when an atom interacts with a light field with frequency ω_L detund from the atomic transition frequency ω_A. This perturbation causes a shift on atomic energy levels, so a shift on the measured transitions and for this reason it must be reduced in atomic clock to keep atoms in as much as possible unperturbed conditions.

2.1.1 Atomic response

I consider an atom in a laser field of frequency ω_L far enough away from atomic transition frequencies ω_{eg}, with intensity of electric field E_0. This non-resonant radiation causes an atomic response in the form of generation of an atomic electric dipole moment induced by oscillating field expressed by:

$$\vec{D}(t) = \alpha(\omega_L)\vec{E}_0 cos(\omega_L t) \tag{2.1}$$

where $\alpha(\omega_L)$ is the dynamic polarizability of the atom at frequency ω_L.

The atomic dipole couples itself with the same radiation that induces it: this phenomenon generates a potential energy U_0 and so a shift in energy levels $\hbar\delta_g$. It can be expressed by the time mean of the product between electric field and induced mean dipole:

$$\hbar\delta_g = -\frac{1}{2}\left\langle \vec{D}(t) \right\rangle \vec{E}_0 cos(\omega_L t) = -\frac{1}{4}\alpha(\omega_L)E_0^2 \tag{2.2}$$

dependending on the dynamic polarizability and on the field intensity to the second power. Moreover, if the potential of interaction has a space dependence, atoms undergo a force $\vec{F} = -\vec{\nabla}U_0 = 1/4\alpha\vec{\nabla}E_0^2$: this is conservative and acts by confining atoms toward the minimum of potential. Electric field role in trapping atoms is now clear: on the one hand it generates an atomic dipole moment, on the other, coupling with dipole, generates also the potential that keeps atoms confined.

2.1.2   Quantum Description

Starting from a "dressed atom" [24] like approach to describe atom-photon interaction it is possible to obtain a more accurate description of the light shift.

Assuming a two level atom composed of a ground state g and an excited state e (with natural linewidth Γ) they are separated in energy by the quantity $E_e - E_g = \hbar\omega_{eg}$. It is possible to define the detuning $\delta = \omega_L - \omega_{eg}$ between the laser frequency and the atomic resonance. The system atom-light is describable introducing the two-dimensional perturbate states $|1(N)\rangle$ e $|2(N)\rangle$, also called dressed states [24]. They are expressed as linear combinations of the uncoupled quantum states $|g, N+1\rangle$ e $|e, N\rangle$, where N is the photon number of the light beam that perturbes the atom. If the atom in g absorbs a photon transiting to e, the states $|g, N+1\rangle$ e $|e, N\rangle$ are coupled with interaction potential V_{AL}. So:

$$\langle e, N|\, V_{AL} \,|g, N+1\rangle = \langle e, N|\, \mu_E \,|g, N+1\rangle\, E_L = \frac{\hbar\Omega_R}{2} \qquad (2.3)$$

where Ω_R is the Rabi frequency of the atomic transition, that depends on the intensity of the electric field E_L and from the operator atomic dipole moment μ_E between the two states . Time evolution is described by the effective Hamiltonian for dressed states:

$$H_{eff} = \hbar \begin{pmatrix} \delta & \frac{\Omega}{2} \\ \frac{\Omega}{2} & -i\frac{\Gamma}{2} \end{pmatrix}$$

(2.4)

where the imaginary term accounts the indetermination of the excited state energy. Considering energy like a complex quantity, it is necessary to use the modulus of the energy difference. Working in weak coupling limit, $\Omega \ll |\delta + i\Gamma/2|$, valid for weak light intensity or far detuning, I can apply a perturbative theory to obtain the expressions of the two dressed states :

$$|1(N)\rangle = |g, N+1\rangle + \frac{\Omega}{2(\delta + i\Gamma/2)}\,|e, N\rangle\,;\ |2(N)\rangle = |e, N\rangle - \frac{\Omega}{2(\delta + i\Gamma/2)}\,|g, N+1\rangle\,;$$

(2.5)

and the energy shift between coupled and unperturbed states is:

$$\delta E_{1N} = \hbar\frac{\Omega^2}{4\delta + i\Gamma/2} = \hbar\delta_g - i\hbar\frac{\gamma_g}{2}\,;$$
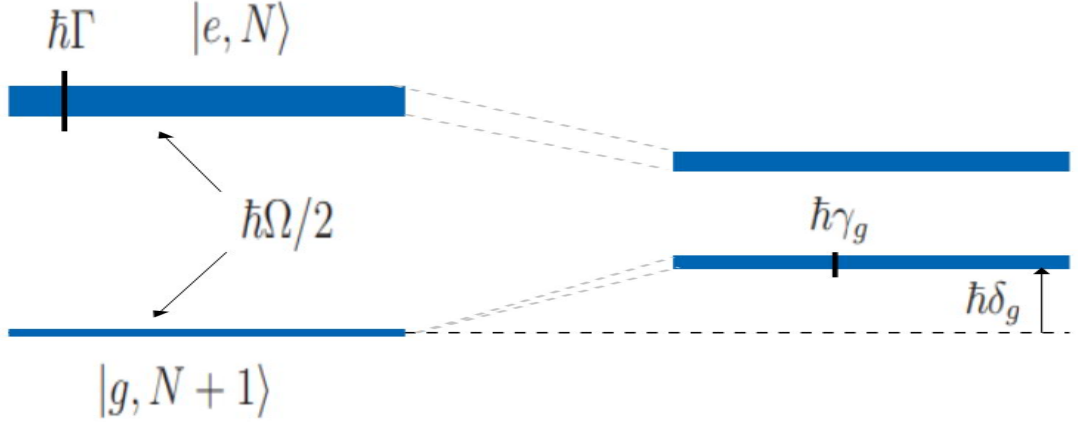
(2.6)

Figure 2.1: LEFT uncoupled states, RIGHT coupled dressed states. The atom-photon coupling shifts the level $|g, N+1\rangle$ by an amount $\hbar\delta_g$ and broads it absorbing instability from excited state of an amount $\hbar\gamma_g$

$$\delta E_{2N} = -\hbar\delta_g + i\hbar\frac{\gamma_g}{2} \tag{2.7}$$

where the real part represents the shift of the energy levels, instead the imaginary one is related to the energy broadening of the state. The term δ_g is called *light shift* and is expressed by:

$$\delta_g = \frac{\delta}{4\delta^2 + \Gamma^2}\Omega^2 \tag{2.8}$$

while γ_g is called *light broadening* and is expressed by:

$$\gamma_g = \frac{\Gamma}{4\delta^2 + \Gamma^2}\Omega^2 \tag{2.9}$$

It represents the broadening of the ground state due to the instability of the excited coupled state, that reduces its natural linewidth of the same amount. These quantities are dependent on the Rabi frequency Ω, related to the light field that couples the two states and so they are proportional to the light intensity that perturbes the atoms.

The effects of coupling due to light perturbation on atomic states are schematized in figure 2.1: energy levels are shifted of the amount $\hbar\delta_g$ in a opposite way, moreover the ground state absorbs part of the instability of the excited one, broadening of an amount $\hbar\gamma_g$ while the other is reduced by the same quantity.

I will concentrate on the description of the light shift in the limits of large detuning $|\delta| \gg \Gamma$, where the expressions (2.8) e (2.9) become respectively:

$$|\delta_g| = \frac{\Omega^2}{4|\delta|}; \quad \gamma_g = \frac{\Omega^2\Gamma}{4\delta^2} = |\delta_g|\frac{\Gamma}{|\delta|} \ll \delta_g; \tag{2.10}$$

So in this limit and at this level of approximation the light broadening is negligible compared to light shift.

2.1.3 Multi-level Atom

I can generalize the previous expression of the light shift δ_g of the state g for of a multi-level atom in the far detuning limit. In this case I can't consider only one transition $g \to e$, but I must take in account all the possible excited states coupled by electric dipole allowed transitions. So I must study the transition for which the electric dipole operator $\langle e| \hat{\mu}_E |g\rangle = D_{eg} \neq 0$.

Equation (2.10) becomes:

$$\delta_g = \Sigma_k \frac{E_0^2 |\langle e| \mu_E |g\rangle|^2}{\hbar(\omega_L - \omega_{eg})} \tag{2.11}$$

where I replaced the expression for Rabi Frequency from (2.3) and ω_{eg} is the frequency associated with the $g \to e$ transition. I extend the model considering not only the transitions for which the atoms go to an higher state by absorbing a photon ω_L, but also those for which the transition occurs by emitting a stimulated photon at frequency ω_L [19]. For the first case the energy variation of the atom is $E_g - (E_e - \hbar\omega_L) = \hbar(\omega_L - \omega_{eg})$, so the denominator of expression(2.11) while in the second is $E_g - (E_e - \hbar\omega_L) = -\hbar(\omega_L + \omega_{eg})$. This second phenomenon can be neglected when ω_L is close to the resonance ω_{eg} (rotating wave approximation), giving only a perturbative contribution to the light shift of the g level. Considering also this contribution I can correct the equation (2.11) writing:

$$\delta_g = \frac{1}{4\hbar^2}\Sigma_e \left\{ \frac{|D_{eg}|^2 E_0^2}{\omega_L - \omega_{eg}} - \frac{|D_{eg}|^2 E_0^2}{\omega_L + \omega_{eg}} \right\} = -\frac{E_0^2}{4\hbar}\left\{ \Sigma_e \frac{2|D_{eg}|^2}{\hbar} \frac{\omega_{eg}}{\omega_{eg}^2 - \omega_L^2} \right\} \tag{2.12}$$

2.1.4 Dynamic polarizability

I rearranged this expression (2.12) at the right side to underline the similarity with the expression of light shift (2.2) derived from atomic response. To isolate the terms in brackets allows me to derive the following expression for the dynamic polarizability of the atomic level identified with index g, $\alpha_g(\omega_L)$ as the laser frequency ω_L changes:

$$\alpha_g(\omega_L) = \frac{2}{\hbar}\Sigma_e |D_{eg}|^2 \frac{\omega_{eg}}{\omega_{eg}^2 - \omega_L^2} \tag{2.13}$$

Like the light shift, it is clear that also $\alpha_g(\omega_L)$ is influenced by the atomic excited states that can couple with g by electric dipole transitions. So, to obtain a realistic expression of dynamic polarizability, I must study what are these excited states knowing the frequencies ω_{eg} of the associated transition and the elements of dipole matrix $D_{eg} \neq 0$. The first are easy to find tabulated in literature, both from theoretical calculations or from experimental measurements while the seconds can be obtained from quantum mechanics calculations or derived experimentally considering the damping rate of spontaneous emissions Γ_{eg}. Considering the process of spontaneous emission from the excited state e to ground state g, the probability of this transition is expressed by:

$$\Gamma_{eg} = \frac{\omega_{eg}^3 |\langle e| \mu_E |g\rangle|^2}{3\pi\epsilon_0 \hbar c^3} \tag{2.14}$$

Replacing equations (2.14) in (2.13) I obtain:

$$\alpha_g(\omega_L) = 6\pi\epsilon_0 c^3 \frac{\Gamma_{eg}}{\omega_{eg}^2(\omega_{eg}^2 - \omega_L^2)} \tag{2.15}$$

Moreover Γ_{eg} can be expressed as a function of the lifetime of the excited state τ_e and of the branching ratio ϕ_{eg} of the $e \rightarrow g$ transition in the form:

$$\Gamma_{eg} = \frac{\phi_{eg}}{\tau_e} \tag{2.16}$$

where the branching ratio, related to the probability that the electron decays in the state g and not in another, are obtained from theoretical calculations that involve angular momentum while lifetimes are measurable.

2.1.5   Allowed transitions

I searched the excited atomic states of the atom ^{171}Yb that can couple with the clock states $^1S_0$ and $^3P_0$ with allowed dipole transitions, influencing the dynamic polarizability. I reported in tab:(2.1.1) and tab:(2.1.2) the parameters of energy, lifetime and branching ratio associated with these transitions.

$^1S_0$			
Quantum State	Energy (cm^{-1})	Lifetime (ns)	Branching Ratio
6s6p $^1P_1$ [34]	25068.222	5.464	1
6s7p $^1P_1$ [34]	40563.97	9.2	0.80
6s8p $^1P_1$ [34]	44017.60	43	0.65
6s6p $^3P_1$ [35]	17992.007	866(7)	1
(7/2, 5/2)j=1 [34]	28857.014	14.6	1

Table 2.1.1: Atomic States involved in the calculation of the Dynamic Polarizability of $^1S_0$ with their main parameters.

$^3P_0$			
Quantum State	Energy (cm^{-1})	Lifetime (ns)	Branching Ratio
6s7s $^3S_1$ [36]	15406.253	14	0.15
6s8s $^3S_1$ [36]	24326.601	34	0.135
6s5d $^3D_1$ [35]	7200.663	329(7)	0.639
6s6d $^3D_1$ [36]	22520.281	21	0.582
6s7d $^3D_1$ [36]	27022.941	38	0.56
$6p^2$ $^3P_1$ [36]	26516.981	15	0.35

Table 2.1.2: Atomic States involved in the calculation of the Dynamic Polarizability of $^3P_0$ with their main parameters

Using these data I could calculate the dynamic polarizability $\alpha(\lambda_L)_{^1S_0}$ and $\alpha(\lambda_L)_{^3P_0}$ of the ytterbium clock states applying the expression (2.15). I reported the results in fig.2.2.
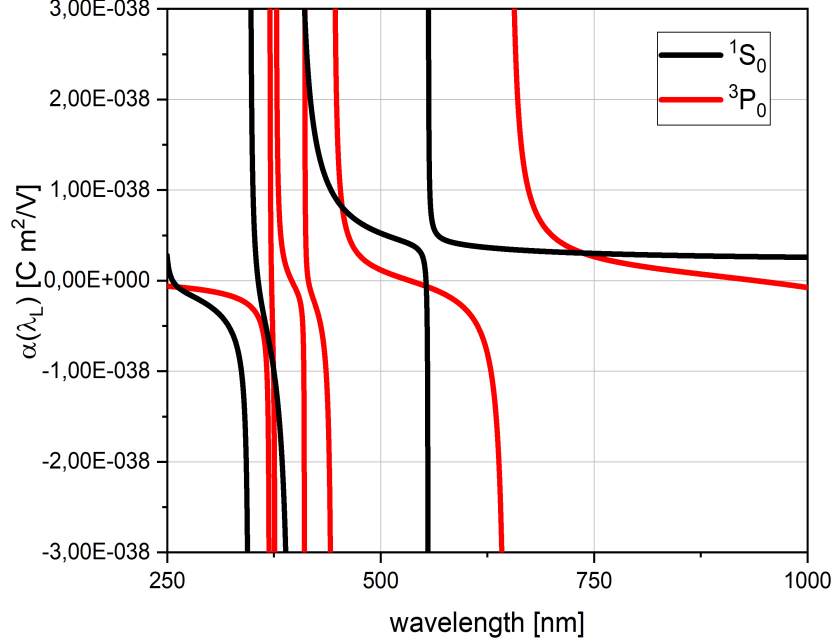

Figure 2.2: Ytterbium clock states dynamic polarizability as change the laser wavelength

From this chart I can see that in far detuned approximation there are asymptotes close to atomic resonances, so this expression is valid only for lattice frequencies far from atomic transitions. Moreover it is evident that for particular wavelengths the polarizability of two states is equal: these are called *magic wavelengths* [37] and are used to delete the light shift in optical lattice clocks. The choice of the wavelength to use is determined by laser availability and distance from atomic resonances. For the ytterbium atomic clock the one at right of the chart, measured experimentally at $\lambda \simeq 759, 35nm$, is used usually to generate the lattice: from my calculation the point where the two curves intersect is located about $737nm$, so far from experimental value. I tried to correct the model that I developed to fit it with experimental results: so I considered a further transition that involves atomic states in the shell $4f$ that can couple with $^3P_0$ [38]. The energy associated with this transition is known and its value is $E = 37414.59cm^{-1}$, instead the branching ratio and lifetime are difficult to measure. I added to the expression of $\alpha(\omega_L)$ of $^3P_0$ a term that takes in consideration this further transition in the form:

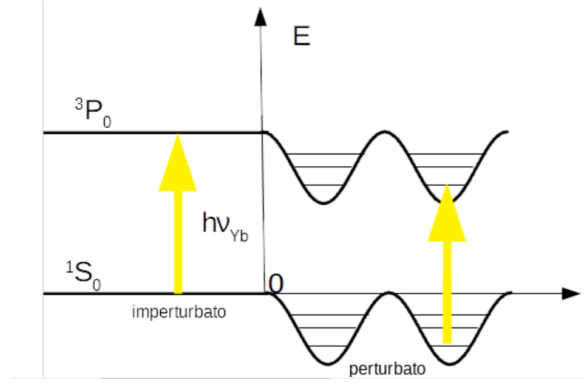$$\Delta\alpha = \frac{A}{\omega_{eg}^2(\omega_{eg}^2 - \omega_L^2)} \tag{2.17}$$

Figure 2.3: Graphical representation of lattice effects on Ytterbium clock states.LEFT imperturbate situation. RIGHT energy levels perturbed by a periodic potential. Close to the nodes electric field is null so there is no shift, instead close to antinodes, where the field is maximum, the bending of energy levels generates a series of potential holes that trap atoms that populate different energy levels of harmonic trap.

where ω_{eg}^2 is the frequency of transition and is obtained from energy with $\omega = 2\pi cE$ and A is a fitting parameter to adapt the model with the measured value. I found $A = 2,608912 \cdot 10^8 s^{-1}$ and I applied this to build a theoretical model similar to experimental results with magic wavelength located around $759,35nm$.

2.1.6 Lattice Light Shift

Knowing now the effects of a non-resonant laser on atoms and an expression for dynamic polarizability of the clock states, I can apply this model to obtain an estimation of the light shift induced on ytterbium atoms trapped into an optical lattice. Optical lattice is a standing wave generated by a retro-reflected laser, so it creates a periodic potential coupling with atomic polarizability that induces a shift of the energy levels. Like represented in picture 2.3, close to antinodes (where the intensity of electric field is maximum) holes of potential arise that trap atoms.

Considering the hypothesis of standing wave generated by an oscillating electric field $\vec{E} = \vec{E}0cos(\omega t)$, the intensity of the electric field at the anti-nodes is equal to $2E0$. I can calculate the intensity of the electromagnetic radiation using the Poynting Equation:

$$I = \frac{1}{2}\epsilon_0 cE^2 \qquad (2.18)$$

Starting from these assumptions intensity close to anti-nodes it is:

$$I = 4I_0 \qquad (2.19)$$

where $I_0 = 1/2\epsilon_0 cE_0^2$ is the intensity of the incident radiation. In the hypothesis that ASE radiation is not coherent and so it does not generate an interference pattern, I should consider ASE intensity in the lattice $I = 2I_0$, by the sum of the two counter-propagating waves. Since I do not know how much ASE is coherent and for

my calculation I am interested in estimating the maximum light shift on atoms, I decide to use the expression (2.19) also for this effect and not only for the coherent laser emission, as a pessimistic approach.

Supposing that laser beam that generate the lattice is Gaussian that propagates along the z-axis, the radius $w(z)$ change following the law $w(z) = w_0\sqrt{1 + (z/z_R)^2}$, where w_0 is the beam waist (minimum radius) and $z_R = \pi w_0^2/\lambda_L$ is the Rayleigh range, where the laser beam is considered focalized. In the (x, y) plane, perpendicular to propagation direction, the intensity of radiation is distributed following a Gaussian profile $exp(2r^2/w(z)^2)$ and at the maximum it is equal to:

$$I_L = \frac{2P_L}{\pi w_0^2} \tag{2.20}$$

where P_L is the laser power that generate the lattice and w_0 is the beam waist.

Substituting the expression (2.20) in (2.19) I can obtain the intensity of radiation at the maximum of anti-nodes of the lattice:

$$I = 4\frac{2P_L}{\pi w_0^2} \tag{2.21}$$

This can be useful to reformulate the expression for light shift as a function of the laser power instead of electric field intensity, so a quantity easy to measure. Light shift becomes:

$$\delta_g = -\frac{1}{4\hbar}\alpha(\omega_L)E^2 = -\frac{1}{2\hbar\epsilon_0 c}\alpha(\omega_L)I = -\frac{4\alpha(\omega_L)P_L}{\epsilon_0\hbar c\pi w_0^2} \tag{2.22}$$

.

2.1.7 Transition shift

Knowing how different atomic states change their energy in function of lattice wavelength and intensity, it is possible to calculate the frequency shift of the clock transition as the difference of light shift of the two involved states $^1S_0 \to ^3P_0$, obtaining the expression:

$$\Delta\nu = -\frac{1}{2\epsilon_0 ch}(\alpha_{^3P_0} - \alpha_{^1S_0})I \tag{2.23}$$

where the lattice intensity is expressed by (2.20) using the parameters P=1 W and a waist w_0 =45 μm. These have been chosen to simulate the real parameters of the optical lattice present in IT-Yb1.

The results that I obtained are reported in fig.(2.4).

Close to the magic wavelength the dynamic polarizability of the two levels, and consequently the light shift, is the same. In these conditions, if both levels are shifted of the same quantity, the difference of light shift is zero and so there is no lattice shift on the clock transition [39]. So if I want to trap atoms in a lattice keeping them in as much as possible unperturbed conditions, I must realize the optical lattice with a laser emitting at the magic wavelength. The choice among all the possible ones is determined mainly by two factors: the availability of tunable laser emitting at this wavelength and how the derivative of the difference between atomic polarizability of the two levels is flat. In fact a small wavelength variation around magic one does not
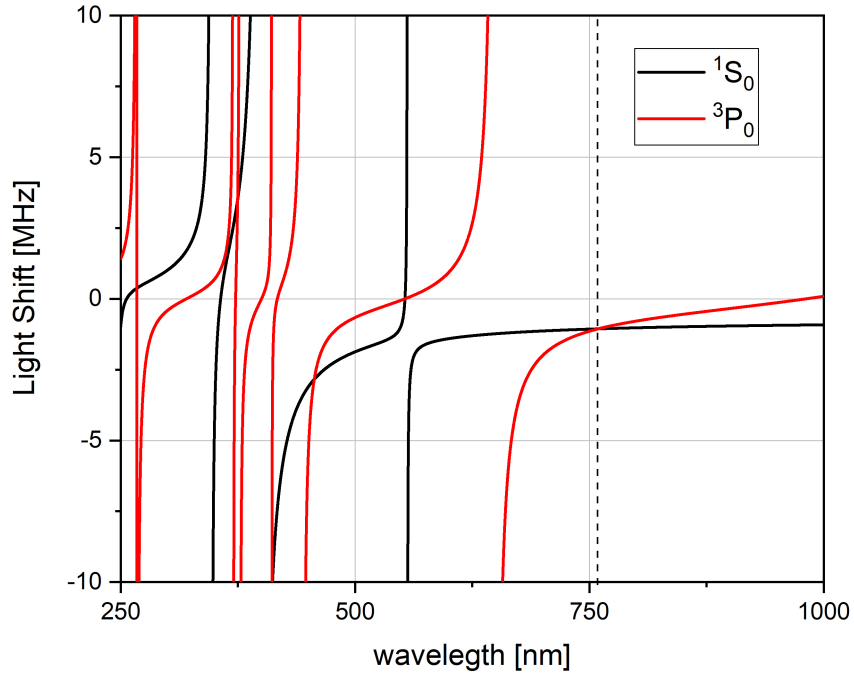
Figure 2.4: Theoretical lattice shift for clock states $^1S_0$ and $^3P_0$ with lattice power $P = 1W$.

change significantly the induced light shift, while near atomic resonances the curves are very steep, requiring high laser stability. The most used magic wavelength worldwide is the one at about $759\,\mathrm{nm}$, so the rightmost one in fig.2.4 and for my work I will concentrate on that.

2.1.8 Comparison with experimental data

Before using the model I developed in the previous section I compare it with experimental results to estimate how much it is reliable. Experimental data of the light shift as a function of the detuning from the magic frequency are fitted with a linear or a parabolic model, extracting two fitting parameters. For this reason I expanded my theoretical model as a second order Taylor series close to the magic frequency (about $394\,798.261(1)\,\mathrm{GHz}$) as a function of the detuning. In tab.2.1.3 I report the comparison between experimental and theoretical parameters of the light shift:

$\Delta\nu_{LS} = a \cdot \nu + b \cdot \nu^2$		
	a/($mHz/GHz/E_r$)	b/($mHz/GHz^2/E_r$)
Pizzocaro 2017 [23]	-27(3)	-0,16(3)
Nemitz 2019 [40]	-25,7(5)	–
This work	-28	-0,16

Table 2.1.3: Comparison between theoretical and experimental parameters that describe the light shift as a function of the detuning from the magic frequency. Values expressed in experimental units. $E_R = h\nu_R$ is the recoil energy of ^{171}Yb at magic wavelength where $\nu_R \simeq 2$kHz.

It is possible to observe that the Taylor parameters extracted by my theoretical work are compatible within the uncertainties with the measurements in the first line [23], while with respect to the results reported in the second line [40] they are similar even if not compatible. I can say that my model is quite acceptable within this level of approximation, so It can be applied to estimate the shift on the clock transition induced by the electric dipole polarizability.

2.1.9   Light Shift Problem

What I discussed here is only a part of the more complex problem of estimating the lattice induced light shift that perturbs the study of the clock frequency. I started to consider the contribution provided by the electric dipole polarizability because it is the more relevant part to this systematic uncertainty, but there are other phenomena involved and further terms that depend not linearly from the lattice intensity, moving the magic frequency from the one I calculated in the previous section.
A more complete expression for the light shift is the following [41]:

$$h\Delta\nu_{LS} = \left(\frac{\partial\Delta\alpha^{El}}{\partial\nu}\delta\nu - \Delta\alpha^{qm}\right)(2n+1)\sqrt{\frac{E_r}{4\alpha^{E1}}}I^{1/2} - \left[\frac{\partial\Delta\alpha^{El}}{\delta}\nu + \Delta\beta(\xi)(2n^2+2n+1)\frac{3E_r}{4\alpha^{El}}\right]I$$

$$+\Delta\beta(\xi)(2n+1)\sqrt{\frac{E_r}{4\alpha^{E1}}}I^{3/2} - \Delta\beta(\xi)I^2$$

$$(2.24)$$

The electric dipole light shift is represented by the term $\partial\Delta\alpha^{El}/\partial\nu\delta\nu$, the linear coefficient of my model, $\delta\nu$ is the detuning from the electric dipole magic frequency at $\Delta\alpha(\omega_L)^{El} = 0$ (the one obtained previously) and α^{El} is the electric dipole atomic polarizability. After that it is necessary to consider effects from other atomic parameters that generate terms of superior orders: the ones present in this formula are $\Delta\alpha^{qm}$, the differential multipolar polarizability and $\Delta\beta$, that represents the hyperpolarizability effects. The dominant term is the one that depends linearly on the lattice intensity and its main contributor is the differential electric dipole polarizability: it is possible to minimize this light shift tuning the lattice laser on the magic frequency that cancels out the electric dipole effect. For fractional uncertainty of the order of 1×10^{-17} it is necessary to take in account also the other terms that introduce a non negligible

systematic shift, and the dominant terms depend on the lattice intensity (at low power prevails the term $\propto I^{1/2}$ while at high power the terms $I^{3/2}$ and I^2). Other parameters present in equation (2.24) are n, the average motional state occupation in the lattice and ξ, the degree of circular polarization of light that influence the hyperpolarization. It is not possible to find a magic position that can cancel out the contribution of all the four terms that depend on different powers of the lattice intensity, because they are not null at magic wavelength. There will be always a lattice shift that one can only try to minimize acting on the different parameters $\delta\nu$, n and ξ.

For the purpose of studying the light shift induced by the amplified spontaneous emission it will be sufficient to consider only the electric dipole contribution linearly dependent on the light intensity: in fact for radiation detuned from magic wavelength it is the more important contribution. Regarding the narrow laser emission instead, it is necessary to take in account all the possible contributions, because the dominant term is suppressed by the tuning.

2.2 Amplified Spontaneous Emission

The phenomenon of Amplified Spontaneous Emission (ASE) [42] becomes very relevant when the active medium is optically dense and the gain $G = exp\sigma(N_2 - N_1)/l$ is large enough. In a typical laser the resonant photons move in the cavity being amplified every time they pass through the active medium. Working in these conditions also fluorescence generated by spontaneous emission at non-resonant wavelength can be strongly amplified in a single pass (it can not survive in the cavity if it is detuned from the resonant frequencies). This generates a broadband spectrum with intermediate properties between laser and spontaneous emission radiation: it shows a certain level of directionality and coherence but a linewidth larger than laser but narrower than the spectrum of spontaneous emission.

I am interested in studying the spectral distribution of ASE intensity. The theory is rather complex but with some approximations it is possible to obtain a valid expression to describe it [43]. I consider a four level active medium in low saturation regime, so the upper state population is not appreciably saturated by ASE. I suppose that the active medium is shaped as a cylinder of length l and the laser beam propagates along the z-direction, parallel to cylinder axis.

If $I_\nu(z, \nu)$ is the ASE spectral density at coordinate z, the elemental variation dI_ν along the z axis is :

$$\frac{\partial I_\nu}{\partial z} = \sigma N I_\nu + N A_\nu \frac{\Omega(z)}{4\pi}$$

(2.25)

where N is the inversion of population, σ is the cross section at frequency ν, A_ν is the rate of spontaneous emission, $\Omega(z)$ is the solid angle subtended by the exit face

as seen from the element dz. The first term on the right part represents the effect of stimulated emission that amplifies the radiation, while the second represents the spontaneous emission contribution. Spontaneous emission is generated isotropically, so I must consider only the fraction of solid angle that corresponds to the photons that cross the whole cylinder length. Most of the ASE radiation derives from photons emitted close to the beginning of the active material, so I can assume Ω as constant.

Imposing the boundary condition $I_\nu(0, \nu) = 0$ and integrating over the space coordinate from 0 to l (active medium length) I obtain:

$$I_\nu(l, \nu) = \frac{\Omega}{4\pi} A_\nu \frac{h\nu[exp(\sigma Nl) - 1]}{\sigma} \qquad (2.26)$$

I can rearrange (2.26) using $A_\nu = A \cdot g(\nu - \nu_0)$ and $\sigma = \sigma_p \cdot g(\nu - \nu_0)/g_p$, where A is the rate of spontaneous emission, $g(\nu - \nu_0)$ is the lineshape of the transition, g_p and σ_p are the peak value of transition and of cross section while ν_0 is the central frequency of the transition.

This way, equation(2.26) become:

$$I_\nu(l, \nu) = \phi I_s \frac{\Omega}{4\pi} g_p h\nu[exp(\sigma Nl) - 1] \qquad (2.27)$$

where ϕ is the fluorescence quantum yield and $I_s = h\nu/\sigma_p\tau$ is the peak saturation intensity of the amplifier.

The term in brackets can be approximated as:

$$[exp(\sigma Nl) - 1] \simeq [exp(\sigma_p Nl) - 1] \cdot exp(-kx^2) \qquad (2.28)$$

where x is the normalized frequency offset :

$$x = \frac{2(\nu - \nu_0)}{\Delta\nu_0} \qquad (2.29)$$

and $\Delta\nu_0$ is the transition linewidth. The constant k instead depends on the kind of line broadening process: for Gaussian line $\sigma = \sigma_p exp(-x^2 ln2)$ and:

$$k = ln(2)\frac{Gln(G)}{G - 1}$$

(2.30)

where G is the peak value of the gain. It is now possible to obtain the ASE linewidth: in gaussian approximation the normalized frequency offset linewidth is $\Delta x_{ASE} = 2\sqrt{ln2/k}$ and applying equation (2.29) $\delta_{\nu ASE} = \Delta x_{ASE} \cdot \Delta\nu_0/2$. Replacing the value of k obtained in expression(2.2) for gaussian line:

$$\Delta\nu_{ASE} = \sqrt{\frac{G - 1}{Gln(G)}} \Delta\nu_0$$

(2.31)

When the gain of the active medium increases the ASE linewidth becomes narrower than the case of pure spontaneous emission.

Substituting eq.(2.2) and (2.2) in (2.28) and collecting the constant terms I can obtain the approximated expression or the spectral ASE distribution:

$$I_\nu = const \cdot \nu \cdot \exp\left(-\frac{(\nu - \nu_0)^2}{\Delta\nu_{ASE}}\right)$$

(2.32)

Chapter 3

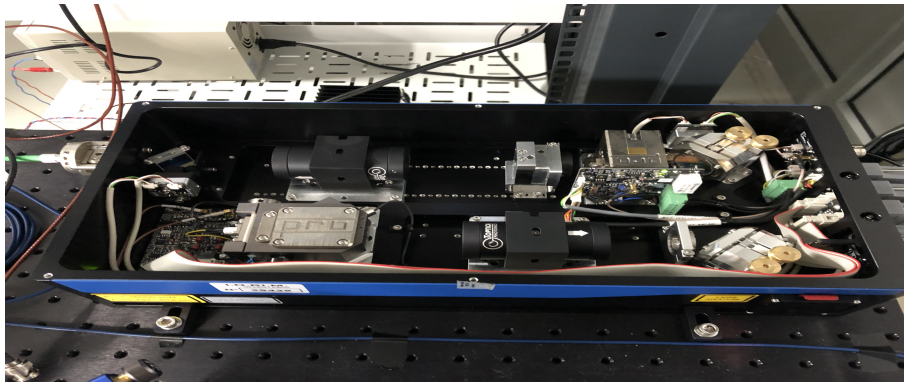# Experimental work

3.1 Tapered amplified laser diode DLC pro TA 759nm

Figure 3.1: DLC pro TA 759nm without cover

The light source that I used to generate the optical lattice in my work is the semiconductor laser DLC pro TA 759nm provided by Toptica, composed by a laser diode and a tapered amplifier, represented in fig.(3.1). In the scheme in fig.(3.2) are shown the main elements that compose this instrument.

- **Extended Cavity Diode Laser (ECDL)** The tunable laser diode that emits light. The optical power is controlled by the current injection. It is possible to tune the frequency of the laser emission acting on the injection current or tilting mechanically the grating of the extended cavity.

- **Optical (or Faraday) Insulators** Discussed in detail in section:3.5.1. They are used to protect the optical elements from eventual harmful retro-reflected beams and to linearize horizontally the output polarization.

- **Alignment mirrors** A couple of mirrors used to inject diode radiation toward the amplifier, modulating the power. Moreover the space mode of emission of the amplified beam depends on the vertical alignment.
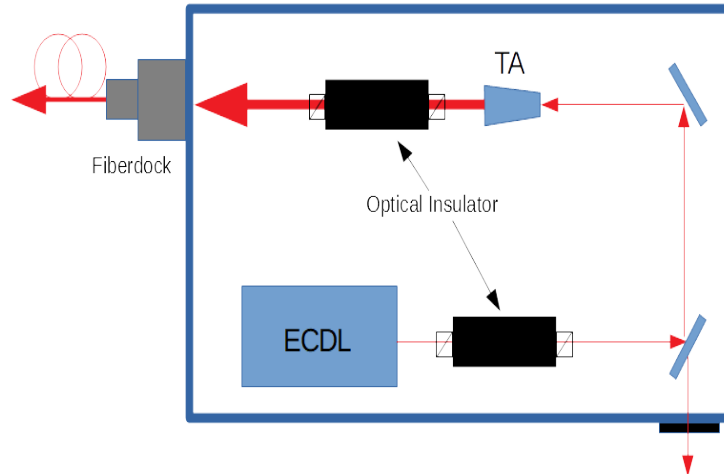
Figure 3.2: Scheme of the internal laser components.

- **Tapered Amplifier (TA)** A semiconductor device that amplifies the laser input. Name derives from its shape, because the dimension increases with optical power in a funnel-like form. It is pumped with the injection current that determines the laser output power.

- **Fiberdock** pre-aligned system to couple in the optical fiber the laser power generated by the TA. It presents a collimating lens that can move coarsely in a guide to focus the laser in the optical fiber [44]. Further adjustments are possible acting on three screws that move finely the lens on the three space direction to maximize the coupling efficiency.

As previously described, I can control the optical power of the laser acting on the injection current of both the diode and the amplifier. This laser is tunable in a wavelength range included between 758.5 nm and 778.9 nm: coarse tuning is possible tilting mechanically the grating of the extended cavity while fine adjustments are controlled by a piezoelectric element controlled by an electric voltage provided by the laser controller. While the amplified laser beam goes out from the laser system through optical fiber, there is a side window through which a small fraction of the diode emission is sent out allowing to sample the injection laser.

I characterized the DLC pro TA 759 emission power varying the injection current of the diode and of the amplifier. I measured the amplifier power with a Thorlabs power meter S130C positioned out of the side window and the second out the fiberdock, after I removed the optical fiber. Using the laser controller I read and modified the injected current. Results are reported in fig.(3.3).
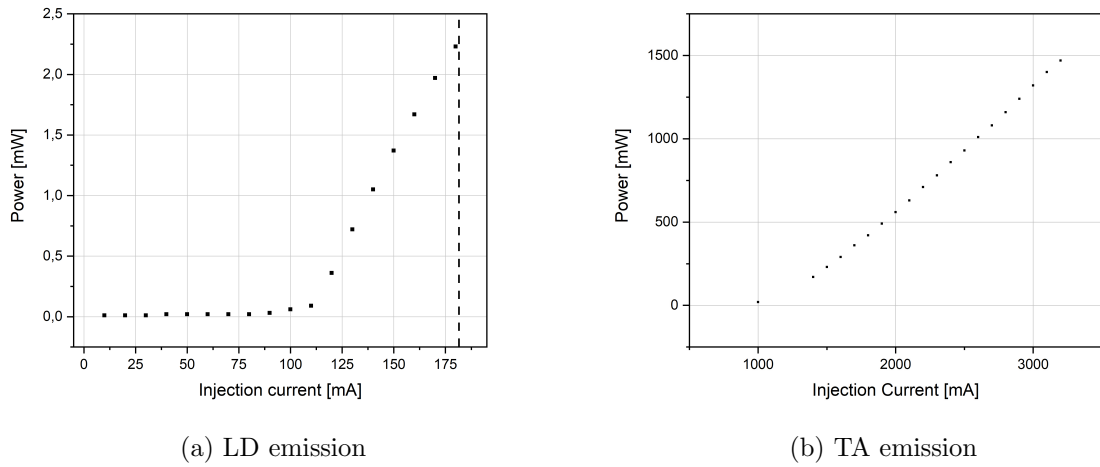
(a) LD emission

(b) TA emission

Figure 3.3: Optical power emitted varying the injection current by diode and amplifier with I_{diode}=181 mA

I fitted the data in in figure (3.3a) and I estimated the threshold current of the diode equal to I=108(2) mA. It is possible to observe that only beyond this value the diode emits laser power instead of incoherent photons from spontaneous emission (such as a LED), so the emitted power increases strongly. From the fit I also estimated a slope efficiency of 3.12(5) mW/mA, taking in account that it is only the small fraction of the total diode power that is not sent to the amplifier. I observe for TA emission a threshold current of about 1300 mA and fitting these data I estimated a slope efficiency equal to 0.738(6) mW/mA with a maximum power at 3200 mA of 1.47(1) W.

3.1.1 Beam shape

I removed the fiberdock from the exit window of the laser system and I studied the shape and the space evolution of the laser beam section. I used a beam profiler provided by Thorlabs, i.e. a ccd camera, to observe the beam shape obtaining a false colour imaging. Like shown in figures (3.4a) and (3.4b), the shape of the beam emitted by the amplifier is very different from the ideal gaussian mode where the laser power is distributed following a Normal distribution: in particular near to the exit window it seems to be bimodal while far it evolves into an ellipse, besides it is very divergent.
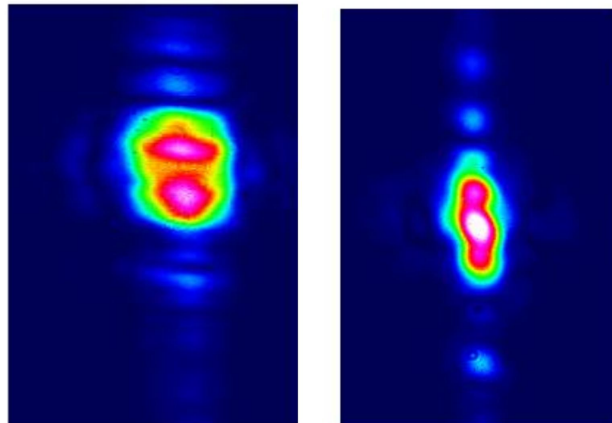
(a) About 20 cm far from the window (b) About 100 cm far from the window

Figure 3.4: Free running laser beam shape observed with the beam profiler at different distances.

To study the laser beam that I want to couple in fiber, I worked at maximum TA current (3200 mW), so I attenuated the power incident on the camera with a couple half-wave plate and a polarizing beamsplitter cube (discussed in the following section) and I applied some absorptive neutral density filters to protect the ccd camera and to avoid the saturation. Because of the divergence of the beam I focused it using a converging lens with focus f=200 mm positioned at 20 cm from the laser window and I studied the space evolution of the section mounting the beam profiler on a sliding carriage. The position z is measured from the lens position. I report the results in figure (3.5), defining the beam radius as the 2σ of a gaussian fit of the laser intensity and measuring the distance from the lens.
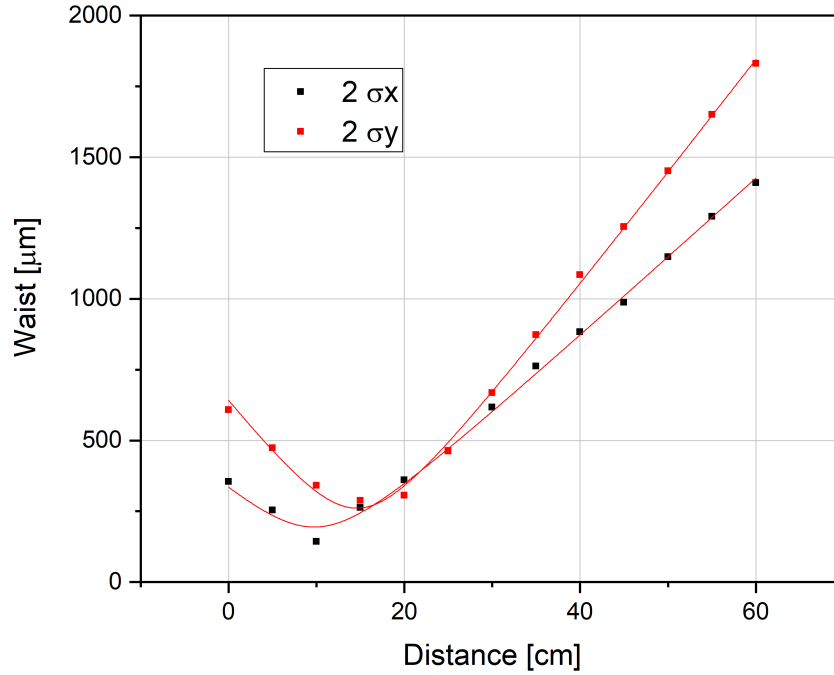
Figure 3.5: Space evolution of beam radius calculated starting from z=0 cm at the lens position.

I fitted the data with the equation that describes the space evolution of real gaussian beams [45]:

$$w(z) = w_0 \sqrt{1 + \left(\frac{(z - z_0)}{z'_R} \right)^2} \tag{3.1}$$

where the fit parameter z'_R allows to find the parameter $M^2 = z_R/z'_R$ that describes how much the real beam is similar to the ideal case considering the ratio between the theoretical Rayleigh range $z_R = \pi w_0^2/\lambda$ and the measured one. Despite the not ideal intensity distribution this model seems to adapt well with experimental data. I report in tab(3.1.1) the fit parameters of the two radii:

	$z_0(cm)$	$w_0(\mu m)$	$z'_R(cm)$	M^2
		Fit Parameters		
x	9,7(5)	194(14)	6,9(5)	2,25
y	14,6(3)	261(15)	6,5(4)	4,34

Table 3.1.1: Fit parameters of the laser beam space evolution with the collimating lens.

Using these fit parameters I could simulate the original beam before the lens extracting its parameters in tab.(3.1.2):

Estimated Parameters			
	$z_0(cm)$	$w_0(\mu m)$	$z'_R(cm)$
x	2,3(2)	446(12)	36,5(5)
y	-2,1(2)	798(17)	61,3(8)

Table 3.1.2: Simulated parameters of the space evolution of the laser beam emitted by the TA.

Comparing the waist position z_0 is clear that the laser beam is strongly astigmatic, while comparing the factor M^2 Is evident that in the y direction the beam is less ideal than in x. Moreover the divergence of the two space coordinates is different. In these conditions it is very difficult to obtain a good fiber coupling without manipulating the laser beam with optical elements.

3.1.2 Fiberdock VS Collimator

To couple the output of the amplifier in an optical fiber I tried both the fiberdock and an external collimator. I used a single mode single mode fiber (NA=0.12, MFD=5.1(5) μ m,λ_{cutoff} =7(manufactured by Schäfter+Kirchhoff. It presents an endcap that makes its application possible in presence of high laser power without breaking it.

The fiberdock is a good tools because it is pre-aligned and allows me to improve the fiber coupling in a simple way, acting only on three screw that move finely the collimation lens in the three space direction (x and y to center the beam on the fiber axis and z to focus it). At 3200 mA the maximum laser power after the fiber is equal to 770 mW, from which it is possible to estimate a coupling efficiency of about 50%.

Removing the fiberdock, I realized an external fiber coupling using a mirror to align the laser output from the amplifier in a optic fiber mounted on the collimator 60 FC-4-A11-07, manufactured by Schäfter+Kirchhoff and with focal distance f=11mm. This collimator presents a moving converging lens that allows to change the laser mode that can couple in fiber. I studied the evolution of the beam that exits from this collimator if I send to it a laser. Using the beam profiler and it is possible to observe a circular section with intensity well distributed following a gaussian distribution, as shown in fig.(3.6).

In fig.(3.7) is shown the waist space evolution of the beam that goes out from the collimator.

The output mode is very different from the laser beam coming from the TA, so I aligned the lens to obtain a collimated target waist similar to the average between x and y dimension of the free running beam near to the window. After that I realized the fiber coupling of the TA emission achieving a maximum efficiency about 50 %, similar to the fiberdock performances.

An important observation is that the profile of intensity distribution depends on the current provided to the amplifier and also on the vertical alignment of the injection laser beam: it has a great influence on coupling efficiency, that changes from less than 30% at 1300 mA to more than 50% at 3200 mA, both with the fiberdock and the external collimator.
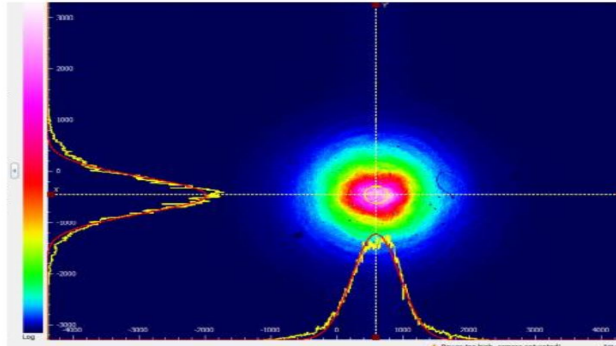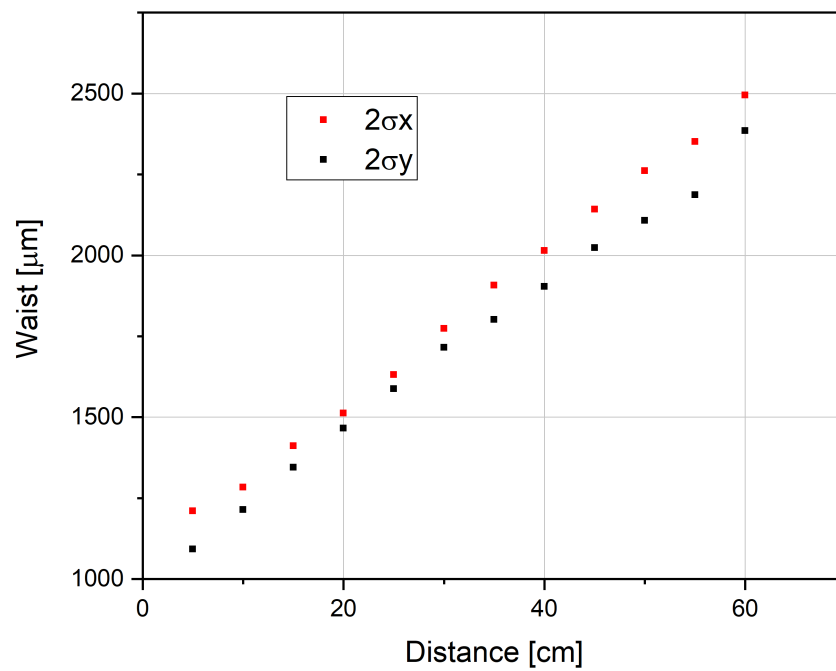
Figure 3.6: Output profile of collimator

Figure 3.7: Waist space evolution of the laser beam coming out from the collimator. The similar value for the x and y dimension represents the circular form of the section.
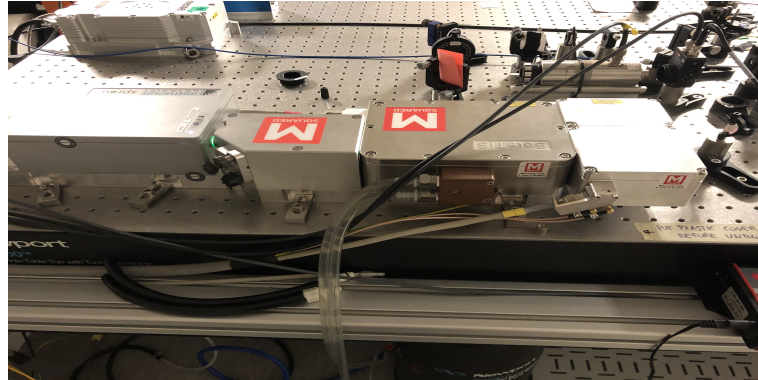
3.2   Titanium:Sapphire laser

Figure 3.8: Ti:Sa laser currently used in IT-Yb1

The laser currently dedicated to generating the optical lattice in IT-Yb1 is a Titanium: Sapphire laser provided by the company M squared, shown in fig(3.8). It is a tunable solid state laser optically pumped with a green laser at $532\,nm$. It is tuned to emit radiation at $759\,nm$ with a maximum power of $2\,W$. Despite its high emission power and narrow linewidth it is very sensitive to external perturbations, causing the oscillating mode to change. It is stabilized on a cavity with a frequency drift of $2\,kHz/h$ and its frequency is constantly monitored thanks to the beatnote with an optical frequency comb [46].

3.3   ASE spectra

In this section I will describe the studies performed on ASE spectra and their dependence by different conditions.

3.3.1   Optical bench

I realized the optical system shown in fig.(3.10) ans schematized in fig(3.9):
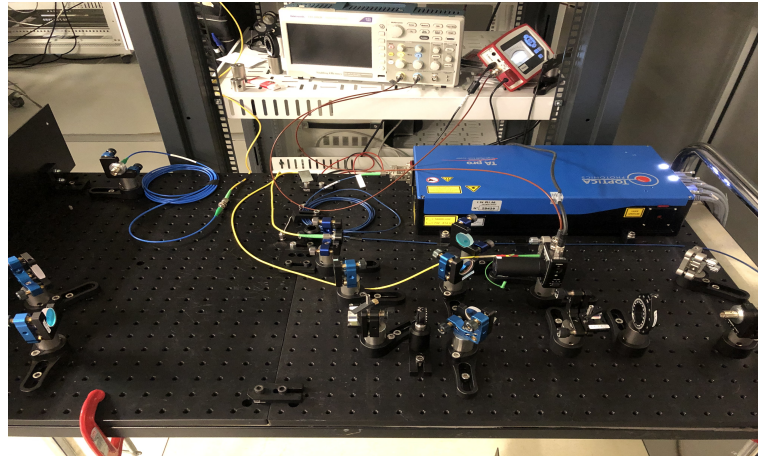
Figure 3.10: Photograph of the optical bench I realized to acquire the laser spectra.
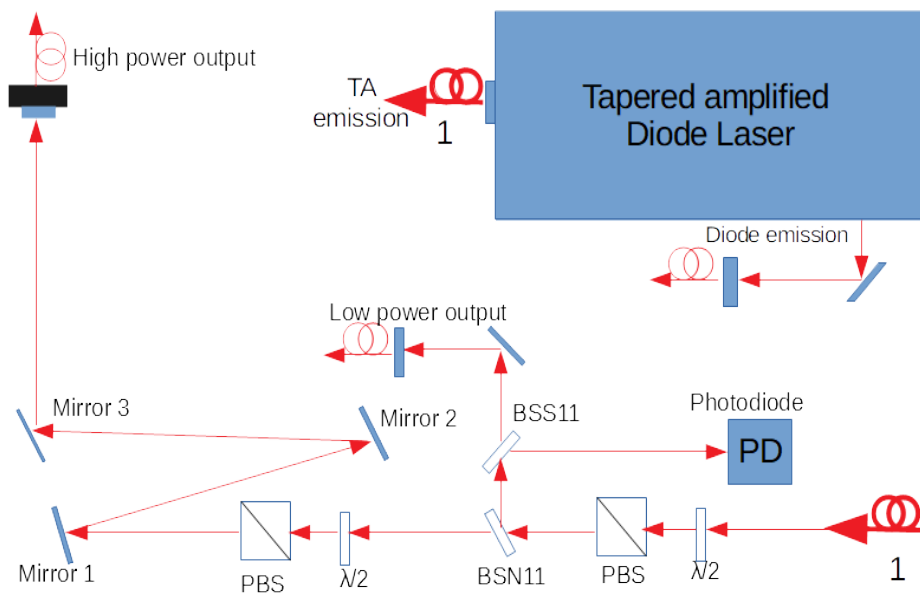

Figure 3.9: Optical system used to study laser emission and spectra

I coupled in fiber by a mirror and a collimator the diode radiation emitted from the side window. I achieved an efficiency of about 50 % limited by ellipticity and divergence of the laser beam. The radiation emitted by the TA (indicated by the index 1 in the previous scheme) is already coupled in the fiber using the fiberdock and I manipulated it with the following optical system, whose main elements present are:

- **Half-wave plate and polarizing beamsplitter cube (PBS102 provided by Thorlabs) couple** Used to make polarization cleaning of the radiation coming from the optical fiber, setting it horizontally. Orienting the plate allows me to rotate the laser polarization, while the cube transmits the p-polarization (lying on the incident plane) with efficiency 95 % and reflects the s-polarization (perpendicular to the incident plane).

- **Beam sampler** (BSN11 provided by Thorlabs). It splits the TA emission in two branches, the main with 95 % of power, the minor with the 5 %.

- **Beam splitter** (BSS11 provided by Thorlabs). It splits the minor branch in two, reflecting laterally the 20 % and transmitting the 80 % which is sent to a collimator using a mirror to realize a low power fiber coupling. It allows me to study the TA spectrum with the optical spectrum analyzer.

- **Photodiode** (PDA-100 A2 by Thorlabs). Connected to an oscilloscope, it allows to monitor the laser power without using a power meter that would block the beam propagation. I applied a convergent lens to focus the laser beam and a bandpass filter (PB 760-10) to reduce the external light noise.

- **Half wave and PBS couple** Here used as a power modulator.

- **High power fiber coupling** Realized with a system of three mirrors and a collimator with focal f=11 mm. I achieved a coupling efficiency superior than 80 % thanks to the possibility to move coarsely the collimator lens to match the Gaussian mode with the one coming from fiber input.

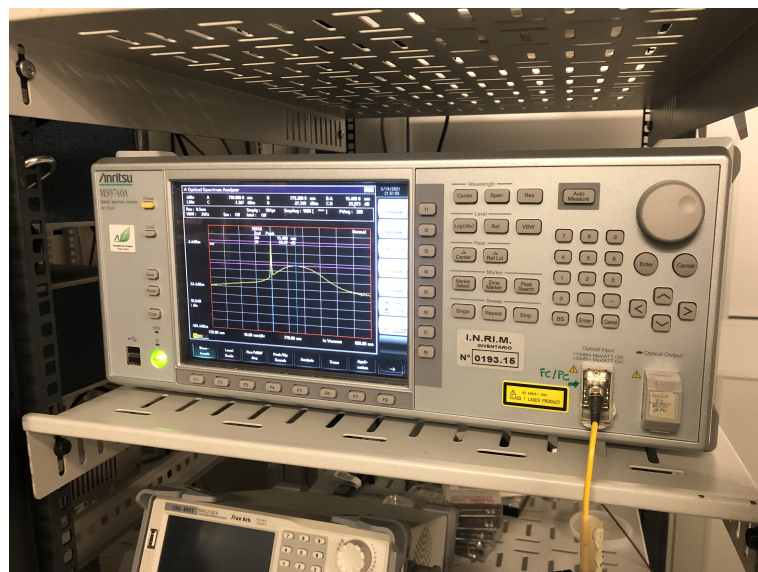**Optical Spectrum Analyzer**

Figure 3.11: ANRITSU MS9740A optical spectrum analyzer

MS9740A Optical Spectrum Analyzer (generally abbreviated to OSA) provided by Anritsu Corporation. It can acquire spectra measuring the power distribution of optical wavelengths. It is basically based on a diffraction grating that scatters on a CCD array the light coming from an optical fiber, analyzing it in a range between 600 and 1750 nm. It is a valid and reliable instrument with a wavelength accuracy of ± 20 pm and with resolution up to 0.03 nm. Operating in the measurement mode "High Dynamic Range" it can distinguish 42 dB at 0.2 nm from the peak wavelength and 70 dB at 1 nm.

For further information it is possible to examine the manual in references [47]. It is important to consider that the acquired data are saved in files measuring the spectral power in units of mW and the wavelength in nm. For the case of diffused spectra it is a critical point because the measured power depends on the resolution of the acquisition, so to obtain the spectral density it is necessary to divide the signal for the value of the set resolution.

3.3.2 Measured Spectra

Using the experimental set-up described in section(3.3.1) I coupled in fiber the laser power from the diode and from the TA and I sent them to the optical spectrum analyzer to acquire their emission spectra.
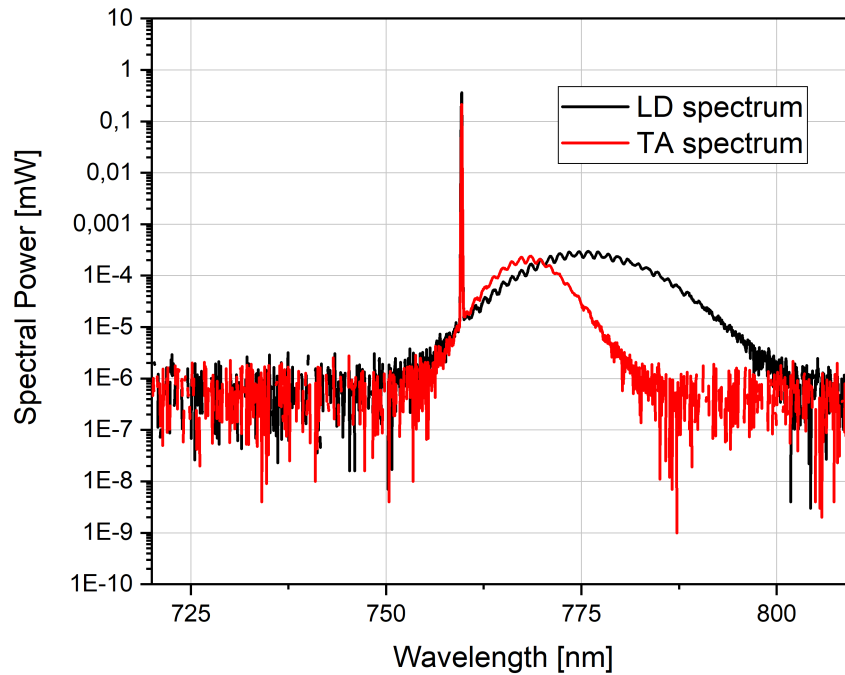

Figure 3.12: Comparison between Laser Diode (black) and Tapered Amplifier (red) spectra. Resolution 0.1 nm

Observing the graph.(3.12), it is possible to distinguish two different contributions both for laser diode and amplifier spectra: there is a very narrow and high intensity line, the carrier, well localized at about 759.35 nm. It represents the laser emission of the diode and also amplified by the TA, used to realize the optical lattice. At the same time there is a broadband and less intense spectrum. It derives from the phenomenon of amplified spontaneous emission and it is not negligible in optical devices based on semiconductors. This spectrum is continuous and strongly detuned from the magic wavelength so it can induce a systematic shift on the clock frequency. In this case it

is about 30 dB at 0.1 nm of resolution less intense than the carrier, but its effect can not be neglected if one wants to use the TA emission to realize an optical lattice with light shift of the order of 10^{-18}. It is evident that the ASE spectrum of the TA and the one emitted by the diode are different. From theory it is known that they are strongly dependent on the gain function of the semiconductor used to realize these devices [48] ASE spectra depend strongly on the OSA resolution because they are continuous, so increasing this quantity also increase the power that hits the portion of the CCD matrix considered. For the narrow line of the carrier it is not relevant.

I also acquired the Titanium:Sapphire spectrum to compare the current laser source with the candidate that I want to investigate. For this reason I coupled in fiber with a mirror and a collimator a small fraction of the power emitted by this instrument and, paying attention to not surpass the maximum input power of the OSA (10 mW without optical attenuation), I obtained the spectrum shown in fig.(3.13).
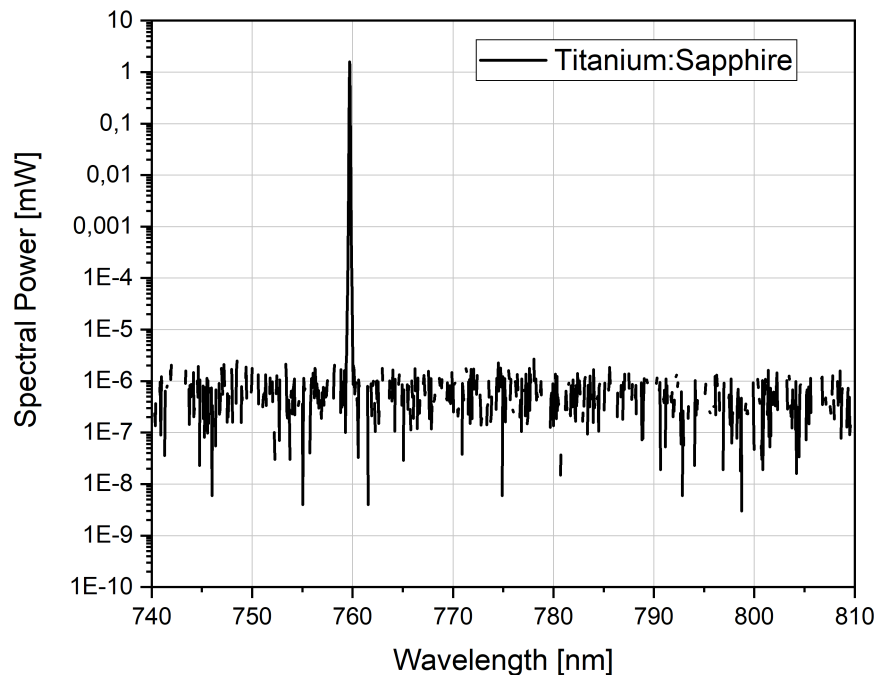

Figure 3.13: Spectrum of the Titanium:Sapphire laser. Resolution 0.1 nm

From this graph it is really evident the difference between the two laser sources: analyzing the spectrum in this case I can only find the narrow laser emission at 759 nm while the ASE, however present, is under the instrumental noise (below to -60 dBm) and more than 70 dB less intense than the carrier peak with a resolution of 0.1 nm. Currently ASE from Ti:Sa is not taken in account in lattice shift calculation because it is difficult to estimate and to measure its spectrum, but if I want to substitute it with a semiconductor laser I must know its behavior to study how to minimize the effects. At state of art there are some measures of the ASE emitted by this solid state laser,

as the one performed at SYRTE [49] where they blocked the resonance laser cavity to interrupt the laser amplification and to observe only the light emitted in a single pass: the limit of this technique is that it excludes the laser effect and the spectrum acquired represents only the fluorescence of the crystal, so it is not possible to know if it is the same when the laser is operating.

3.3.3 ASE polarization

To characterize the ASE emission I am interested in studying the degree of polarization of this incoherent radiation comparing it with the one of the laser emission. To do this I took advantage of the property of the Faraday insulators present in the DLC pro TA 759nm that transmits only one state of polarization and reflects the other to suppress it. These instruments are already aligned to maximize the transmission of the light emitted by the diode or by the amplifier in function, so I introduced a half-wave plate to rotate the input beam polarization. I minimized the transmitted power allowing the passage only to the perpendicular component (the one previously suppressed) and I acquired the spectrum with the OSA, distinguishing the ASE contribution from the laser power. As shown in figures (3.14a) and (3.14b), I acquired the spectra without the plate and with the plate oriented to minimize the transmitted power (so, in the hypothesis that laser emission that constitutes the main part of the power, it is perpendicularly rotated). Comparing the attenuation of the laser and the ASE peak between the two states I could estimate the degree of polarization of the two emissions.
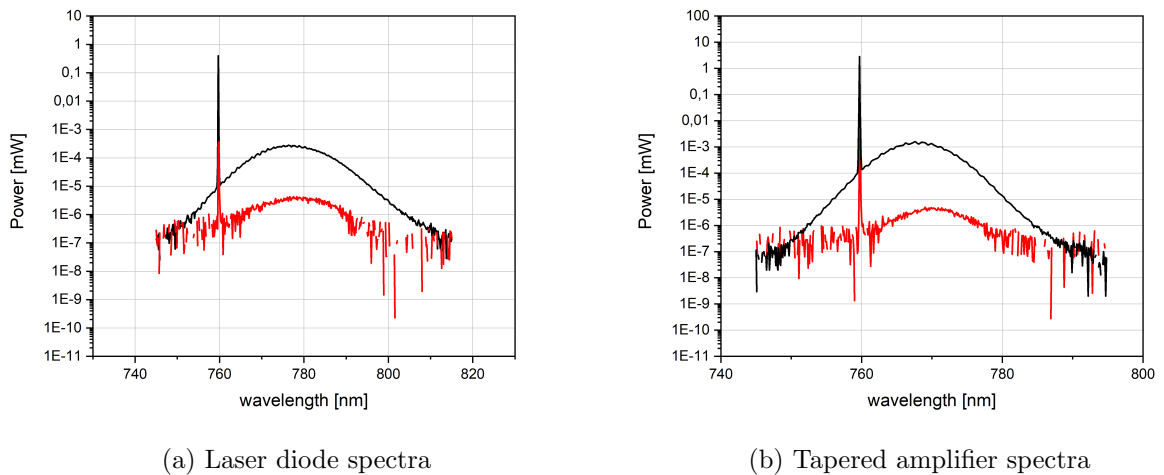

(a) Laser diode spectra   (b) Tapered amplifier spectra

Figure 3.14: Spectra acquired for different state of polarization.**Black** without plate.**Red** Minimizing the transmitted power rotating the plate.

In table (3.3.1) I report the results of attenuation calculated separately for the carrier and the ASE both for the diode and the amplifier.

	Carrier attenuation	ASE peak attenuation
Laser Diode	1078(15)	70(1)
Tapered Amplifier	1390(20)	317(4)

Table 3.3.1

As expected, that the carrier is strongly polarized with an imbalance of the order 10^3 between the two states for both the semiconductor devices. Considering instead the ASE the polarization imbalance is lower, of the order of 10^2, but it means that also this radiation is strongly linearly polarized on one axis, even if less that the laser radiation. In fact, considering a totally non polarized radiation, it should not be attenuated by a polarization analyzing elements because it oscillates indifferently on all the plane.

3.3.4 ASE fitting

Before estimating the light shift induced by ASE, it is necessary to study if the model introduced in section (2.2) is valid to describe the spectral distribution of the power generated by amplified spontaneous emission. I report in fig.(3.15) the spectrum of TA emission where I excluded the carrier to consider only the ASE contribution.
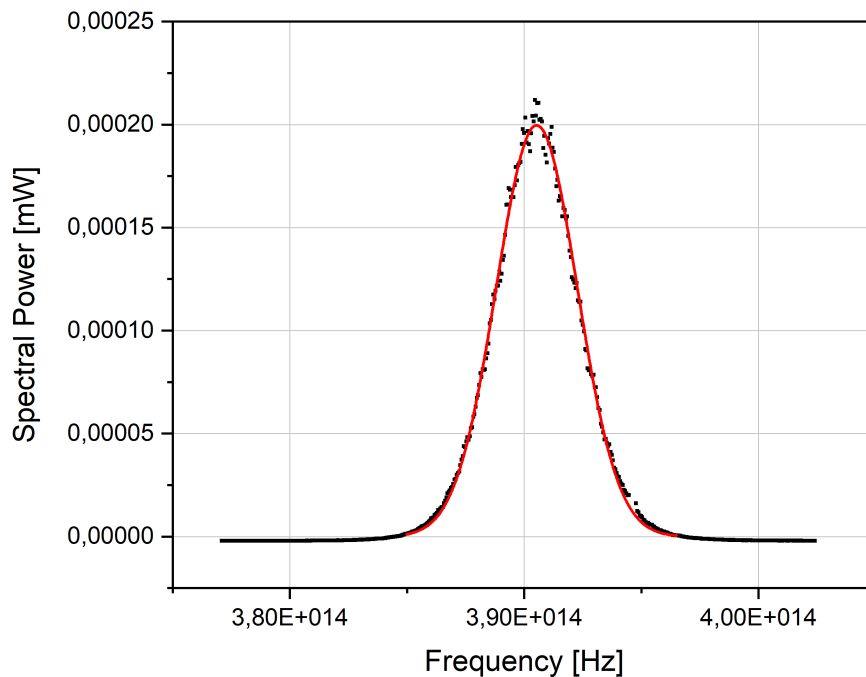

Figure 3.15: Spectral distribution of the ASE generated by TA with injection current 1300 mA.

Then I fitted the data using the expression (2.2) whose I report the fitting parameters in tab.(3.3.2).

$P_\nu(\nu) = A \cdot \nu \cdot \exp -\frac{(\nu-\nu_0)^2}{\Delta\nu_{ASE}}$	
A	$5.11(2)\,\mathrm{mW/Hz/nm}$
ν_0	$390\,527(9)\,\mathrm{GHz}$
$\Delta\nu_{ASE}$	$4070(20)\,\mathrm{GHz}$
R^2	0,99652

Table 3.3.2

From the value of the statistical estimator R^2 close to 1 the model reproduces the experimental data well enough, despite its simplicity. So I can use it to estimate the ASE spectral distribution in the following sections.

3.3.5 TA characterization

It is interesting to study the amplified spontaneous emission of the TA changing different working conditions, with the aim to know the behavior of this non desired radiation when one uses TA DLC pro 759 to generate the optical lattice. First of all I report in fig(3.16) the fluorescent spectrum of TA when it is pumped with the injection current but not injected by diode emission. This quantity is related to the gain of the amplifier, that for semiconductor optical amplifier in general is well approximated by a parabolic model [48]
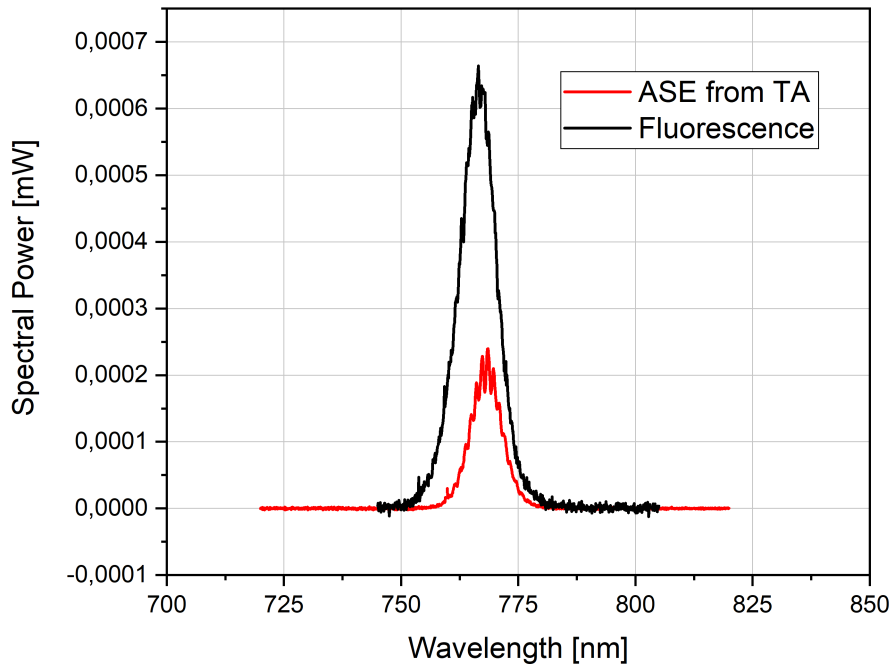

Figure 3.16: Spectrum of TA fluorescence without optical injection compared with the spectrum of ASE emitted by TA in operation. Resolution 0.1 nm

To obtain this spectrum I blocked the diode emission between the two alignment mirrors, observing with the optical spectrum analyzer the emission of the not injected TA. This probably represents a purely ASE spectrum without laser contribution: in fact, without the input from the diode, the light emitted by TA is only constituted by photons generated by spontaneous emission and others that are amplified by stimulated emission when they go through the active region.
Comparing the fluorescence with the ASE spectrum of the amplifier injected by the diode emission it is evident that the first is more intense: this effect is provided by the saturation of the active medium induced by the carrier

After that I studied the ASE spectrum changing the TA injection current. It influences the inversion of population in the active medium and so the amplifier gain at different wavelengths. These effects can change the spectral distribution of the emitted ASE, strongly related to the gain of the amplifier. I acquire the spectra of the TA emission at the high power optical fiber sending to the OSA the maximum input power of 10 mW, to maximize the signal to noise ratio. Obviously changing injection current has effects also on TA power as seen in graph (3.3), so to keep constant the power on OSA I compensated acting on the half-wave plate/cube beamsplitter couple located close to the collimator of the output fiber. To compare the data in the same conditions I show in fig.(3.17) the spectra normalized with respect to the peak of the carrier.
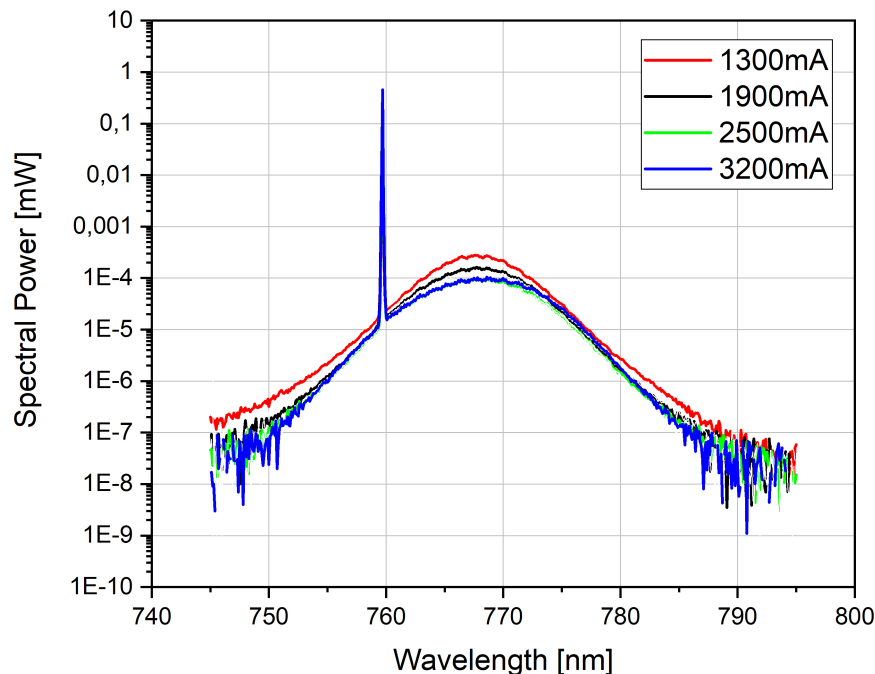

Figure 3.17: TA spectra for different injection current normalized on the peak of the carrier. Resolution 0.1 nm.

It seems that increasing the injection current the ASE power becomes less relevant

in intensity with respect to the carrier, fixed for all the spectra.

To analyze this phenomenon in detail I studied the ratio between the power of the carrier and the power of the ASE, reporting the results in the graph (3.18).
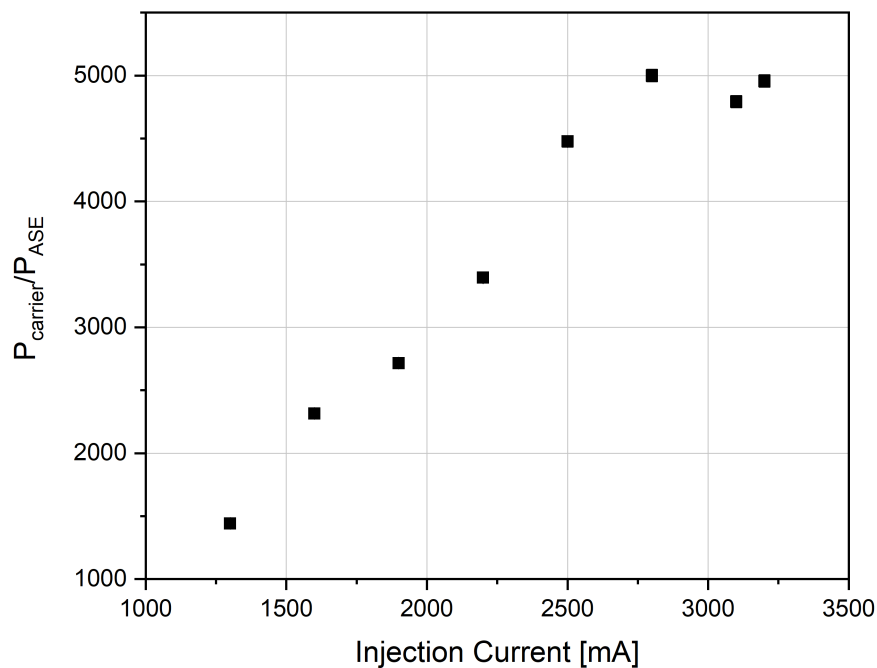

Figure 3.18: Ratio between carrier power and ASE peak power measured with resolution 0.1 nm.

These data confirm what was already evident from the graph:(3.17): keeping fixed the carrier power, the ASE peak decreases in power as the injection current increases, increasing the value of the ratio reported in the graph I observe that close to the maximum current the ratio seems to be constant, suggesting the presence of a saturation. Moreover, after fitting the ASE spectra emitted by TA with the expression (2.2), I calculated the ASE linewidth as FWHM of the spectral distribution. I report the results in the graph in figure(3.19).
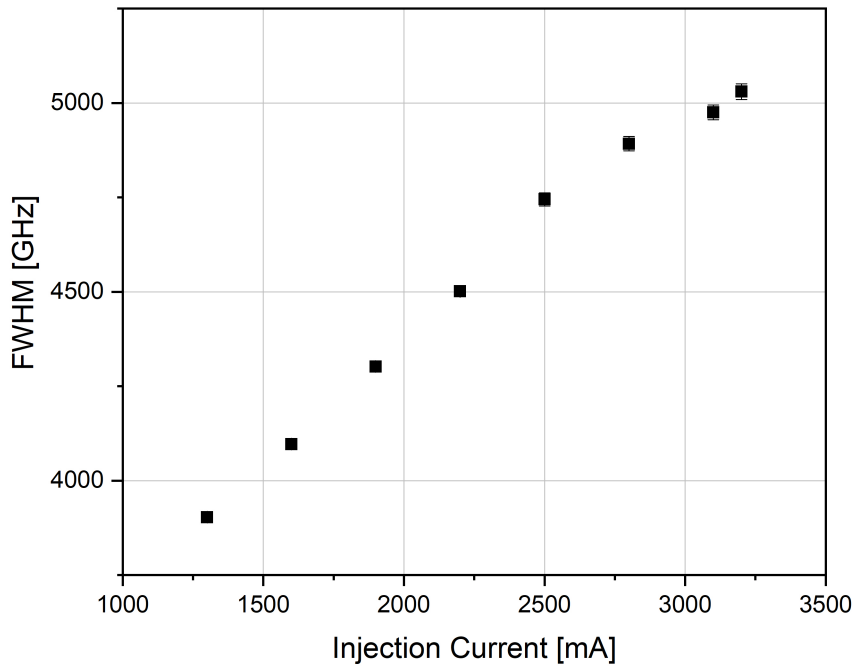
Figure 3.19: FWHM of the ASE spectra changing the TA injection current

From this figure it is possible to see that increasing the current also the ASE linewidth seems to increase. These results may be counterintuitive with respect to what seen in fig.(3.17), where the spectra acquired at lower current seem to be more broadband then the ones at higher current. Probably it is a problem carried by the logarithmic scale that deceives the observer.

To conclude this discussion as the injection current increases the ASE spectrum becomes less relevant than the carrier emission although it increases in absolute power. At the same time it becomes more broadband exerting its effects on a wider range of wavelengths. I can try to explain this phenomenon relating it to the change of the amplifier gain with the injection current: higher current pumps more electrons in the conduction band of this semiconductor device, causing a higher inversion of population in the active region that can be used by the injected laser power emitted by the diode to amplify itself. This higher amplification has as consequence a smaller inversion of population available to photons deriving from TA spontaneous emission, causing a lower ASE power.

A further characterization of the ASE spectrum emitted by the TA can be done as a function of the laser frequency emitted by the diode changes. For these measure I kept fixed the injection current at 3200 mA and I tilted the grating in extended cavity (like discussed in sec:(3.1)) to tune the laser diode emission at the desired wavelength. I measured the laser wavelength with a wavelength meter to which I send the diode power with an optical fiber while I acquire the TA spectra with the OSA. In figure(3.20) I show the different spectra with the carrier detuned from the magic wavelength (759
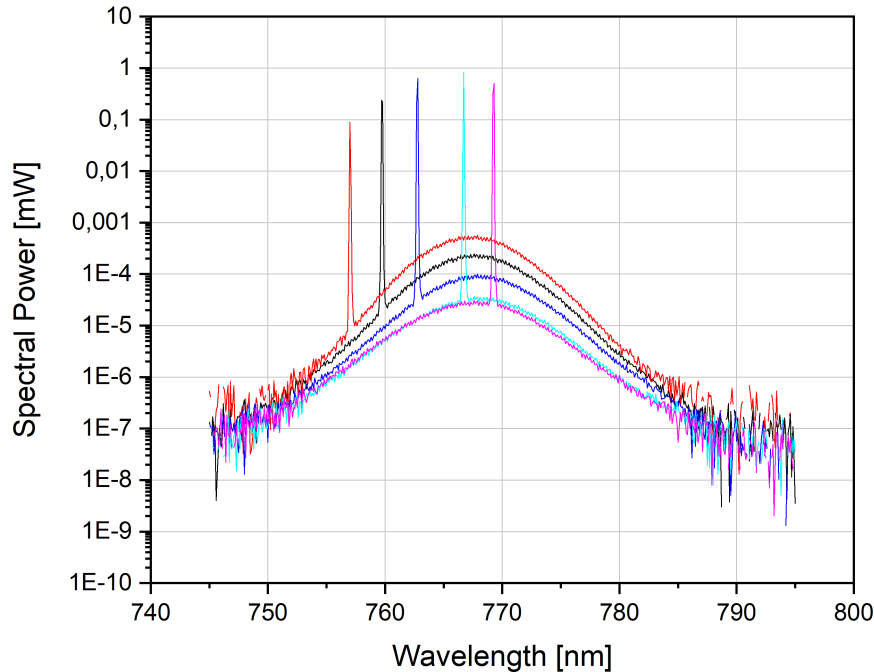
nm).

Figure 3.20: Spectra acquired for different diode wavelength, detuned from magic wavelength (black line).

I observed that the ASE spectral distribution varies mainly in intensity more than in shape as the laser wavelength changes. The ASE spectral power changes with respect to the case where laser emission is tuned on magic wavelength (the black spectrum in fig(3.20), in this graph up to a factor 20. Tuning the diode to a wavelength close to the maximum of the TA gain (about 768 nm) not only the amplified laser emission increases but the ASE spectrum becomes less intense and more symmetrical with respect to the laser wavelength. If I resume the previous argument to explain the magnitude of ASE emission, I can explain this phenomenon in terms of gain and inversion of population of the TA: close to the maximum the laser is more amplified and it is able to absorb most the inversion of population, so the amplification by stimulated emission of spontaneous emission photons is reduced, attenuating the ASE spectrum. This is an interesting observation because if the ASE spectrum used to realize the optical lattice would be more symmetrical also the contribution to light shift provided by the red and blue detuned part of the spectrum would be more similar, reducing the ASE induced lattice shift up to some Hz [27]. Something similar happens considering the case of optical lattice for strontium atomic clock, where the optical lattice is realized at magic wavelength λ=813.4 nm and the tapered amplifiers used for this purpose have the maximum of gain about at this wavelength, generating a quite symmetrical ASE spectrum as discussed in reference [49]. Another important consequence is the fact

that the ASE intensity varies with the laser wavelength and it will be useful in the following sections: considering the ASE power at 759 nm it increases when the laser wavelength is higher than the magic wavelength and decreases when the it becomes lower. As described previously, this phenomenon happens because the carrier is farer or closer to the maximum of gain, producing higher or lower amplification to the ASE.

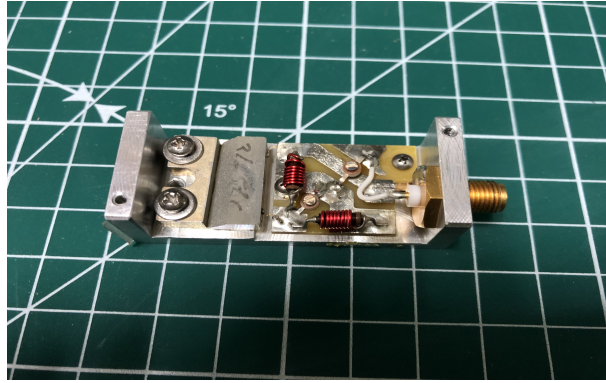## 3.4   Acousto Optic Modulator - effect and use

Figure 3.21: AOM used in my thesis without cover

As described in section (1.5.1) the process to measure experimentally the magic wavelength is based on alternating Rabi spectroscopy of the clock transition at high and low lattice power: at magic frequency the difference of dynamic polarizability between the two clock states is null and so the measure is not sensitive to light shift [25]. The instruments mainly used to change the lattice power are the acousto optic modulators (AOM) because of their efficiency and their execution speed. As shown in figure (3.21) it is composed basically by a crystal, through which the laser beam moves, and a piezo-electric transducer applied on its surface. When it is powered by an oscillating voltage the piezoelectric element oscillates inducing the generation of sound waves in the crystal transversely to the direction of laser propagation. As schematized in fig.(3.22) in this case the AOM behaves like a diffraction grating with reticular step Λ equal to the wavelength of the sound waves, following the Bragg law:

$$2\Lambda \sin\theta = m\frac{\lambda}{n}$$

(3.2)

where θ is the angle of incidence of the laser beam with respect to the normal to the crystal surface, m is the diffraction order and n is the refraction index of the crystal. A function generator can produce the oscillating voltage at frequency of 100 MHz, in the range of radiofrequencies. I define the power of this voltage as P_{RF} and I can control it by changing the amplitude of the sine wave. Before feeding the acousto optic
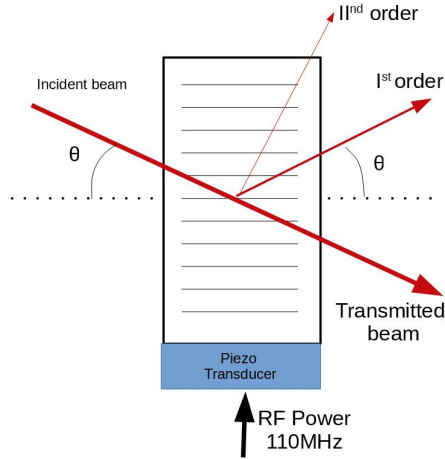
Figure 3.22: Operating scheme of an acousto optic modulator. The incident beam goes through a diffraction grating generated by the acoustic wave separating the laser power in different diffraction orders

modulator with a coaxial RF connector SMA (SubMiniature version A), it is sent to an amplifier to be amplified up to 30 dB. I define the quantity P_{AOM} as the laser power measured after the acousto optic modulator. Basically, providing a oscillating voltage to the transducer the diffraction grating transfers a fraction of P_{AOM} from the 0th order (transmitted beam) to other superior diffracted orders deflected at angle θ in function f the laser wavelength. The value of P_{RF} provided determine how much laser power is transferred on higher orders.

In this case I want to use the AOM only as a laser power modulator driven by P_{RF}, but it finds applications also as frequency modulator, because photons of higher order sum frequency to the one of the sine wave. It is also possible to image this as a photons-phonon scattering where the light particle emitted sums its energy with the one of reticular quantum (or is reduced of the same quantity if I consider the negative diffraction order).

I placed the AOM between the mirror 2 and 3 of the figure(3.9 and I aligned the system on the first diffracted order tuning the angle to maximize the out beam power: when the radiofrequence power is off all the light goes on the 0th order while when it is on I move laser power toward the output fiber. It is possible to calculate the diffraction efficiency of the acousto optic modulator by the ratio between the P_{AOM} on 1st order and at 0th at AOM turned off:

$$D.E. = \frac{P(I^{st}, on)}{P(0^{th}, off)} = 68\% \tag{3.3}$$

Varying the P_{RF} provided to this device it is possible to characterize the attenuation

properties of the AOM. In fig.(3.23a) is shown the ratio between the output power at a certain radiofrequency power and the one at the maximum of transmission (observed at P_{RF}=0.6 dBm) referred to the first diffracted order. Regarding instead the 0th order in fig.(3.23b) is shown the ratio between the power transmitted on this order changing the radiofrequency power and the transmitted laser power at AOM turned off.
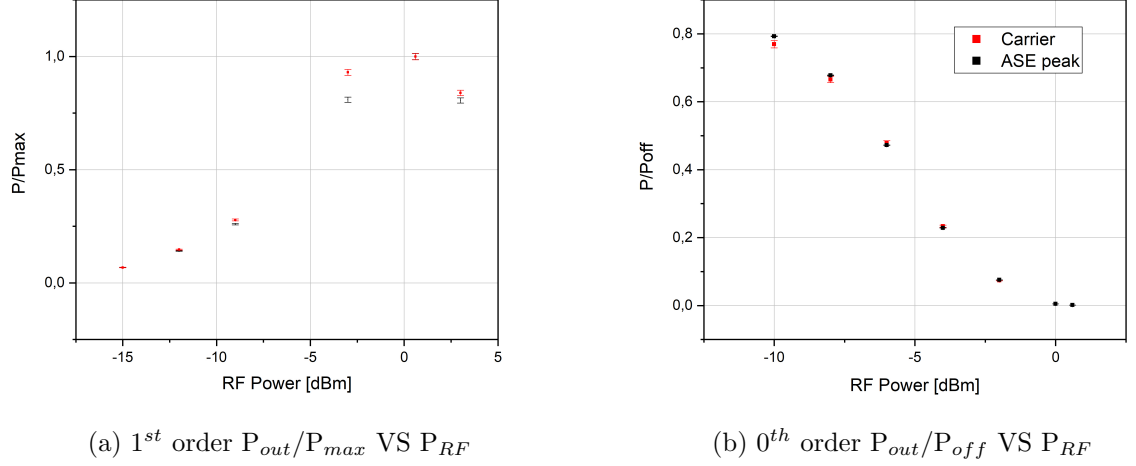

(a) 1st order P_{out}/P_{max} VS P_{RF}

(b) 0th order P_{out}/P_{off} VS P_{RF}

Figure 3.23: AOM transmission at 1st and 0th order of diffraction changing P_{RF}.

From these measures I observe that the power transmitted on the first diffracted order increases with the P_{RF} provided up to maximum at 0.6 dBm, so for my purposes I would set the working point at the maximum and I could reduce the RF power to reduce the laser intensity that generate the optical lattice, reducing the trap depth on atoms. Regarding instead the not diffracted beam, the 0th order emitted by the AOM, it has a maximum of transmission at low RF power while it decreases close to 0.6 dBm, where prevails the diffracted beam.

These measures are acquired with the optical spectrum analyzer, allowing to distinguish the laser by the ASE attenuation: in fact I can not know in advance if also non-coherent light behaves like laser in presence of a diffraction grating.

From graph (3.23a) and (3.23b) I observe that the ASE power transmitted is not compatible within the uncertainty with the data referred to the carrier power, suggesting that ASE attenuation is different from laser attenuation. To investigate further this phenomenon I acquired with the OSA different spectra of the 1st diffracted order and of the 0th order changing the diffraction efficiency acting on the RF power but at the same optical power compensating with the plate-cube couple to keep it constant. In fig.(3.24) are represented the TA spectra acquired for the 1st diffracted order in the conditions here described, to observe if ASE spectral distribution change varying P_{RF} but keeping the total power constant.

Looking at the ASE spectra it is evident that they are not constant but they are influenced by the AOM in function of P_{RF}. It makes it difficult to estimate the ASE light shift if one wants to performe measure changing the lattice intensity, because for every condition the ASE spectral distribution is different. Moreover repeating the
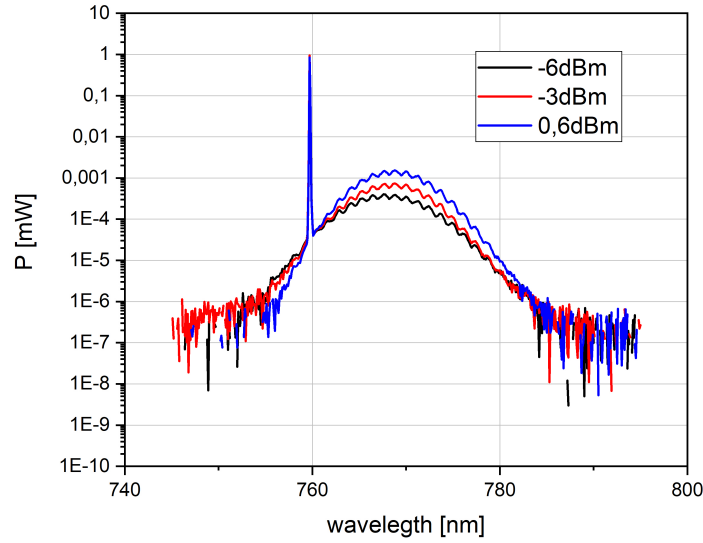
Figure 3.24: Variation of ASE spectra changing the RF power provided to AOM but keeping constant the optical power to 10 dBm.

acquisition in the same conditions this results are slightly reproducible. Probably it is caused by thermal effects on the crystal that change the diffractive efficiency of the instrument varying P_{RF}, beyond the poor coherence of the ASE that make its interaction with the diffraction lattice not predictable.

3.5 Filtering

The technique chosen to mitigate the light shift induced by the incoherent ASE background is to filter the radiation emitted by the amplifier. This allows to improve the TA spectral purity suppressing ASE and transmitting only the carrier toward the atoms. In this section I present the experimental set-up that I realized to use two different filters in different conditions and their characterization, studying their efficiency, their bandwidth and their attenuation for far detuned frequencies.

3.5.1 Toptica filter

Figure 3.25: Diffraction grating provided by Toptica

The first kind of filter studied is a reflecting diffraction grating provided by Toptica, the same company that produced the laser DLC pro TA 759. It is shown in fig.(3.25). It was part of the monochromatic detector DFC-MD manufactured by Toptica [50] and used to realize beat detection on the optical frequency comb. After removing the diffraction grating from the instrument I mounted it on an adjustable support as shown in the previous figure, in order to use it in the optical bench. Not having available much prior knowledge about this filter except the manufacturer declaration about the original system, which achieves a bandwidth of $10\,\mathrm{GHz}$ with a resolution $<1\,\mathrm{GHz}$. I studied its behavior coarsely to know how it works and to distinguish its characteristics. Lighting up the filter with a white light source it decomposes the white spectrum at different angles (see fig.(3.26a). I aligned the grating in my optical system minimizing the 0th order, i.e. the reflected beam, and maximizing the 1st diffracted order tilted of about 30° from the incident beam. The diffraction pattern of the TA emission has been projected on a black screen like shown in fig.(3.26b); it is possible to distinguish an intense circular spot on the right of the figure while at left there is a less intense diffused figure. The first represents the carrier, while the second refers to the asymmetrical ASE spectrum diffracted at different angles in function of the wavelength. Changing the laser frequency coarsely the circular beam moves because it is diffracted at different angles and at the same time also diffracted ASE changes its intensity as already discussed. These are considerables as evidence that it is really the diffracted beam and so that the filter is behaving as a typical Bragg grating that separates the radiation at different angles in function of its wavelength.
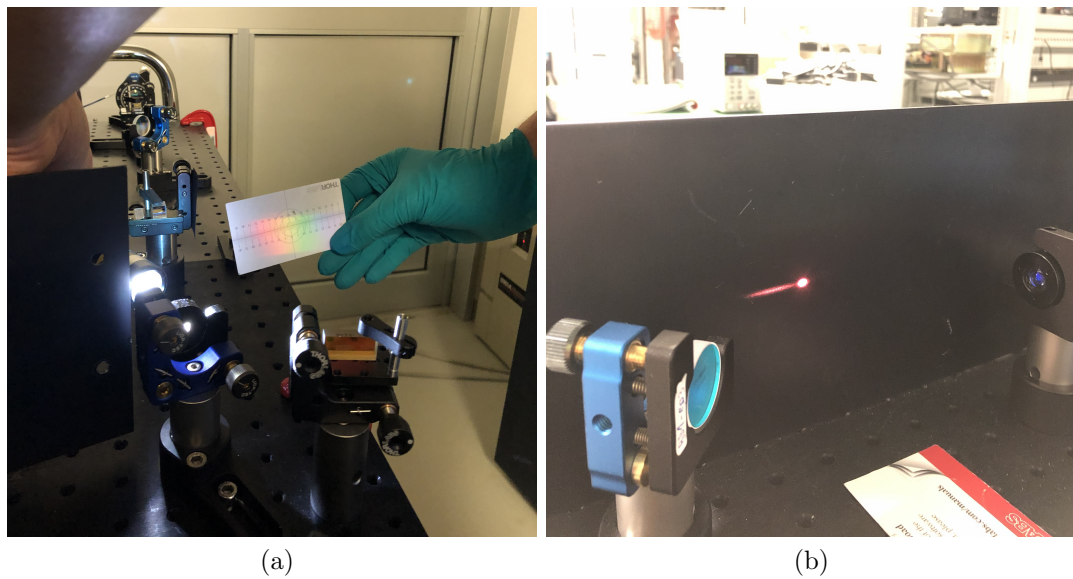
Figure 3.26: (a)White light scattered by the diffraction grating. (b)TA emission scattered by the grating. It is possible to distinguish the monochromatic carrier scattered at the same angle, by the ASE spectrum diffused in function of the wavelength.

For reflecting diffraction grating it is valid the Bragg law:

$$2d \sin \theta = m\lambda$$

(3.4)

where d is the distance between two successive fringes and θ is the angle of incidence of the laser beam on the grating.

The grating has been placed on the optical bench removing the mirror 1 in the scheme in fig.(3.3.1) to filter the radiation emitted by the TA. Fixing the laser frequency at $394\,798\,\text{GHz}$, the grating is aligned tilting the angle with the incident beam to maximize the diffracted power at 1st order and this laser beam was sent to the collimator of the high power fiber coupling.

After that it is possible to characterize the filter transfer function (T) near to the maximum, to study its bandwidth and its maximum efficiency. The input power has been measured placing a power meter before the grating while after the fiber to measure the diffracted power: doing this it is possible to carry out a more accurate measurement reducing the fraction of the solid angle that is under analysis, excluding the ASE scattered near the carrier. To characterize only the filter and not the system composed by filter and fiber (that can attenuate part of the ASE) it is necessary to take in account the coupling efficiency, equal to $79\,\%$, normalizing the measured output power. Providing a voltage to the piezo present in the extended cavity it is possible to sweep a range of $400\,\text{GHz}$ centered on magic frequency and repeating then the measurements of power to calculate the filter transfer function at different frequencies.

The results are shown in figure (3.29). The maximum diffraction efficiency estimated at the peak is equal to $92.4(3)\,\%$ with a FWHM$= 84.51(2)\,$GHz.

Rotating the incident beam polarization with a half wave plate placed before the filter it is possible to study the polarization sensivity of the Bragg grating under test. Using a PBS cube it is possible to know when it is perpedicularly rotated, and testing the filter for an incident vertical polarization this instrument it was observed that it can not operate. In fact it moves all the laser power from the diffracted to the reflected beam, emptying the power of the 1st order previously aligned. The fact that it is extremely polarization dependent is another proof that it is a typical Bragg grating.

There are two solutions to improve the filter performances: first increasing the optical path of the diffracted laser beam before to be coupled in fiber (in order to reduce the portion of the solid angle that hits the collimator and so the range of frequencies that are transmitted), then using the grating in double pass, to improve its diffractive power. With this aim I realized the optical system shown in fig.(3.28) and schematized in fig.(3.27.
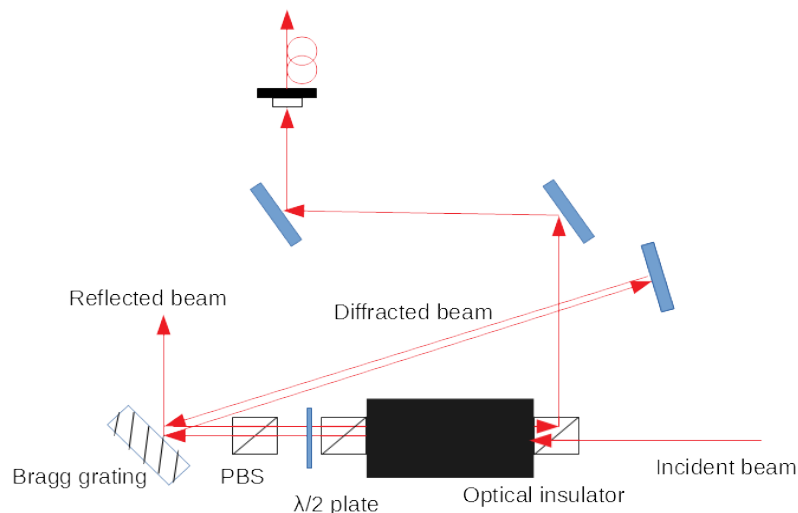

Figure 3.27: Optical system realized of the Toptica Bragg grating in double pass configuration

The laser beam emitted by the amplifier passes through an optical insulator: at the entrance it presents a polarizing beam splitter cube (PBS) that transmits the horizontal polarization and reflects the vertical one. Then it encounters a magnetic field generated by a permanent magnet that rotates the light polarization of 45° for Faraday effect. At the exit there is another PBS tilted of about 45° to transmit the rotated polarization. Out of the insulator, the laser beam encounters a couple composed by a half wave plate and cube beamsplitter to rotate the laser polarization bringing it back to the starting horizontal state before to go to the Bragg grating. The diffracted laser beam is reflected again to the grating using a mirror and then it walks the optical path in reverse way: encountering the half wave plate its polarization is again tilted to 45° from
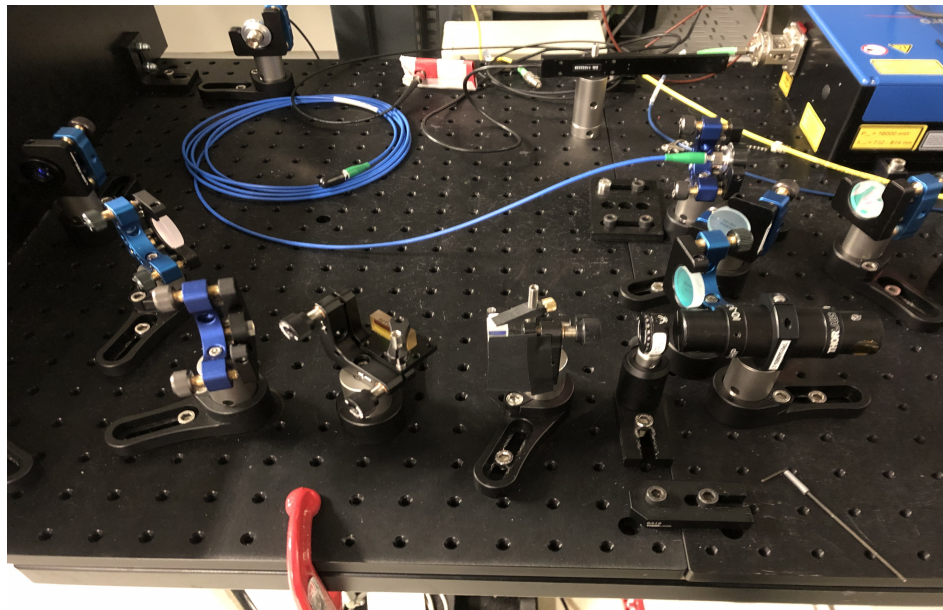
Figure 3.28: Photograph of the optical bench I realized to filter the TA emission with the Toptica Bragg grating in double pass.

the horizontal state to be transmitted by the second cube, but when it pass through the insulator it is again tilted of 45° encountering the first cube with a vertical polarization. The laser is so reflected by this beamsplitter allowing to extract the diffracted beam, sending it to the collimator to couple it in fiber and study its spectrum and the filter properties.

It is possible to tilt manually the two cube at the entrance and at the exit of the insulator after loosening two screws: typically one must do this process first to maximize the transmission of the forward beam, then to maximize the isolation capacity from retro diffused beam. These processes have been performed to align the insulator, but it would be necessary to take in account also the internal losses on the insulator.

With this experimental set-up it is possible to characterize the grating in double pass configuration near the maximum of diffraction. The estimated maximum efficiency is equal 74.9(3) % with a FWHM=66.874(3) GHz. I report the shape of the transfer function in fig.(3.29), comparing it with the single pass result.

Figure 3.30: Volume Bragg Grating BPF-759
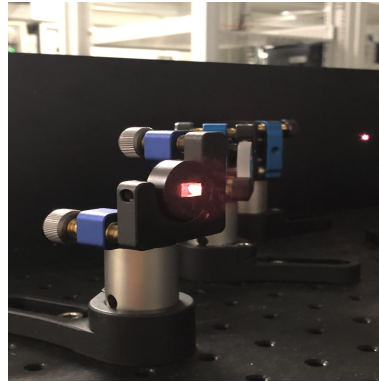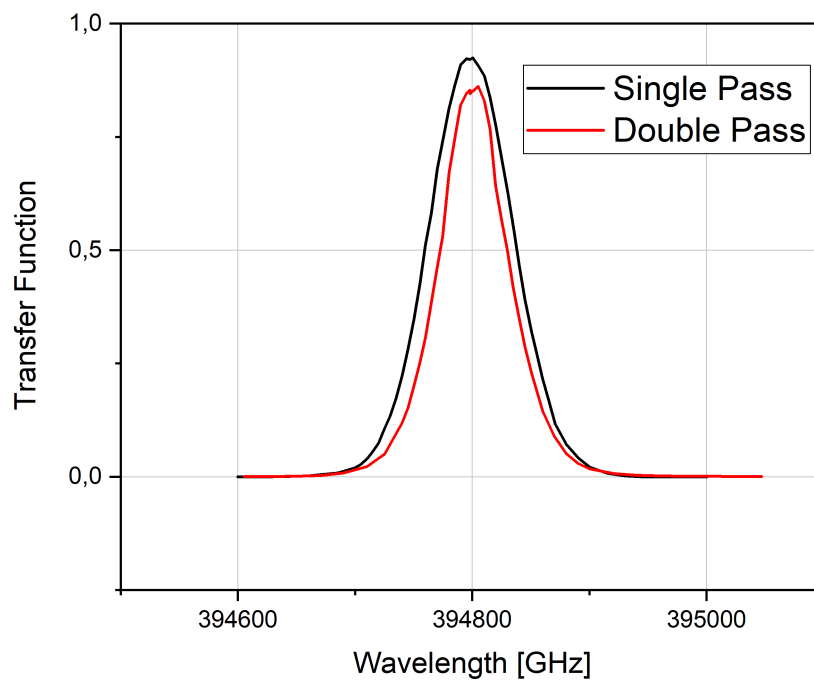

Figure 3.29: Comparison between the transfer function of the Toptica Bragg grating used in single and double pass

As expected, paying a small reduction in efficiency in double pass configuration the filter bandwidth becomes narrower. Anyway this result is inferior to what expected and very far from the 10 GHz declared by the manufacturer for the original monochromatic filter.
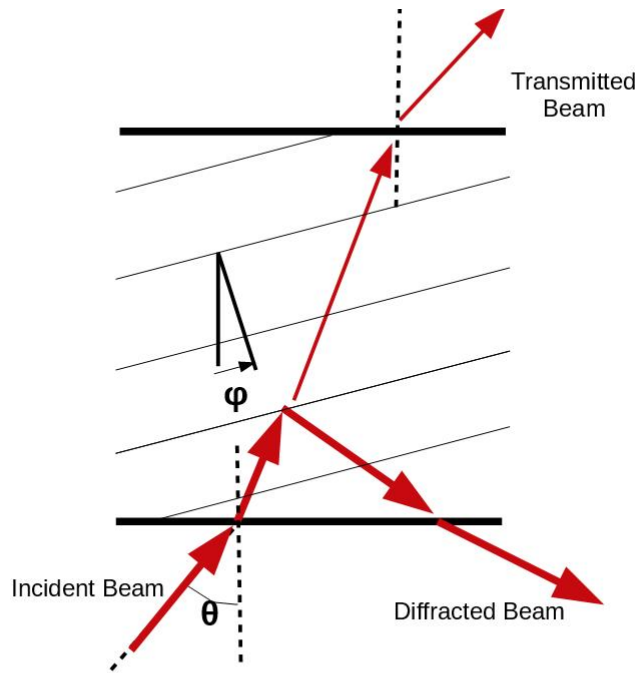
Figure 3.31: Operation scheme of a reflecting volume Bragg grating

3.5.2 BPF-759 by Optigrate

The second filter that was characterized is a reflecting volume Bragg grating BPF-759 shown in fig.(3.30) provided by Optigrate. This choice is originated by the fact that similar tools are already used by other groups [51] or for example in IT-Yb1 to filter the Titanium:Sapphire radiation [22]. As schematized in fig.(3.31), a volume Bragg grating is fundamentally composed by a series of thin layers with periodical change of refractive index, tilted at an angle ϕ from the surface. Modifying the orientation of the grating it is possible to use it in reflection or in transmission mode [52]. Despite there are more complex and accurate theories to describe the diffraction effect of a volume Bragg grating [53], it is possible to describe it with the following simplified equation [54]:

$$2\Lambda \cos\left(\theta + \phi\right) = m\lambda \tag{3.5}$$

where Λ is the reticular step of the grating (here constituted by the distance between two successive layer with the same refraction index), ϕ is the angle between the layer and the surface of the grating, m is the diffracted order and λ is the laser wavelength diffracted at angle θ. Here the trigonometric function used is a cosine because the case taken into account is a reflection grating. Tilting the grating it is possible select the laser wavelength for which the diffraction efficiency is maximum, tuning the filter transfer function.

I placed the Volume Bragg grating instead of the mirror 1 and before the AOM, as shown in fig.(3.32). Then I tuned the filter acting on the angle to have the maximum

diffraction efficiency at 394 798 GHz and I sent the reflected beam toward the AOM and then toward the collimator of the high power fiber coupling. Moreover I realized a fiber coupling with a mirror and a collimator to collect the laser beam transmitted by the grating, i.e. the not filtered laser power.
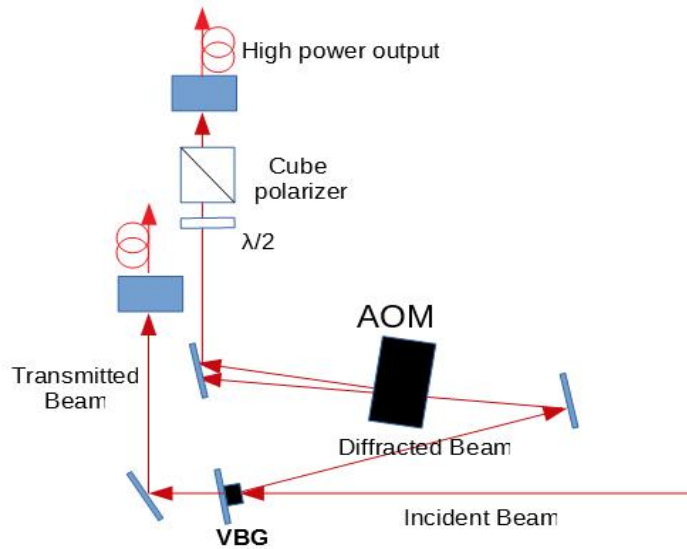
Figure 3.32: Optical bench with AOM and volume Bragg grating in single pass configuration

The first characterization performed is the study of the grating transfer function to know its performances near to the maximum of efficiency. For this purpose it is necessary to calculate the ratio between the power of the diffracted beam and the input power on the grating, measured with a power meter. It is possible to change the laser frequency providing a voltage to the piezo that tunes finely the diode frequency, iterating the previous calculation. The results are shown in the black points in figure (3.36).

The diffraction efficiency at the maximum equal to 89,20(6)% and it is possible to estimate a FWHM=29.965(9) GHz, that means a range of wavelength of about 0.056 nm in the bandpass of the filter.

It is interesting to acquire the filtered spectrum with the OSA and comparing it with the one of the transmitted beam, i.e. the not-diffracted beam. The results are shown in fig(3.33).

Figure 3.33: **Black** Diffracted spectrum; **Red**Transmitted spectrum. Resolution 0.1 nm.

I observe that the diffracted beam (black line), constituted by the laser emission that passes through the filter, is now narrower than the TA emission and quite comparable with the titanium: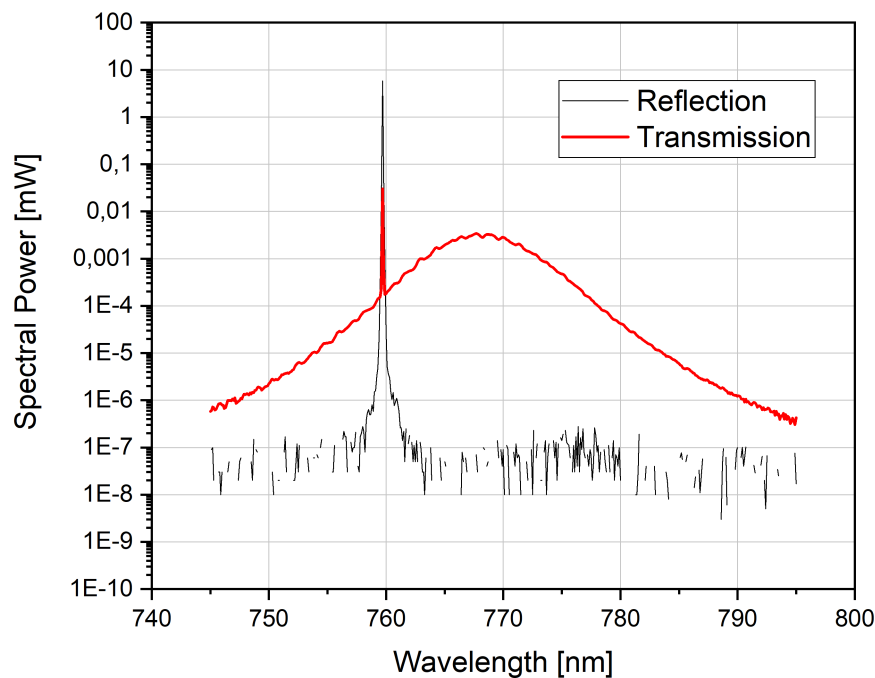Sapphire spectrum. It would be interesting to have a direct comparison between the two spectra, but unfortunately the resolution of the optical spectrum analyzer makes it not possible to realize this measure with high accuracy. Regarding the transmitted spectrum (red line), so the filter losses, it is possible to observe that the ASE detuned from the bandpass is not significantly reduced while the carrier is strongly attenuated by the filter of about 20 dB. Known this property of the volume Bragg grating it is possible to study if it can be employed to observe the ASE spectrum of the Ti:Sa laser: as already mentioned, this laser source is the most used worldwide to generate the optical lattice in atomic clocks (except for some transportable atomic clocks), so it would be useful to know its ASE spectral distribution to estimate an eventual induced light shift to take in account in the uncertainty budget. The idea is to study the beam transmitted by the volume Bragg grating applied on Titanium:Sapphire emission, where if the carrier is strongly attenuated while the ASE is quite unperturbed it could be possible to observe the latter spectrum, now less irrelevant with respect to the laser emission. To perform this measurement I coupled in fiber the beam transmitted by the grating applying a mirror and a collimator behind the filter and I sent it to the OSA. I maximized the transmitted power up to the limit of the optical spectrum analyzer of 10 mW, with the idea that if only the carrier is attenuated it is possible to amplify the ASE spectrum of the same factor keeping the

total power constant. From the spectrum reported in fig.(3.34) there are no evident differences with the unfiltered shown in fig.(3.13). With this technique I can quantify the ASE power respect to the carrier: if previously it was estimated as more than 70 dB at 0.1 nm of resolution less intense than laser emission (instrumental limit), considering that also attenuating the carrier of 20 dB this spectrum is not visible it is possible to assert that it is more than 90 dB under the carrier at this resolution.
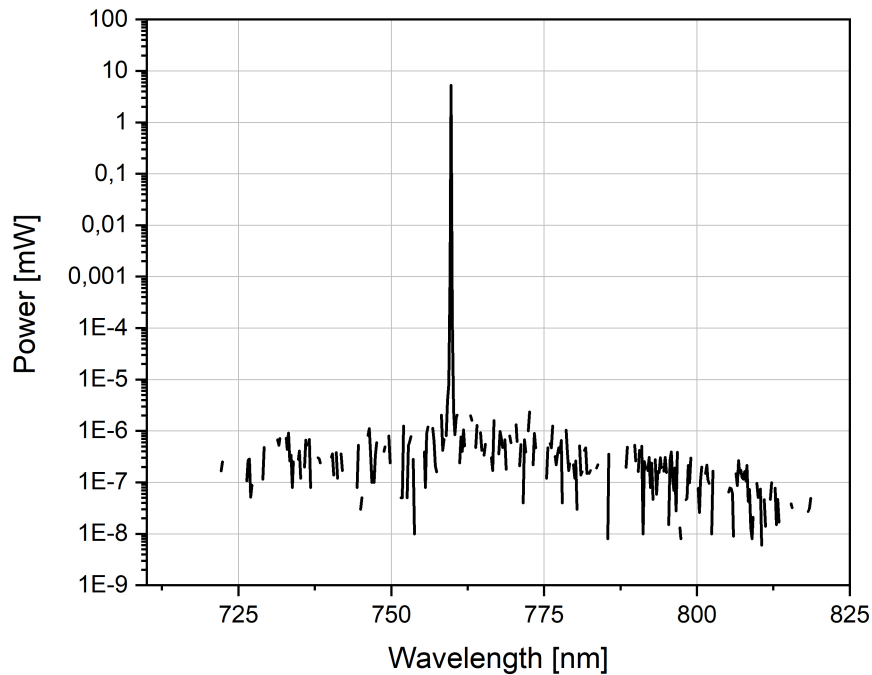
Figure 3.34: Titanium:Sapphire spectrum transmitted by the filter. Resolution 0.1 nm.

As shown in fig.(3.37) the transfer function of the grating was characterized also far from the magic wavelength: for these measures the laser frequency change is performed by tilting the internal grating of the extended cavity sweeping all the range of possible wavelength. The optical power is again measured with the power meter, but if for the incident beam there are no difference for the diffracted power this instrument is located after the optical fiber: doing this it is possible to consider a smaller portion of the solid angle that couples in fiber as well as it reduces eventual background power diffracted as example at higher orders (little relevant in the previous case because of the greater power involved) improving the accuracy of the measurement.

In order to improve the filter capacity of the Volume Bragg grating it is possible to use this instrument in a double pass configuration, provided it does not lose too much laser power.

I realized the optical system shown in fig.(3.35) [55].

Figure 3.35: Optical scheme of the volume bragg grating in double pass configuration

Before to be filtered, the incident beam passes through a polarising beam splitter cube (PBS) that transmits all the laser power already horizontally polarized. I applied a $\lambda/4$ plate to the reflected beam that circularize the laser polarization and 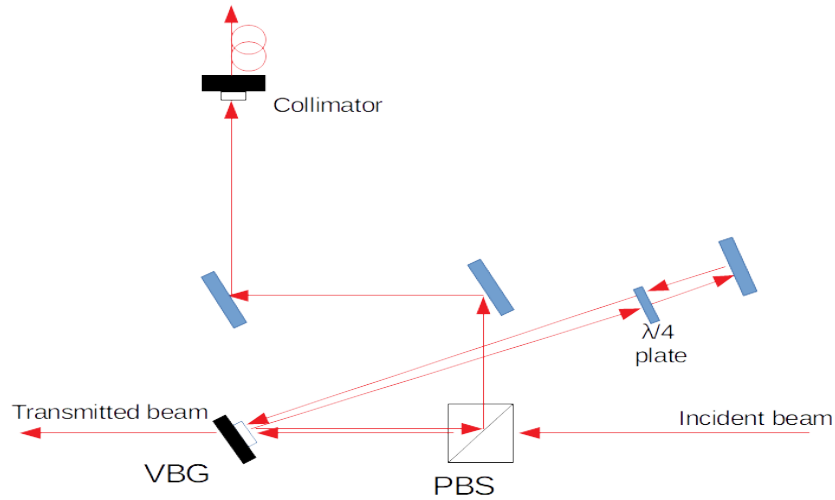then a mirror to retro-reflect on the grating the diffracted beam to filter it another time: passing another time through the plate the circular polarization is again linear but now vertically. After the second filtration I can extract the radiation with vertical polarization using the cube beamsplitter that reflects this beam and with two mirrors I can couple the filtered light into the optical fiber. Before using that set-up it is necessary to study if the filter behaves in the same way for horizontal and vertical state of polarization: so the incident polarization was rotated to vertical and I repeated the characterization of the transfer function near the magic wavelength as discussed previously: I measured a maximum diffracted efficiency of $90.85(5)\%$ and a FWHM=$27.33(1)\,$GHz. These values are not compatible with the ones measured previously but they are of the same order of magnitude, so the filter is valid for both the polarization states and it is acceptable to use the grating also in double pass.

The first measure that carried out with the optical system shown in fig.(3.35) is the filter characterization near the maximum after it is to the magic wavelength by tilting the grating angle. As already said the output power after the optical fiber has been measured with the power meter and knowing the coupling efficiency $\eta = 59\%$ it is possible to normalize it to consider only the effects provided by the filter. The transfer function obtained is shown in graph.(3.36) and it was possible to estimate a maximum efficiency of $87.4(1)\%$ and a FWHM=$19.707(8)\,$GHz. Comparing these results with the ones obtained for the case of single pass there is not a significant reduction of power, suggesting that the carrier passes quite unaltered through the filter during the second pass, while the bandpass is reduced down to $20\,$GHz.
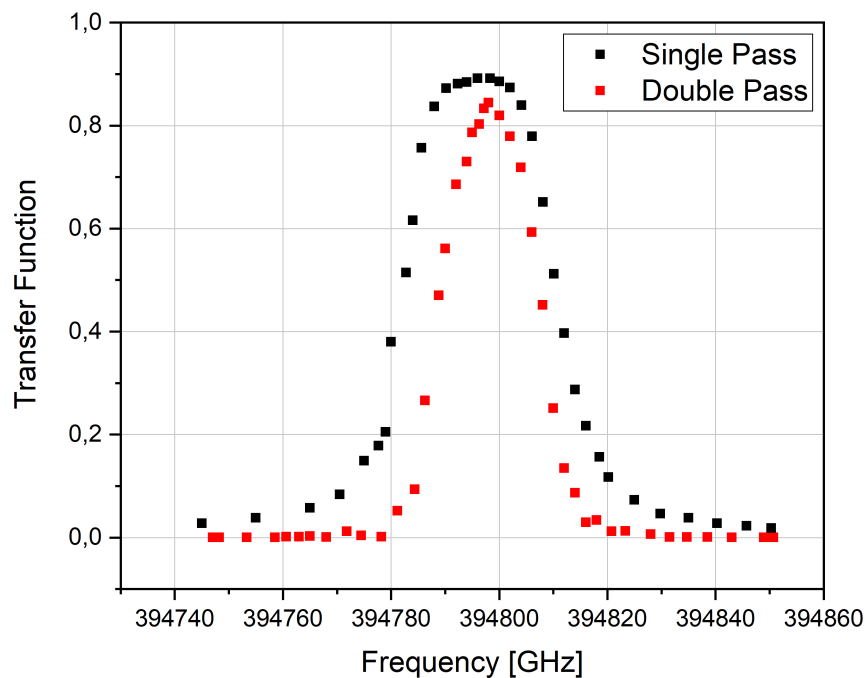
Figure 3.36: Comparison between the transfer function of the Optigrate VBG used in single and double pass near to the maximum.

This last statement can be supported from a numerical example of the power involved in the double pass Optigrate filter: for about 600 mW of incident power from TA, the power transmitted at the first pass is about 45mW while at the second pass it is possible to measure less than 4 mW. It means that the loss of power at the first pass is mainly constitutes by the ASE detuned from the filter bandwidth, so the efficiency for the in-filter frequencies would be greater than what estimated previously.

Knowing now how the double pass filter behaves near to the magic wavelength it is necessary to study the transfer function also far from that, sweeping all the frequency range of emission of the laser system (between 390 000 GHz and 396 400 GHz) acting on the grating of the diode extended cavity to detune the carrier and study its attenuation. The output power was measured in two different ways: first using the power meter placed out of the optical fiber like done for the single pass configuration, then sending the power coupled in fiber to the OSA and measuring the carrier attenuation from the acquired spectrum (as shown as example in fig.(3.38). Improving the alignment of the fiber it is possible to achieve a better coupling efficiency equal to about 78 % and it is taken into account to normalize the measured data.

In fig.(3.37) are reported the measurements carried out in the first way comparing them with the analogous ones obtained from the single pass filter configuration.
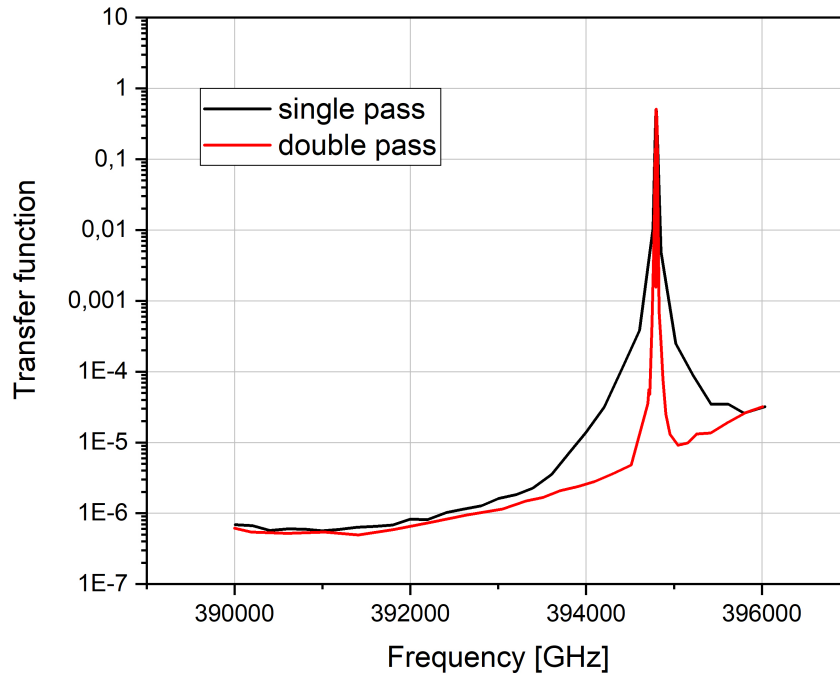
Figure 3.37: Comparison between the transfer function of the filter far from magic wavelength in conditions of single (black curve) and double pass (red curve).

In this figure the main differences are present only near to the maximum of transmission, where the double pass transfer function shows a narrower band, while far from 394 798 GHz the two curves seem to overlap. I note the presence of a not constant background that increases with the frequency: from the fig.(3.38) is evident that it is attributable to the portion of amplified spontaneous emission at frequency in the bandwidth of the filter and for this reason it is not suppressed. This explanation is reinforced from what was discussed previously about the saturation effects in the amplifier, for which tuning the laser far from the maximum of gain, the ASE spectrum becomes more relevant. Measuring with the power meter it is not possible to exclude this contribution and so when the attenuated carrier is comparable or lower I can not perform an accurate characterization of the filter.

The second method allows to solve this problem estimating the effective transfer function of the volume Bragg grating in double pass configuration, excluding thanks to OSA the in-filter ASE contribution. It was possible to perform the measurements only in the frequency range from 394243GHz to 395 301 GHz, outside of which the the peak of the attenuated carrier is not distinguishable from the noise background of the OSA.For this reason, out from this interval the value estimated from the last measurements has been assigned to the transfer function setting T=7.84×10^{-9} for the frequencies higher than 395 301 GHz while T=1.08×10^{-8} for the frequencies lower than 394 243 GHz. This probably means to overestimate the filter attenuation in these frequency ranges, but it is the best choice possible because of the inability to obtain other data.
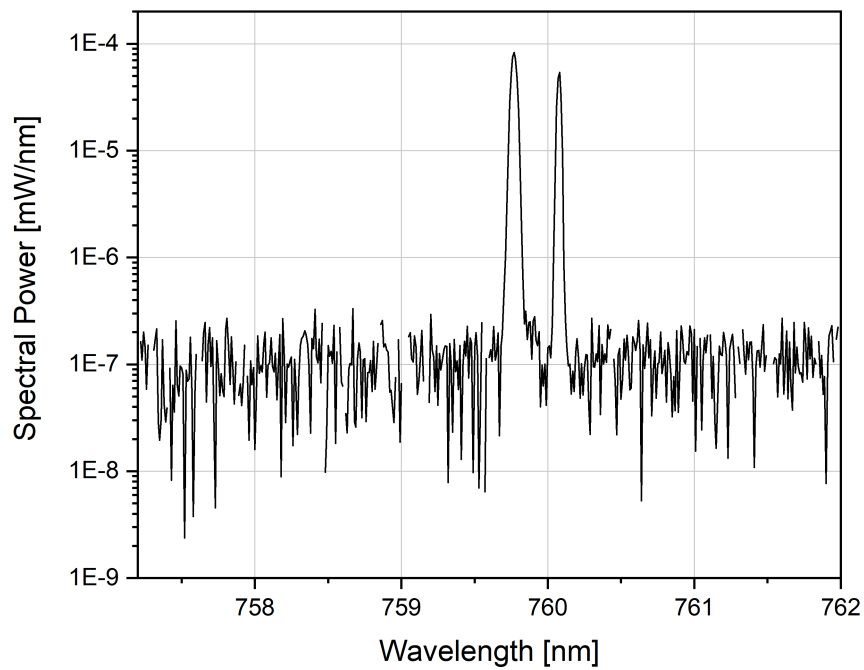
Figure 3.38: Example of filtered spectrum with carrier detuned from magic wavelength. **Left peak** ASE in filter at 394 798 GHz.**Right peak** Carrier at 394 577 GHz.Resolution 0.03 nm.
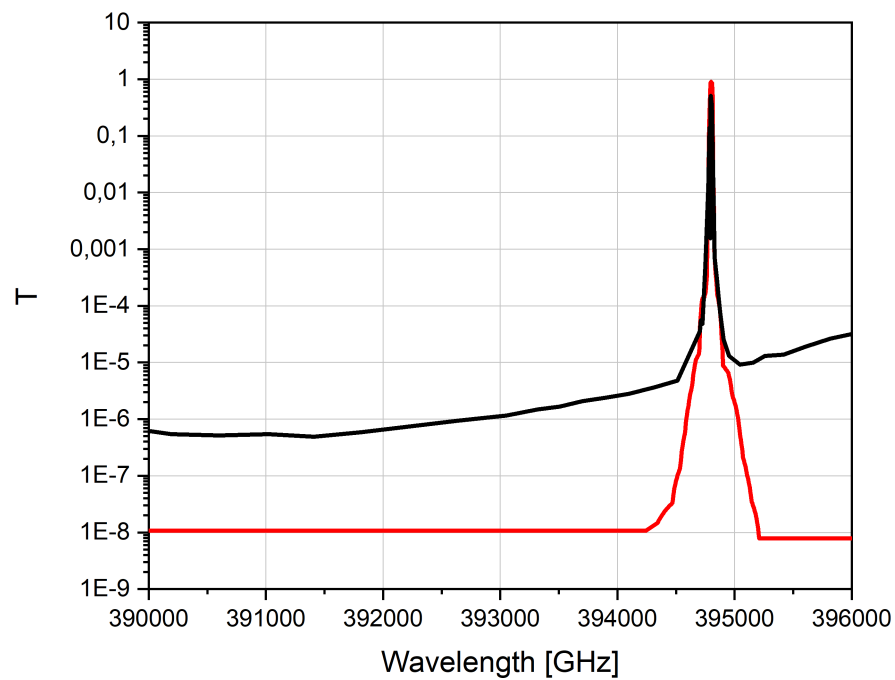
Figure 3.39: Grating transfer function measuring the output power after the fiber: **Black** with power meter;**Red** with OSA.

In the graph.(3.39) I compare the transfer function obtained by using the two different techniques. It is evident that they are equivalent near to the maximum, while when the carrier is at the same order or lower respect to the in filter ASE power the second method allows me to perform a more accurate measure in a larger frequency range. Far from the magic frequency, even if I overrated the transfer function assigning a constant value, it is about 20 dB lower than the value estimated with the first method.

Chapter 4

ASE light shift calculation

Knowing the ASE spectral distribution and the transfer function of the different filters, it is possible to estimate the light shift that would be induced by the detuned ASE radiation on the ytterbium clock transition $^1S_0 \rightarrow^3 P_0$ realizing the optical lattice with the laser system that described in the previous sections. SUpposing that the narrow laser emission is tuned at the magic wavelength and stabilized with locking in cavity it does not provide any contribution to the dipole polarizability induced lattice shift, generating only a contribution from superior orders that I do not take in account in this work and it is already estimated [23].
For this reason I concentrate my efforts only in the ASE contribution that constitutes the main contribution induced by the semiconductor laser.

4.1 Estimated ASE light shift

First of all it is interesting to estimate the light shift induced by ASE if the lattice would be realized with the radiation emitted by the tapered amplifier without any kind of filtering.

Setting the operation condition of TA current I=3200 mA it is possible to acquire the spectrum with the OSA limiting the input power at 10 mW (limit of the instrument), reducing it with the half-wave plate/PBS couple used like power modulator in the scheme in fig.(3.9). The spectrum has been normalized to simulate the ASE that would be present with a total input power P=1 W (including the carrier). This value has been chosen conventionally in analogy to the maximum power emitted by the Ti:Sa currently used. Experimentally the laser power employed in trapping atoms is lower, typically between about 400 mW and 800 mW (corresponding to a lattice depth to about $200\,E_R$ and $400\,E_R$), so the effective light shift would be lower than what here estimated. The normalized ASE spectrum was fitted using the expression (2.2) and I report the fitting parameters in tab.(4.1.1).

ASE parameters,I=3200 mA,TA power=1 W	
A	$5.38(2) \times 10^{-7}$ mW/GHz/nm
ν_0	$390\,406(10)$ GHz
$\Delta\nu_{ASE}$	$5040(20)$ GHz

Table 4.1.1: Fitting parameters of the ASE spectrum simulating a total input power of 1 W.

Because it is a diffused spectrum, to calculate the lattice shift induced by ASE it is necessary to integrate on the frequency domain the spectral distribution of ASE power for the difference of polarizability adapting the expression (2.23):

$$\Delta\nu_{LS} = -\int \frac{4\Delta\alpha(\nu)}{h\pi\epsilon_0 w_0^2} P_\nu(\nu)d\nu \qquad (4.1)$$

considering the spectral density $P_\nu(\nu)$ obtained normalizing the spectral power acquired by the OSA for its resolution (in this case 0.1 nm, so about 52GHz). It is possible to distinguish two light shift contributions: one induced by the ASE spectrum red-detuned (so with a frequency lower than the magic one) and one induced by the blue-detuned ASE (so the radiation at frequency higher than the magic one). In fact at the magic frequency $394\,798$ GHz the quantity $\Delta\alpha(\nu)$ changes its sign, giving a light shift with opposite sign for the two sides. For this reason the integral (4.1) was calculated fixing the extremes of integration between $377\,263$ GHz and magic frequency and between magic frequency and $402\,595$ GHz. These value have been chosen to include only the part of the spectrum higher than the instrumental noise background.

ASE induced Lattice Shift			
	red-detuned	blue detuned	sum
Light shift/Hz	+1292,74	-5,04	+1287,7

Table 4.1.2: ASE induced light shift calculated for the TA spectrum unfiltered.

In tab.(4.1.2) I report the results of light shift calculation.
It is evident that because of the strong asymmetry with respect to the magic frequency of the ASE spectra there is a high imbalance between the contribution of the red and the blue detuned parts that generates a light shift different by more than two orders of magnitude. After adding the two results, the estimated fractional systematic uncertainty on the determination of the ytterbium clock frequency $(518\,295\,836\,590\,863.59(31)$ Hz$)$ is equal to 2.5×10^{-12}, an enormous value that would make the clock unusable. From this calculation it is clear that, despite its suited characteristics in realizing transportable clocks, it is impossible to use an amplified semiconductor laser to obtain an optical clock with uncertainty of 1×10^{-18} without filtering the ASE emitted by TA.
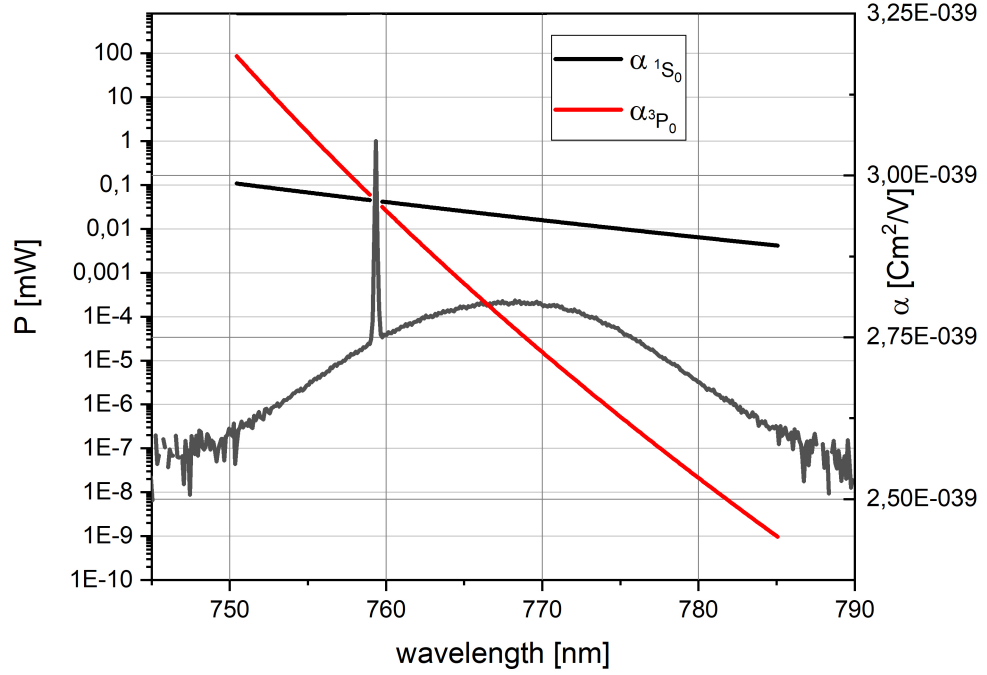
Figure 4.1: Comparison between TA spectrum and ytterbium clock states polarizabilities. By tuning the carrier at magic wavelength the difference of polarizability is zero, so all the light shift contribution is carried by the ASE spectrum

4.2 ASE light shift with filter

After I characterized the transfer function of different filtering systems, it is possible to use these data to estimate the light shift induced by the filtered ASE. The aim is to achieve a lattice light shift lower or of the order of 10×10^{-18}, allowing to use this laser to generate the optical lattice on IT-Yb1.

As already done in the previous section (4.1) it is possible to simulate the typical operating conditions of an ASE spectrum emitted from a TA with injection current I=3200mA and 1W of laser power incident on atoms. The ASE spectral density $P_\nu(\nu)$ was calculated from the fitting parameters of spectral power and normalized by the resolution. In absence of a function to fit the Transfer function of the filters, $T(\nu)$ is obtained interpolating the measured data to obtain a numerical expression and it has been multiplied to ASE spectral density to simulate the ASE after the filter. Knowing these quantities the expression (4.1) can be edited in the form:

$$\Delta\nu_{LS} = -\int \frac{4\Delta\alpha(\nu)}{h\pi\epsilon_0 w_0^2} T(\nu) P_\nu(\nu) d\nu \qquad (4.2)$$

and solving numerically the integral one can calculate the ASE induced light shift

after the filter.

The filter characterization is performed measuring the diffracted power and maximizing it by tilting the grating: it is not possible to know during the measurement campaign how much it is well aligned, i.e. when the transfer function peak matches with the magic wavelength. This problem has been solved by estimating how much one is able to well align the filter using this technique and I choose as a convection that the filter is well tuned when the carrier falls in the frequency range where the normalized efficiency is more than $90\,\%$. It is a reasonable value easily reachable with an hand-made tuning, without electronic system to stabilize the power, furthermore in this range it is easy to see if the filter is close to the maximum of efficiency. Maybe this interval could appear as overestimated, but it is necessary to consider the fact that during the measure the filter can be perturbed from external stimuli, such as mechanical stresses, or from thermal effects due to the laser power absorbed that misaligns the filter from the position tuned at the begin.

In order to estimate the maximum light shift induced by the residual ASE in different filter configurations, I assign to it the difference between the value estimated at the extremes of the range of confidence that I chose for the filters, considering that in all the measurements campaign the filter will fall in this confidence range.

Before calculating this quantity, it is interesting to know which part of the spectrum gives the largest contribution to the total light shift. I define the cumulative light shift at frequency ν as the integrated light shift for all the frequencies smaller than ν. Clearly the rightmost value of the cumulative light shift is the total light shift [49].

As an example in fig.(4.2) is shown the cumulative light shift calculated for the Volume Bragg grating manufactured by Optigrate comparing the two different configurations.
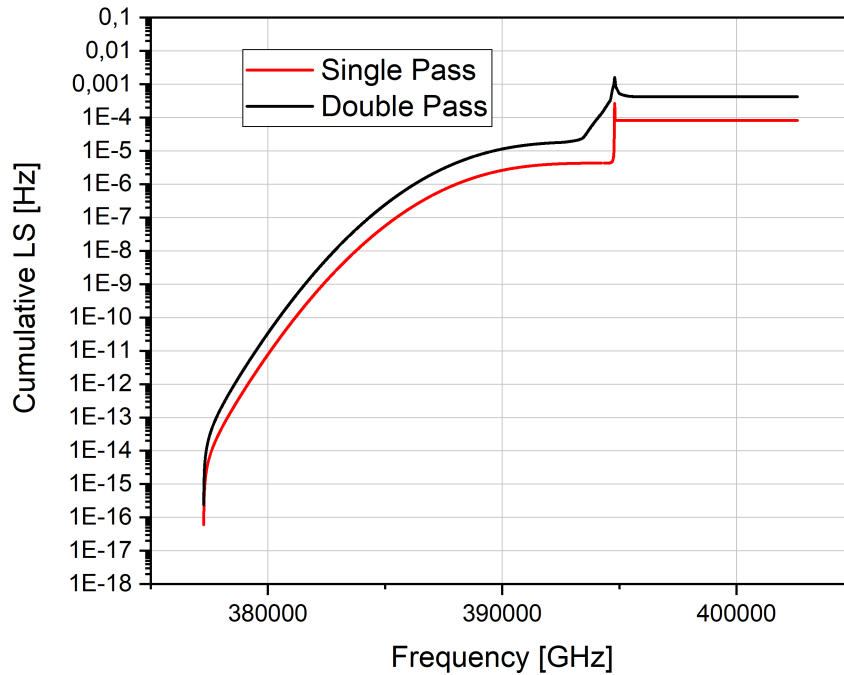
Figure 4.2: Cumulative Light shift calculated for the Optigrate filter in double pass configuration

It is evident that for both the curves here represented the most important contribution is provided by the ASE near the center of the filter, i.e. where it is less attenuated. The asymmetry of the ASE spectrum has as consequence the fact that the light shift induced by the red detuned frequencies do not cancel out with the one from blue detuned frequencies, so the final balance is not null. For this reason, to save calculation time, it is reasonable to neglect the far detuned parts of the spectrum that contribute less than 1% to the total light shift. Moreover it is possible to estimate the effects of the Toptica filter, whose transfer function was characterized only near the center.

In the following tables (4.2.1), (4.2.2), (4.2.3) and (4.2.4) are reported the estimated light shifts for the different filter configurations. I separated the interval of integration for red detuned frequencies (left part of the spectrum) and blue detuned one (right part of the spectrum) that contribute to total light shift with opposite sign: the firsts provide a positive shift to the measure of the clock frequency while the seconds give a negative contribution. As discussed previously I calculated it for a filter centered on magic wavelength and detuned at the extreme of the interval where the diffraction efficiency is over 90%.

Toptica Single Pass				
Filter detuning	Left/Hz	Right/Hz	Sum/Hz	Fractional LS
0 GHz	8.26×10^{-3}	-2.37×10^{-3}	5.88×10^{-3}	1.1×10^{17}
16 GHz	4.95×10^{-3}	-4.43×10^{-3}	5.18×10^{-4}	1.0×10^{-18}
-16 GHz	1.26×10^{-2}	-1.13×10^{-3}	1.14×10^{-2}	2.2×10^{-17}

Table 4.2.1: Estimated ASE induced light shift calculated for the Toptica filter in single pass configuration detuning the center of the transfer function from the magic wavelength. 90 % Bandwidth $\pm16.6(4)$ GHz;P=1 W.

Toptica filter double pass				
Filter detuning	Left/Hz	Right/Hz	Sum/Hz	Fractional LS
0 GHz	3.55×10^{-3}	-3.8×10^{-3}	-2.50×10^{-4}	-4.8×10^{-19}
13.7 GHz	20.7×10^{-3}	-5.95×10^{-3}	-3.88×10^{-3}	-7.5×10^{-18}
-13.7 GHz	5.73×10^{-3}	-2.25×10^{-3}	3.47×10^{-3}	6.7×10^{-18}

Table 4.2.2: Estimated ASE induced light shift calculated for the Optigrate filter in single pass configuration detuning the center of the transfer function from the magic wavelength. 90 % Bandwidth $\pm14.7(4)$ GHz;P=1 W.

Optigrate VBG single pass				
Filter detuning	Left/Hz	Right/Hz	Sum/Hz	Fractional LS
0 GHz	1.56×10^{-3}	-1.13×10^{-3}	4.24×10^{-4}	8.2×10^{-19}
9 GHz	1.1×10^{-3}	-1.8×10^{-3}	-6.9×10^{-4}	-1.3×10^{-18}
-9 GHz	2.3×10^{-3}	-7.4×10^{-4}	1.56×10^{-3}	3.0×10^{-18}

Table 4.2.3: Estimated ASE induced light shift calculated for the Optigrate filter in single pass configuration detuning the center of the transfer function from the magic wavelength. 90 % Bandwidth $\pm9.0(3)$ GHz;P=1 W.

Optigrate VBG double pass				
Filter detuning	Left/Hz	Right/Hz	Sum/Hz	Fractional LS
0 GHz	2.56×10^{-4}	-1.03×10^{-4}	5.29×10^{-5}	1.0×10^{-19}
4 GHz	9.53×10^{-5}	-3.53×10^{-4}	-3.53×10^{-4}	-6.8×10^{-19}
-4 GHz	3.71×10^{-4}	-1.22×10^{-4}	2.49×10^{-4}	4.80×10^{-19}
10 GHz	2.90×10^{-5}	-7.99×10^{-4}	-7.70×10^{-4}	-1.49×10^{-18}
-10 GHz	6.99×10^{-4}	-3.38×10^{-5}	6.65×10^{-4}	1.29×10^{-18}

Table 4.2.4: Estimate ASE induced light shift calculated for the Optigrate filter in double pass detuning the center of the transfer function from the magic wavelength. 90 % Bandwidth $\pm4.0(2)$ GHz;P=1 W.

Detuning the filter from the magic wavelength the contribution from the right or the left part of the ASE spectrum prevails on the other increasing in general the absolute

value of the light shift respect to the centered case. It is not always true because the asymmetry of the ASE spectrum and the asymmetry of the transfer function.

Best performances are obtained by the filters with a closer bandwidth, where the confidence range of frequency for which the efficiency is higher than 90 % is smaller and so it is simpler to well align the grating. For the Optigrate in double pass I calculated the light shift also for the extremes condition of filter detuning at the exterems of the filter bandwidth (where the efficiency is 50 % of the maximum)

In table(4.2.5) are compared the maximum light shifts estimated as difference between the values calculated at the extremes of the interval.

Maximum Light Shift		
	LS/mHz	Fractional LS
Toptica single pass	10.88×10^{-3}	2.1×10^{-17}
Toptica double pass	7.35×10^{-3}	1.4×10^{-17}
Optigrate single pass	2.25×10^{-3}	4.34×10^{-18}
Optigrate double pass	0.54×10^{-3}	1.05×10^{-18}

Table 4.2.5: Maximum light shift estimated in the range of 90 % of filter efficiency with P=1 W.

If the Toptica filter can achieve a maximum fractional light shift (in absolute value) of the order of 10^{-17} for both the configurations, making it usable to realize optical lattice. Regarding instead the Optigrate volume Bragg grating, I estimated a light shift in the low 10^{-18}, achieving the goal of 1×10^{-18} at 1 W of lattice power for the double pass configuration.

Moreover the loss of power respect to the single pass version is very low. As an example for about 600 mW incident I measured about 45 mW transmitted at the first pass while less than transmitted4 mW at the second: it means that the main part of the power transmitted at the first pass is constituted by the detuned ASE not diffracted by the filter. For this reason the efficiency measured using only the power meter must be considered underestimated respect to the real one referred to the carrier.

As shown in tab4.2.4, for the filter that I choose I also calculated the ASE induced light shift increasing the hypothetical misalignment of the grating until the limit of the bandwidth, so simulating that the transfer function is so detuned that the diffraction efficiency of the carrier is the 50 % respect to the maximum. This is an extre case because, also if I can not tune the center of the filter position at GHz level, I can easily notice if the grating is so much detuned. Anyway, also in this unrealistic subject of study the maximum estimated light shift generated by ASE detuned from magic wavelength is in absolute value equal to 1.5×10^{-18}: this is a result better than the single pass configuration of the same filter.

However it is quite simple to align manually the filter minimizing the power transmitted by the volume Bragg grating to keep the diffraction efficiency above 90 %, i.e. limiting the detuning from magic wavelength under 4GHz. Considering an ideal well centered and stable grating, it is possible to conclude this section stating that the filter system here described could achieve a light shift induced by ASE lower than 10^{-19}, less than the actual fractional uncertainty of the clock IT-Yb1. This would allow use of

this tapered amplified laser diode to realize an optical lattice within the prefixed aim. It is important to note that these last reasonings are only theoretical speculations that do not take in account the fact that I can not tune the filter transfer function at GHz level but I can only align it in a frequency range around the magic wavelength.
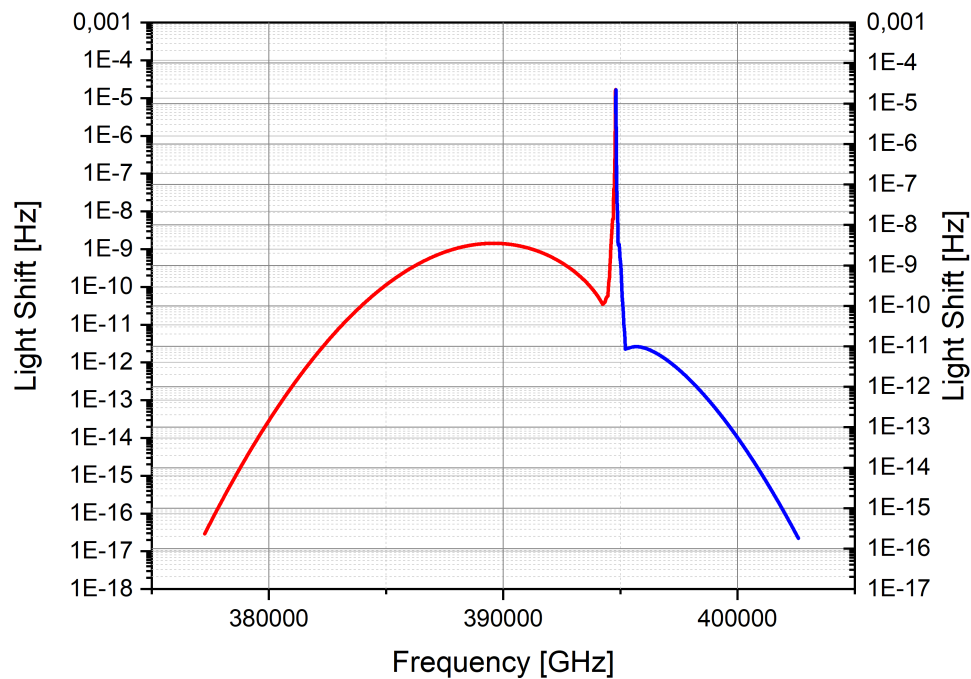

Figure 4.3: Estimated light shift for the double pass volume Bragg grating. **Red** LS induced by red-detuned frequency. **Blue** negative LS induced by the blue-detuned frequencies

In figure (4.3) it is shown the light shift for the volume bragg grating i double pass configuration distinguishing the positive contribution from red-detuned frequencies and the negative from blue detuned one (here represented in absolute value). Close to magic wavelength the slope of the light shift is very steep while far it becomes more flat: the first case is where I was able to measure the transfer function of this grating, that is in the interval between 394200 and 395 300 GHz, while the second is where the value of T was conservatively estimated fixing a constant value equal to the the minimum measured one. For this reason out of filter range the estimated light shift follows a trend similar to the ASE spectrum. By comparing the slope between these two regions, there is further a proof that the filter is doing its work correctly. Moreover it means that also the light shift contribution from the wings is overestimated. For the left part it is not a problem because it represents less than 1 % of the total light shift (so it is excluded by the calculation as previously said), while for the right part it affects the measure because the out of filter contribution represents about the 3 % of the red-detuned light shift.
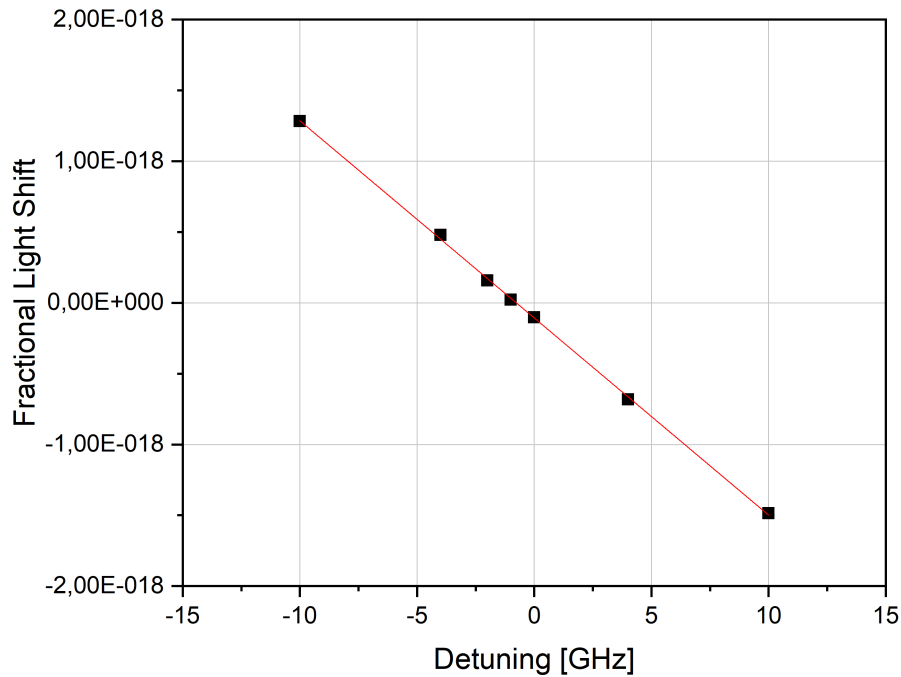
Figure 4.4: Estimated light shift in function of the detuning of the transfer function respect to the the magic wavelength, obtained for the volume Bragg grating in double pass

Before to conclude this section it is possible to discuss about the role of the ASE asymmetry: as already seen the carrier at magic wavelength is located at one side of the the ASE spectrum and not at the center, so the spectral density at its right its different from the one at its left. Moreover, observing the tables that contain the light shift calculations, the values obtained for filter with center at magic wavelength are not the average between the ones for filter detuned. This suggests that it would be possible to decrease the estimated ASE light shift tuning the filter slightly toward positive frequencies, in order to reduce the left contribution. Fitting linearly the data obtained for the filter that I used I estimated a filter detuning to minimize this ASE light shift at $-0.58(1)$ Hz from magic wavelength. Applying my model to simulate the filter detuned of this quantity I obtained a light shift of 1.17×10^{-5} Hz and a fractional uncertainty of 2.3×10^{-20}.

Chapter 5

Trapping atoms with TA

The laser system developed and described in this work has been applied to realize the optical lattice on ytterbium lattice clock IT-Yb1, as shown in fig.(5.1). Because of it is no stable the laser has been tuned at magic wavelength using the piezoelectric control reading it from the wavemeter Bristol Instruments 621WM. The fiber coming from the clock has been connected to the collimator of the high power fiber coupling. It makes it possible to send the laser at 759 nm to the atoms to realize the lattice. This fiber presents a different numerical aperture NA with respect the one that previously used, so the coupling efficiency maximized for this optical system was reduced [56]: for this reason, from about 560 mW of incident power is sent to atoms only 307mW against the about 440 mW achieved with the previous alignment (with a coupling efficiency of about 78 %).

First of all, to observe if the lattice realized by this optical system is operating correctly it is possible to perform an absorption imaging of the atomic ensemble trapped in the lattice generated by the TA laser emission. Atoms generate an optically dense vapour with density N that can interact with resonant laser beams, absorbing incident photons. When the light goes through this atomic cloud of length Δz it can interact with $N\Delta z$ atoms for units of area with a certain probability dependent by the absorption cross section σ. The infinitesimal variation of the laser intensity is described by $dI/dz = -\sigma N\Delta z$, and integrating this expression on the space coordinate one obtains the Lambert-Beer law:

$$I = I_0 \exp\left(-N\sigma(\omega)z\right) = I_0 \exp\left(-OD\right) \tag{5.1}$$

where the quantity $OD = N\sigma z$ is the optical density of the atomic cloud. Supposing that ultracold trapped atoms are quite immobile so the Doppler effect is neglectable, all the cloud see the incident photons with the same frequency, so optical density is directly related to the atomic density.

Figure 5.1: Photograph of the optical system described in this thesis applied on IT-Yb1.
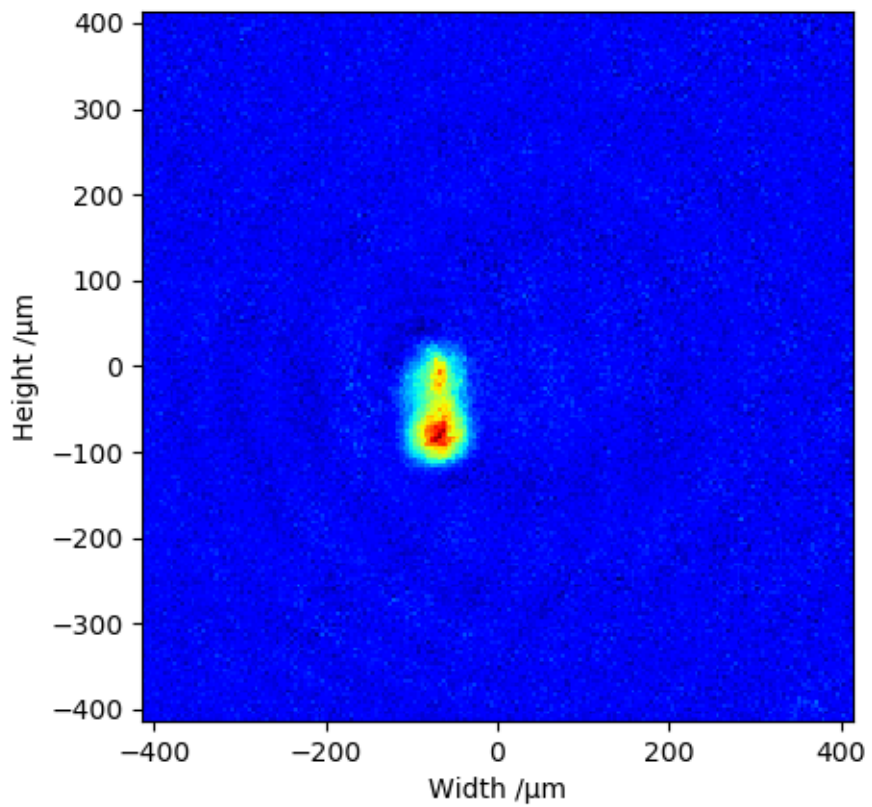

Figure 5.2: False color image acquired in absorption of the atomic gas distribution

To estimate the OD of the atomic ensamble in absorption a laser beam at 399 nm is employed, stimulating the strong $^1S_0 \rightarrow ^1P_1$ transition for which ytterbium atoms has high absorption probability. Using a photodiode two images in different conditions have been acquired: the first is obtained when the atomic cloud is present and so the blue laser is attenuated passing through the vapour. It defines the intensity distribution I_{atoms}. Then a second picture is taken after the lattice was turned off and the cloud is missing. It allows to know the distribution of the image beam I_{img}. Should be useful also to acquire a further picture of the I_{dark} turning off the laser to compensate the background from, as example, scattered light from free atoms or from thermal noise.

From equation (5.1) the measured optical density is equal to [57]:

$$OD = \ln \frac{I_{img} - I_{dark}}{I_{atoms} - I_{dark}} \tag{5.2}$$

and after mediating among about 400 acquisitions one can obtain the picture in fig.(5.2). It is represented in false colour where the red represents a maximum OD of about 0,3 while the blue is zero. From this imaging it is possible to estimate coarsely the cloud size, that presents a height of about 135 μm and a width of 91 μm. The gravitational acceleration is aligned with the vertical direction of this picture, as shown by the spatial distribution of the atoms, denser at the bottom.

After demonstrating that this optical lattice al 759nm from TA can trap ytterbium atoms, it is now interesting to use IT-Yb1 to realize some clock measurements.

The first measure here presented is the spectroscopy of the clock transition, shown in fig.(5.3).
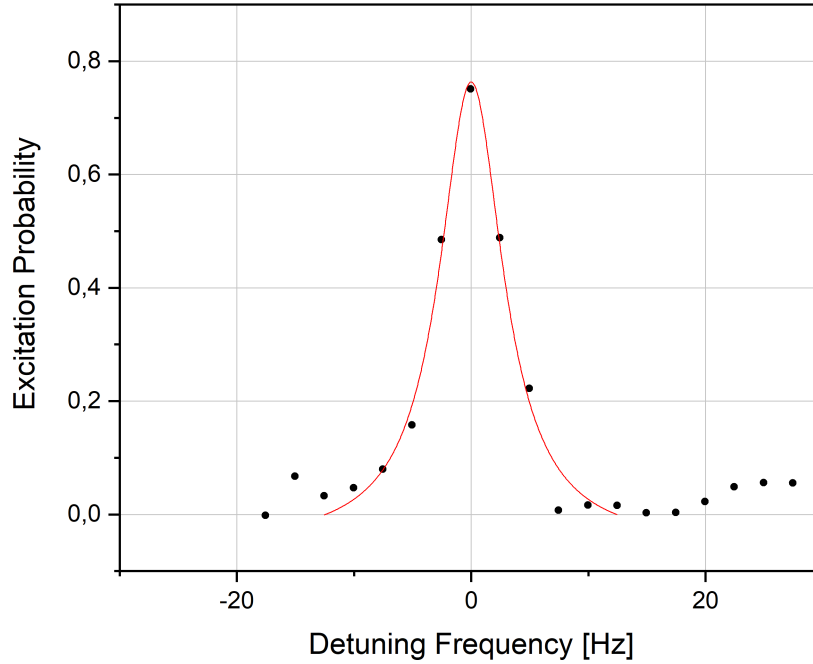
Figure 5.3: Excitation of the clock transition varying the detuning from the clock frequency 518295836590864 Hz

Applying a magnetic field, the $^1S_0 \rightarrow ^3 P_0$ transition is separated in two lines depending on the spin state $m_F = 1/2$ or $m_F = -1/2$ [23]. After the process of spin polarization it is possible to obtain a spin purity of 98% and so it is possible to study only a single magnetic component with a Rabi spectroscopy, like shown here. After the frequency of the maximum of excitation of the clock transition has been found, it is possible to sweep all the range of frequencies around it to study how the interaction probability changes moving from the resonance. This process is performed changing the frequency of the P_{RF} provided to an acousto optic modulator which is applied to the probe laser at 578 nm. Fitting the center of the excitation curve with a Lorentzian function and it is possible to estimate a FWHM equal to 6.7(6) Hz. The time of the Rabi pulse is 60 ms and it means a Fourier limit of about 6.6 Hz, compatible with the one obtained by the fit.

Another interesting measure that it is possible to perform is a sideband spectroscopy of the clock transition, as shown in figure (5.4): the main difference from the previous narrow line spectroscopy is that the power of the probe laser at 578 nm is now higher as well as the Rabi time of interrogation is increased. The peak of excitation probability is strongly broadened because of the phenomenon of power broadening [58] which is added to the natural linewidth of the transition: from a Lorentzian fit of the carrier (the central peak of the figure) it is possible to estimate a FWHM equal to 3300(200)Hz, widely superior to the 6.7 Hz previously measured.
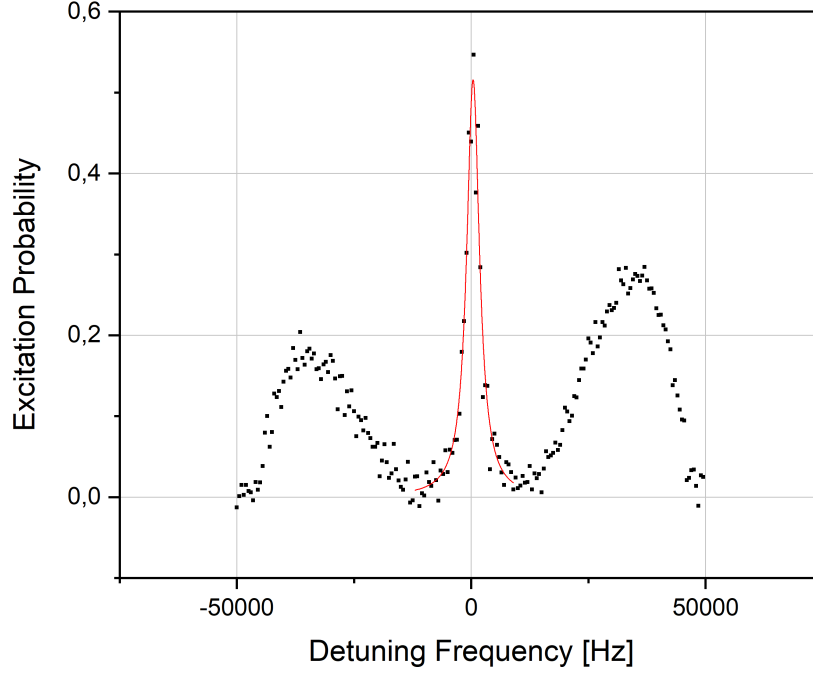
Figure 5.4: Sideband spectroscopy of clock line

The advantage of stimulating the $^1S_0 \to^3 P_0$ transition at high power is the possibility to observe also two sidebands detuned from the clock frequency and less intense than the central carrier. This phenomenon is generated by the lattice trapping, because atoms are confined in quantum potential holes approximable as quantum harmonic oscillators. Depending on their temperature, atoms are distributed with a certain probability to populate different levels with motional state n. While the carrier does not present a change of this quantum number, if the frequency of the Rabi pulse is sufficiently detuned from the resonance it is possible that there is also a change of the lattice vibrational state with $\Delta n = n^e - n^g \neq 0$. For this reason the two sidebands arise: the blue is the one at the right where $n^e = n^g + 1$ and the red is the one at the left, with $n^e = n^g - 1$. Causing the excitation or the de-excitation of a vibrational quantum the first is at higher while the second at lower energy.

The importance of the sideband spectroscopy derives from the informations about the lattice that it allows to extract [59].

The motional frequency ν_Z is represented by the detuning of the sidebands from the carrier and it depends on the intensity of the trapping potential. $h\nu_{max}$ is the energy of the motional quantum at the center of the potential hole, so where the confinement is stronger. As the temperature of the atomic ensemble approaches $0\,\mathrm{K}$ all atoms are still and well confined at the center of the hole subjected to the same trapping potential: in this conditions the sidebands tend to become tighter and tighter and peaked around $\pm\nu_{max}$. Hotter atoms, instead, are able to move from the center of the trap so they are subjected to a weaker potential to which it is associated a lower motional frequency:

their contribution causes the sidebands broadening.

The lattice depth U_0 is related to the longitudinal motion frequency ν_z following the expression:

$$h\nu_z = 2E_R\sqrt{\frac{U_0}{E_R}} \tag{5.3}$$

where $E_R = h\nu_R$ is the recoil energy and ν_R is the recoil frequency that for the ytterbium atom is equal to $\nu_R \simeq 2\,\text{kHz}$. To study the maximum lattice depth it is necessary to use the appropriate value of longitudinal motional frequency, so ν_{max} estimate from the graph equal to about $48\,\text{kHz}$. From (5.3) one can obtain $U_0 \simeq 144\,\text{E}_\text{R}$. It is a quite small lattice depth because typical clock measurements are performed between 200 and $400\,\text{E}_\text{r}$, but it is enough to trap atoms in lattice. Considering that the sidebands magnitude depends on the atomic temperature on the lattice axis T_z, it is possible to estimate it calculating the ratio between the excitation fraction of the blue and red sideband b_{br} and using [60]:

$$k_b T_z = \frac{h}{\nu_z \ln b_{br}} \tag{5.4}$$

Using the appropriate values for b_{br} and ν_z one can obtain Tz=$4.7\,\mu$ K. This value seems to be reasonable because it is of the same order of magnitude of the typical atomic temperature, as described in section (1.5).

At the end it is important to measure the clock instability of interleaved measurements. Currently at INRiM there is not an optical clock with better performances than IT-Yb1, so it has been measured calculating the Allan deviation between measurements of the same clock [23]. The results are shown in fig.(5.5).
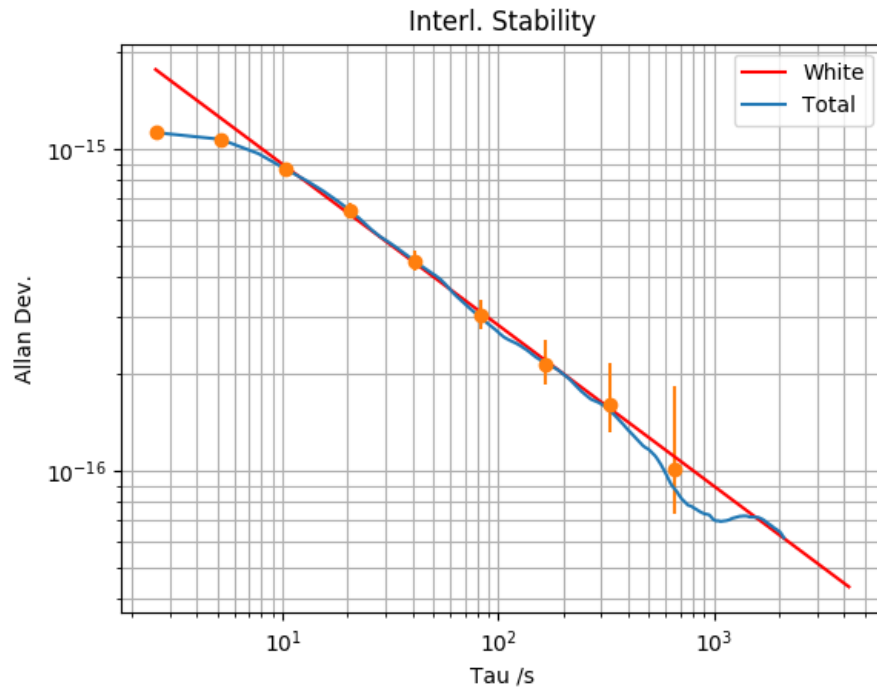
Figure 5.5: Allan deviation of the clock measured for the atoms trapped with the TA

The red line represents the trend of the Allan deviation of the white noise, that decreases linearly with slope equal to the $\sqrt{\tau}$, where τ is the measurement time.

Chapter 6

Conclusions

In this work I proved that it is possible to apply a semiconductor laser to trap atoms in an optical lattice in atomic optical clocks with an ASE induced fractional lattice shift of the order of low 10^{-18} or better. I developed a theoretical model to estimate the dynamic Stark shift induced by electric dipole polarizability effects and I calculated it for the case of ^{171}Yb, achieving a good agreement with the experimental results. I realized experimentally an optical system to study and manipulate the radiation emitted by a tapered amplified laser diode in order to realize an optical lattice and I applied to IT-Yb1.

I characterized the background spectrum of amplified spontaneous emission generated by the semiconductor laser I used, the main limits to their application, studying its distribution and its behavior with optical elements. I observed a strong dependence on the operating conditions, becoming less relevant with respect to the carrier as the injection current increases or if the laser wavelength is close to the maximum of gain of the amplifier. These effects are attributable to the amplifier saturation. I measured an ASE background less intense of about 30 dB at 0.1 nm of resolution with respect to the carrier and setting a typical operating condition of 1 W of optical power on atoms I estimated with the previous theoretical model an ASE induced light shift at the kHz level, that would make impossible to perform good clock measurements. I tested different filter configuration to improve the TA spectral purity, finding in the volume Bragg grating provided by Optigrate used in double pass the best choice. A good alignment of this filter allowed to reduce the estimated fractional light shift from 2.5×10^{-12} to an hypothetical 2.3×10^{-20} at lattice power 1 W. Considering the need to center the filter at the magic wavelength I estimated a reasonable confidence range in which the grating is well aligned and there I assigned a maximum lattice shift of 1.05×10^{-18}. This result makes the TA system suitable for the operation of state-of-the-art optical clocks.

As further proof I trapped ytterbium atoms in IT-Yb1 and I performed some clock measurements such as clock transition and sidebands spectroscopy or interleaved stability, in order to show its good behavior.

The laser system that I developed can be used as a backup by using the volume Bragg grating for the current Titanium:Sapphire in lattice generation and it will make possible to perform comparison between the two systems. Upcoming studies foresee to

perform comparison between the two systems with the target to measure experimentally the ASE induced lattice shift comparing it with the estimation.

The two systems can be exploited for further enhancement of IT-Yb1, for example by realizing 2D lattice confinements, or for the realization of a second clock.

The background spectra filtering on amplified laser diodes seems to provide encouraging results in order to realize optical clocks based on only semiconductor laser sources, even if the spectrally-pure alternatives are still better. It will be possible to apply the knowledge acquired during this work in developing new optical clocks, with a particular attention to compactness, reliability and transportability. While this thesis considered the case of a ytterbium optical clock, the techniques described can be useful for optical lattice clocks based on strontium, mercury, magnesium and cadmium atoms. Semiconductor lasers are ideal for a transportable clock that can find applications for the measurements of Earth gravitational potential or as a travelling frequency standard. The development of space optical clocks also requires an all-semiconductor laser setup and can benefit from the filtering techniques presented in this thesis. Finally, this work will be beneficial to the development of continuously-running optical clocks that are an important step toward the generation of timescales based on optical frequency standards and toward the redefinition of the second.

Bibliography

[1] Bureau International de Poids and Mesures; The International System of Units(SI)

[2] Levi, F.; Calonico, D.; Calosso, C. E.; Godone, A.; Micalizio, S. Costanzo, G. A. Accuracy evaluation of ITCsF2: a nitrogen cooled caesium fountain Metrologia, 2014, 51, 270

[3] Ludlow, A. D.; Boyd, M. M.; Ye, J.; Peik, E. Schmidt, P. O. Optical atomic clocks Rev. Mod. Phys., American Physical Society, 2015, 87, 637-701

[4] Abdel-Hafiz, M.; Ablewski, P.; Al-Masoudi, A.; Mart, H. Á.; Balling, P.; Barwood, G.; Benkler, E.; Bober, M.; Borkowski, M.; Bowden, W.; Ciurylstrok;o, R.; Cybulski, H.; Didier, A.; Dolev zal, M.; Dörscher, S.; Falke, S.; Godun, R. M.; Hamid, R.; Hill, I. R.; Hobson, R.; Huntemann, N.; Le Coq, Y.; Le Targat, R.; Legero, T.; Lindvall, T.; Lisdat, C.; Lodewyck, J.; Margolis, H. S.; Mehlstäubler, T. E.; Peik, E.; Pelzer, L.; Pizzocaro, M.; Rauf, B.; Rolland, A.; Scharnhorst, N.; Schioppo, M.; Schmidt, P. O.; Schwarz, R.; ¸ Senel, ¸ CaBreve; grimath;.; Spethmann, N.; Sterr, U.; Tamm, C.; Thomsen, J. W.; Vianello, A. Zawada, M. Guidelines for developing optical clocks with e-18 fractional frequency uncertainty arXiv:1906.11495, 2019

[5] McGrew, W. F.; Zhang, X.; Leopardi, H.; Fasano, R. J.; Nicolodi, D.; Beloy, K.; Yao, J.; Sherman, J. A.; Schäffer, S. A.; Savory, J.; Brown, R. C.; Römisch, S.; Oates, C. W.; Parker, T. E.; Fortier, T. M. Ludlow, A. D. Towards the optical second: verifying optical clocks at the SI limit Optica, OSA, 2019, 6, 448-454

[6] Nemitz, N.; Ohkubo, T.; Takamoto, M.; Ushijima, I.; Das, M.; Ohmae, N. Katori, H. Frequency ratio of Yb and Sr clocks with 5e-17 uncertainty at 150 seconds averaging time Nature Photonics, Nature Publishing Group, 2016, 10, 258-26

[7] Kim, H.; Heo, M.-S.; Lee, W.-K.; Park, C. Y.; Hong, H.-G.; Hwang, S.-W. Yu, D.-H. Improved absolute frequency measurement of the 171 Yb optical lattice clock at KRISS relative to the SI second Japanese Journal of Applied Physics, 2017, 56, 050302

[8] Gao, Q.; Zhou, M.; Han, C.; Li, S.; Zhang, S.; Yao, Y.; Li, B.; Qiao, H.; Ai, D.; Lou, G.; Zhang, M.; Jiang, Y.; Bi, Z.; Ma, L. Xu, X. Systematic evaluation of a 171Yb optical clock by synchronous comparison between two lattice systems Scientific Reports, 2018, 8, 8022

[9] Kobayashi, T.; Akamatsu, D.; Hosaka, K.; Hisai, Y.; Wada, M.; Inaba, H.; Suzuyama, T.; Hong, F.-L. Yasuda, M. Demonstration of the nearly continuous operation of an 171Yb optical lattice clock for half a year Metrologia, IOP Publishing, 2020, 57, 065021

[10] Riehle, F.; Gill, P.; Arias, F. Robertsson, L. The CIPM list of recommended frequency standard values: guidelines and procedures Metrologia, 2018, 55, 188-200

[11] Godun, R. M.; Nisbet-Jones, P.; Jones, J.; King, S.; Johnson, L.; Margolis, H.; Szymaniec, K.; Lea, S.; Bongs, K. Gill, P.;Frequency Ratio of Two Optical Clock Transitions in $^{171}Yb^+$ and Constraints on the Time Variation of Fundamental Constants;Physical Review Letters, American Physical Society, 2014, 113, 210801

[12] Pizzocaro, M.; Sekido, M.; Takefuji, K.; Ujihara, H.; Hachisu, H.; Nemitz, N.; Tsutsumi, M.; Kondo, T.; Kawai, E.; Ichikawa, R.; Namba, K.; Okamoto, Y.; Takahashi, R.; Komuro, J.; Clivati, C.; Bregolin, F.; Barbieri, P.; Mura, A.; Cantoni, E.; Cerretto, G.; Levi, F.; Maccaferri, G.; Roma, M.; Bortolotti, C.; Negusini, M.; Ricci, R.; Zacchiroli, G.; Roda, J.; Leute, J.; Petit, G.; Perini, F.; Calonico, D. Ido, T. Intercontinental comparison of optical atomic clocks through very long baseline interferometry Nature Physics, 2021, 17, 223-227

[13] Pezzè, L.; Smerzi, A.; Oberthaler, M. K.; Schmied, R. Treutlein, P. Quantum metrology with nonclassical states of atomic ensembles Rev. Mod. Phys., American Physical Society, 2018, 90, 035005

[14] Sanner, C.; Huntemann, N.; Lange, R.; Tamm, C.; Peik, E.; Safronova, M. S. Porsev, S. G. Optical clock comparison for Lorentz symmetry testing Nature, 2019, 567, 204-208

[15] Delva, P.; Lodewyck, J.; Bilicki, S.; Bookjans, E.; Vallet, G.; Le Targat, R.; Pottie, P.-E.; Guerlin, C.; Meynadier, F.; Le Poncin-Lafitte, C.; Lopez, O.; Amy-Klein, A.; Lee, W.-K.; Quintin, N.; Lisdat, C.; Al-Masoudi, A.; Dörscher, S.; Grebing, C.; Grosche, G.; Kuhl, A.; Raupach, S.; Sterr, U.; Hill, I. R.; Hobson, R.; Bowden, W.; Kronjäger, J.; Marra, G.; Rolland, A.; Baynes, F. N.; Margolis, H. S. Gill, P. Test of Special Relativity Using a Fiber Network of Optical Clocks Physical Review Letters, American Physical Society, 2017, 118, 221102

[16] Grotti, J.; Koller, S.; Vogt, S.; Häfner, S.; Sterr, U.; Lisdat, C.; Denker, H.; Voigt, C.; Timmen, L.; Rolland, A.; Baynes, F. N.; Margolis, H. S.; Zampaolo, M.; Thoumany, P.; Pizzocaro, M.; Rauf, B.; Bregolin, F.; Tampellini, A.; Barbieri, P.; Zucco, M.; Costanzo, G. A.; Clivati, C.; Levi, F. Calonico, D. Geodesy and metrology with a transportable optical clock Nature Physics, 2018, 14, 437-441

[17] M.Takamoto et al.; Test of general relativity by a pair of transportable optical lattice clocks; Nature Photonics;

[18] D. B. Sullivan, D. W. Allan, D. A. Howe, and F. L. Walls. NIST Technical Note 1337: Characterization of Clocks and Oscillators. Tech. rep. National Institute of Strandard and Technology, 1990.

[19] A.Ludlow;The Strontium Optical Lattice Clock: Optical Spectroscopy with Sub-Hertz Accuracy;B.S. Physics, Brigham Young University, 2002 PhD thesis;

[20] F. Levi et al., "The cryogenic fountain ITCsF2," 2009 IEEE International Frequency Control Symposium Joint with the 22nd European Frequency and Time forum, Besancon, France, 2009, pp. 769-773, doi: 10.1109/FREQ.2009.5168289.

[21] Absolute frequency measurement of the $^1S_0 - ^3P_0$ transition of ^{171}Yb with a link to International Atomic Time; M.Pizzocaro et al. Metrologia 2019

[22] F.Bregolin; ^{171}Yb optical frequency standards towards the redefinition of the second; PhD thesis; Politecnico di Torino

[23] M.Pizzocaro et al. Absolute frequency measurement of the $^1S_0 - ^3P_0$ transition of ^{171}Yb;Metrologia 54 (2017) 102–112

[24] Advanced in atomic physics, an overview; Claude Cohen-Tannoudji, David Guery-Odelin.

[25] Barber et al. Optical Lattice Induced Light Shifts in an Yb Atomic Clock; 10.1103/PhysRevLett.100.103002

[26] S.B.Koller et al.; Transportable Optical Lattice Clock with 7×1017 Uncertainty;: 10.1103/PhysRevLett.118.073601

[27] G S Belotelov et al; Lattice light shift in strontium optical clock;l 2020 Laser Phys. 30 045501

[28] Towards an optical clock for space: Compact, high-performance optical lattice clock based on bosonic atoms S. Origlia, M. S. Pramod, S. Schiller, Y. Singh, K. Bongs, R. Schwarz, A. Al-Masoudi, S. Dörscher, S. Herbers, S. Häfner, U. Sterr, and Ch. Lisdat Phys. Rev. A 98, 053443 – Published 29 November 2018

[29] D. Voigt, E. Schilder, R. Spreeuw, and H. V. L. Van Den Heuvell, Characterization of a high-power tapered semiconductor amplifier system, Applied Physics B 72, 279 (2001).

[30] V. Bolpasi and W. Von Klitzing, Double-pass tapered amplifier diode laser with an output power of 1 W for an injection power of only 200 µW, Review of Scientific Instruments 81, 113108 (2010).

[31] R. Dumke, M. Volk, T. M¨uther, F. Buchkremer, G. Birkl, and W. Ertmer, Micro-optical realization of arrays of selectively addressable dipole traps: a scalable configuration for quantum computation with atomic qubits, Physical Review Letters 89, 097903 (2002).

[32] T. Bienaim´e, G. Barontini, L. M. de L´epinay, L. Bellando, J. Chab´e, and R. Kaiser, Fast compression of a cold atomic cloud using a blue-detuned crossed dipole trap, Physical Review A 86, 053412 (2012).

[33] Westergaard, P. G.; Lodewyck, J.; Lorini, L.; Lecallier, A.; Burt, E. A.; Zawada, M.; Millo, J. Lemonde, P. Lattice-Induced Frequency Shifts in Sr Optical Lattice Clocks at the 10^{-17} Level Physical Review Letters, American Physical Society, 2011, 106, 210801

[34] NIST Atomic Spectra Database Lines Form

[35] K.Beloy et al. Determination of the $5d6s\ ^3D_1$ state lifetime and blackbody-radiation clock shift in Yb; PHYSICAL REVIEW A 86, 051404(R) (2012)

[36] N.D.Lemke; Optical Lattice Clock with Spin-1/2 Ytterbium Atoms;University of Colorado at Boulder;PhD thesis;

[37] Ushijima, I.; Takamoto, M. Katori, H. Operational Magic Intensity for Sr Optical Lattice Clocks Phys. Rev. Lett., American Physical Society, 2018, 121, 263202

[38] V.A.Dzuba, A.Derevianko; Dynamic polarizabilities and related properties of clock states of the ytterbium atom; 2010 J. Phys. B: At. Mol. Opt. Phys. 43 074011

[39] Brown, R. C.; Phillips, N. B.; Beloy, K.; McGrew, W. F.; Schioppo, M.; Fasano, R. J.; Milani, G.; Zhang, X.; Hinkley, N.; Leopardi, H.; Yoon, T. H.; Nicolodi, D.; Fortier, T. M. Ludlow, A. D. Hyperpolarizability and Operational Magic Wavelength in an Optical Lattice Clock Physical Review Letters, American Physical Society, 2017, 119, 253001

[40] N.Nemitz et al; Modeling light shifts in optical lattice clocks; PHYSICAL REVIEW A 99, 033424 (2019)

[41] H.Katori; Strategies for reducing the light shift in atomic clocks; PHYSICAL REVIEW A 91, 052503 (2015)

[42] Orazio Svelto, Principles of Lasers; 4th edition

[43] O Svelto and S Taccheo and C Svelto;Analysis of amplified spontaneous emission: some corrections to the Linford formula;Optics Communications;1998;

[44] FIBERDOCK. Compact fiber coupler;FiberDock 2V0 Manual: M-011 Version 02; Toptica photonics.

[45] Kogelnik, H. Li, T.;Laser Beams and Resonators; Appl. Opt., OSA, 1966, 5, 1550-1567

[46] Milani et al.; Multiple wavelength stabilization on a single optical cavity using the offset sideband locking technique; Optics Letters 42;2017;

[47] `https://dl.cdn-anritsu.com/en-au/test-measurement/files/Manuals/Operation-Manual/MS9740A/MS9740A_Operation_Manual_E_21_0.pdf`

[48] G. Talli, M.J. Adams; Amplified spontaneous emission in semiconductor optical amplifiers: modelling and experiments/ Optics Communications 218 (2003) 161–166

[49] Slawomir Bilicki. Strontium optical lattice clocks: clock comparisons for timescales and fundamental physics applications. Atomic Physics [physics.atom-ph]. Observatoire de Paris - SYRTE, 2017. English.

[50] DFC-BC DFC-MD Beat detection unit; Manual: M-084 Version 01; Copyright 2019 TOPTICA Photonics AG

[51] R.J. Fasano;Characterization and suppression of background light shifts in an optical lattice clock;rXiv:2103.12052v1 [physics.atom-ph] 22 Mar 2021;

[52] S.C.Barden et al; Tunable gratings: imaging the universe in 3-D with volume-phase holographic gratings;2000ASPC..195..552B;

[53] J.Hellstrom et al.;Finite Beams in Reflective Volume Bragg Gratings:Theory and Experiments; IEEE JOURNAL OF QUANTUM ELECTRONICS, VOL. 44, NO. 1, JANUARY 2008

[54] Ivan Divliansky,Volume Bragg Gratings: Fundamentals and Applications in Laser Beam Combining and Beam Phase Transformations,Holographic Materials and Optical Systems, Edited by Izabela Naydenova.

[55] E.A.Donley,T.P.Heavner, F Levi,M.O.Tataw, and S.R.Jefferts; Double-pass acousto-optic modulator system;Rev. Sci. Instrum. 76, 063112 (2005)

[56] Anthony Siegman, Lasers, ISBN 0-935702-11-5;

[57] Martin Blaha, Ausgeführt am Atominstitut der Technischen Universität Wien, Master Thesis.

[58] N.V.Vitanov; Power broadening revisited: theory and experiment; Optics Communications 199(2001)117-126

[59] P.G.Westergaard, Horloge a reseau optique au Strontium: en quete de la performance ultime; PhD thesis;

[60] Blatt S, Thomsen J W, Campbell G K, Ludlow A D, Swallows M D, Martin M J, Boyd M M and Ye J 2009 Phys. Rev. A 80 052703